COHERENT STRUCTURES IN INCOMPRESSIBLE FLUID FLOWS

A Dissertation
Presented to
The Academic Faculty

By

Kimberly Yovel Short

In Partial Fulfillment
of the Requirements for the Degree
Doctor of Philosophy in the
School of Physics

Georgia Institute of Technology

December 2019

COHERENT STRUCTURES IN INCOMPRESSIBLE FLUID FLOWS

Approved by:

Dr. David Ballantyne, Advisor
School of Physics
Georgia Institute of Technology

Dr. Kurt Wiesenfeld
School of Physics
Georgia Institute of Technology

Dr. Francesco Fedele
School of Civil and Environmental Engineering
Georgia Institute of Technology

Dr. Pablo Laguna
School of Physics
Georgia Institute of Technology

Dr. Michael Schatz
School of Physics
Georgia Institute of Technology

Date Approved: October 25, 2019

La vérité vaut bien qu'on passe quelques années sans la trouver.

Jules Renard

ACKNOWLEDGEMENTS

I would like to acknowledge the generous financial support of the Professor Dr. Martin B. Short Graduate Fellowship for Wives Who Really, Really Wanted to Pursue Physics as a Profession But Had Their Dreams Crushed in the Most Heartbreaking Ways Possible; and the National Science Foundation Graduate Research Fellowship under Grant No. DGE-0707424.

TABLE OF CONTENTS

LIST OF TABLES

LIST OF FIGURES

SUMMARY

The work presented here is broadly related to the transition to turbulence in pipe at intermediate Reynolds numbers.

Chapter 1 includes a background of the problem of turbulence and the Navier-Stokes equations, as well as two classes of structures observed during the transition to turbulence: numerically-extracted solutions of the Navier-Stokes equations (the "exact") and localized/patterned turbulent spots that are not themselves solutions of the Navier-Stokes equation but are nonetheless pervasive during the transition (the "inexact").

Exact solutions of the Navier-Stokes equations include the sole analytically-derived Hagen-Poiseuille parabolic flow profile and an unknown number of computationally-extricated solutions whose form cannot be simply written down.

Approximate solutions to the Navier-Stokes equations can be found by embracing a litany of simpler, related equations and by linearization techniques, which are likewise mentioned in Chapter 1.

High-dimensional descriptions of turbulence is predicted by periodic orbit theory (POT) which expects to describe turbulence exactly, as opposed to approximately. The search for relative periodic orbits and traveling waves in pipe—the constituents solutions to periodic orbit theory—is described pedagogically in Chapter 1 with some technical details detailed in Chapter 2. The successful search for relative periodic orbits at transitional Reynolds numbers gave a catalogue of invariant solutions; many of these solutions were continued in parameter space to find that solutions coexist with the transitional regime (according to POT, this is not a coincidence). The work in study was largely numerical, and technical descriptions of the codes and numerical techniques are given in Chapter 2, publications resulting from work related to appears in Chapters 3 and 4.

In addition to collecting solutions to eventually test periodic orbit theory, an investigation into the Barkley's pipe model—a system that successfully models the transition to

turbulence in pipe—was undertaken. The resultant paper appears as Chapter 5.

CHAPTER 1
INTRODUCTION AND BACKGROUND

Two of the most important substances on Earth, air and water, are both fluids, substances that continually deform, or flow, when a shear force or stress is applied. Water and air of are two of the five classical elements of ancient Greece, and and the ancient peoples of Egypt, Babylonia, Japan, Tibet, and India likewise include water and air in similar lists. Both fluids are crucial to life as we know it, providing plants, animals and other organisms with the substances required to sustain life. Air contains the oxygen for animals to breathe, and the carbon dioxide required by plants to thrive. And, as far as scientists know, all lifeforms require water to live.

The importance of these fluids motivates a complete understanding of their behavior.

Unfortunately, the differential equations that describe the behavior of fluids—the famed Navier-Stokes equations—are nonlinear and exact analytical solutions are hard to come by. Still, empirical studies have found that a single parameter–the Reynolds number Re–can largely determine whether a fluid flow will be smooth and predictable ("laminar") or unpredictable ("turbulent").[1]Specifically, fluids are laminar at small Re and turbulent at large Re. Low Re fluids have a trivial velocity profile—the single analytically-tractable solution of the NSE, the "laminar" solution—and observations of fluids at high Re have yielded significant statistical information of turbulent fluid flows, e.g., Kolmogorov's $-5/3$ power law for the distribution of turbulent energy.

Much is already known about both the low and high Re regimes, but what about the intermediate regime where flows are neither fully laminar nor fully turbulent?

This intermediate Re regime is an area of significant interest to fluid dynamicists for myriad reasons, and is currently an active area of study both computationally and exper-

[1]"Unpredictable" does not necessarily mean chaotic. Stochastic systems are also unpredictable.

imentally. Naturally, scientists are eager to understand how fluids transition from very predictable laminar flow at low Re to fully-developed turbulent flow described statistically at much higher Re. The dynamicists who champion the *periodic orbit theory* (POT) of turbulence expect a weighted average of a large number of computationally-extracted invariant solutions of the NSE to reproduce the statistics obtained from laboratory experiments. The invariant solutions are observed in direct numerical simulations (DNS) of the NSE and describe coherent motions and well-behaved cycles of flows ("exact coherent structures"), including traveling wave solutions (TW), periodic orbits (PO) and relative periodic orbits (RPO), solutions whose analogues in low-dimensional chaotic systems reproduce the statistics of low-dimensional chaos upon application of POT[1]. Further, a PO has been shown to predict about 80 seconds fluid flow in a quasi two-dimensional laboratory experiment[2], a remarkable achievement given the generally unpredictable behavior of turbulent flows. However, at least one study has failed to confirm POT in transitionally-turbulent fluid flows (though this may be due to an inadequate number of required solutions) and evidence of dynamically-relevant paths between solutions ("heteroclinic connections", the other important element of POT) is conspicuously lacking. So while periodic orbits and relative periodic orbits appear to play some role in the transition to turbulence, it is not yet known if POT can reproduce turbulent and near-turbulent statistics of high-dimensional fluid flows as expected.[2] The campaign to find a sufficiently large set of exact solutions and confidently test POT in pipe flow is underway.[3]

The intermediate Re regime is of interest to physicists for an additional reason: many behaviors seen during the transition to turbulence are likewise seen in other nonlinear, pattern-forming systems. Observations of intermediate-Re two-dimensional flows find localized patches of turbulence surrounded by otherwise smooth or laminar flow; for a range of Re, the localized structures grow in number and extent, forming well-defined stripes of

[2]As far as the author know, POT has no competitor, so there is the possibility of creating a competing approach to POT that also relies upon TWs and RPOs.

[3]The author has found several dozen such solutions in pipe.

alternating turbulent and quiescent flow. Thus, a possible connection exists between other systems of nonlinear equations and the Navier-Stokes equation. An understanding of one may elucidate another. For example, homoclinic snaking—a process by which a spanwise-localized solution acquires more and more structure to grow to fill the spatial domain—is observed in the cubic-quintic Swift-Hohenberg equation, as well as in two-dimensional plane Couette flow. As of the time of this writing, no one has succeeded in deriving the Swift-Hohenberg equation from the NSE, but the shared snaking behavior suggests such a link exists.

Finally, most natural systems are nonlinear. The linear systems that do exist in nature are few, or are often the result of physical idealizations or assumptions. Consequently, there is a need to develop and advance more techniques and methods to analyze nonlinear systems in general. The techniques we develop to understand turbulence are not thought experiments without real-world application; they can be carried over to other nonlinear systems.

Given the complexity of solving the incompressible Navier-Stokes equations exactly for high Re in three-dimensional cylindrical geometry, it is unsurprising that simplified models exist to describe large-scale features of transitionally-turbulence flow. In particular, Barkley has introduced a series of models that describe the transition to turbulence remarkably well[3]. A discussion of his model comprises a portion of this dissertation.

1.1 Research Objectives and Scope

Investigations of the subcritical transition to turbulence for incompressible fluid flows are ongoing with most recent focus on the mechanisms driving pattern formation[4] and localization[5] of dissipative coherent structures. Attention is often given to reduced models of specific canonical flows that are more amenable to analysis than the full Navier-Stokes equations (NSE). The models, as well as the NSE, see a series of patterns emerge during the transition. Most recently, much work has been done to understand the localization aspect

of pattern formation, which is being understood through a combination of reduced models, and the linearization of the NSE about particular invariant solutions and their numerical continuation in other domains.

The research program highlighted in this document includes studies of a small number of projects, all of which are related to the coherent structures observed during the transition to turbulence. Projects include finding invariant solutions, continuing the search for relative periodic orbits in pipes to build a sufficiently large collection of solutions to test the predictions of periodic orbit theory, and an investigation of Barkley's successful pipe flow model.

In short, we observe both exact invariant solutions and spatiotemporal intermittency during the transition to turbulence. It begs the question: Is there a relationship between solutions of the Navier-Stokes equations and the coherent structures we see?

1.2 The Navier-Stokes Equations

All fluid flows, including gases like air and liquids like water, are governed by the Navier-Stokes equations (NSE). The dimensionful form of the NSE for incompressible fluid flow are:

$$\frac{\partial \mathbf{V}}{\partial t} + (\mathbf{V} \cdot \nabla)\,\mathbf{V} - \nu \nabla^2 \mathbf{V} = -\frac{1}{\rho}\nabla P + \mathbf{F} \tag{1.1}$$

where

$$\mathbf{V} = (U, V, W)^T \tag{1.2}$$

is the velocity field, and $U(x_1, x_2, x_3; t), V(x_1, x_2, x_3; t), W(x_1, x_2, x_3; t)$ are the components of the velocity field which depend on the spatial coordinates x_1, x_2, x_3 and time t, $P = (P_1, P_2, P_3)$ is the applied pressure, and $\mathbf{F}$ is an external body force that may act on the fluid, e.g. gravity. For the pipe studies undertaken here, one assumes $\mathbf{F} = 0$.

Conservation of mass, coupled with the requirement that the fluid density within a moving volume remains constant, gives us the incompressibility condition. The mathematical statement of incompressibility is:

$$\nabla \cdot \mathbf{V} = 0 \tag{1.3}$$

As water and most other Newtonian liquids are very nearly incompressible this is typically a physically sound assumption to make.

In physics, the set of fundamental units are mass (M), length (L), and time (T), and all other quantities are expressed in terms of these units. For example, the dimensions of velocity V and pressure p can be expressed in terms of these quantities:

$$[V] = \frac{L}{T} \quad , \quad [p] = \frac{M}{LT^2} \tag{1.4}$$

The properties of a viscous incompressible fluid, like those under study here, depend crucially on two important parameters, mass density ρ

$$[\rho] = \frac{M}{L^3} \tag{1.5}$$

and kinematic viscosity ν (momentum diffusivity)

$$[\nu] = \frac{L^2}{T} \tag{1.6}$$

A convenient dimensionless parameter is the Reynolds number Re, which is defined in terms of a characteristic velocity V_o and characteristic lengthscale L_o,

$$Re = \frac{V_o L_o}{\nu} \tag{1.7}$$

which facilitates rewriting Eq. 1.1 in a dimensionless form,

$$\frac{\partial \mathbf{V}}{\partial t} + (\mathbf{V} \cdot \nabla)\,\mathbf{V} - \frac{1}{Re}\nabla^2 \mathbf{V} = -\nabla P \tag{1.8}$$

Re is the important parameter that describes the character of observed flows.

The Navier-Stokes equations are expressions of momentum and volume conservation. In terms of the advective derivative (material derivative),

$$\frac{D}{Dt} \equiv \frac{\partial}{\partial t} + \mathbf{V} \cdot \nabla \tag{1.9}$$

Eq. 1.1 is

$$\underbrace{\rho\left(\frac{D\mathbf{V}}{Dt}\right)}_{\text{time rate of change of momentum}} = \underbrace{-\nabla P + \frac{1}{Re}\nabla^2 \mathbf{V}}_{\text{net force}} \tag{1.10}$$

where we can think of the left-hand side as the time rate of change of momentum (mass

times acceleration) equal to the resultant of the pressure and diffusive forces acting on the fluid. That is to say, this is Newton's second law for incompressible fluids. We note that the pressure term acts as a source term in the momentum equation; there is not an evolution equation for the pressure.

1.3 The Importance of Reynolds Number

For many of the fluid flows being discussed in this document, the dimensionless quantity is the Reynolds number Re, which can be thought of as the ratio of inertial forces to viscous forces,

$$Re = \frac{\text{inertial}}{\text{viscous}} \tag{1.11}$$

or if the reader prefers, the ratio of inertial to viscous timescales:

$$\frac{(\mathbf{V}\cdot\nabla)\,\mathbf{V}}{\nu\nabla^2\mathbf{V}} \sim \frac{V_o^2/L_o}{\nu V_o/L_o^2} = \frac{V_o L_o}{\nu} \equiv Re \tag{1.12}$$

where the inertial forces are related to the quantities that drive the flow and the viscous to the forces that dissipate energy. As a general rule, when the relevant inertial force far exceeds the viscous, turbulence erupts.

In pipe with a fixed circular cross section, the inertial forces are related to the momentum flux induced by a pressure or mass gradient. That is,

$$Re = \frac{\text{momentum flux}}{\text{viscosity}} = \frac{\rho\,\Delta V\,\Delta x}{\mu}$$

Here, ρ is the density of the fluid, ΔV is a characteristic difference in velocity between two parcels of fluid separated by a characteristic length Δx, and μ is the dynamic viscosity. The larger the difference in momentum flux between two regions of the fluid, the larger viscosity must be to even out momentum variations and keep the fluid moving smoothly

(*laminar flow*). When Re is small ($Re \ll 1$), flow will be smooth (laminar). Conversely, when Re is large ($Re \gg 1$), neighboring particles of fluid may move at very different velocities—that is, fluid parcels may exhibit large variations in momentum—giving rise to complex *turbulent* flow.

By convention, the characteristic distance Δx described above is taken to be the diameter D of the pipe. Thus, Reynolds number for pipe is

$$Re_{pipe} = \frac{\overline{U}D}{\nu} \quad \text{(pipe)} \tag{1.13}$$

where $\overline{U}$ is the mean speed of the fluid through the pipe and and $\nu \equiv \mu/\rho$ is the kinematic viscosity. In the absence of a gradient to drive the flow, the viscous forces would restore equilibrium by bringing all fluid to dynamic equilibrium. Because of the no-slip boundary condition at the walls,

$$\mathbf{V} \times \hat{r}\Big|_{\partial\Omega} = 0 \quad \text{where} \quad \partial\Omega \equiv r = \frac{D}{2} \tag{1.14}$$

$V \to 0$ for all the fluid in the pipe in the absence of an external driving mechanism. Thus, the only equilibrium fluid state is that corresponding to no flow at all. It follows then that all sustained flows are nonequilibrium states.

1.4 What makes solving the NSE so difficult?

1.4.1 The non-linear inertial term

The non-linear inertial term

$$(\mathbf{V} \cdot \nabla)\mathbf{V} \tag{1.15}$$

is the term that hinders complete understanding of the NSE, e.g., by severely constraining use of perturbative methods embraced in other areas of mathematical physics[6].

1.4.2 The Closure Problem

The velocity and pressure fields—$\mathbf{V}$ and $\mathbf{P}$, respectively—may also be decomposed into a time-averaged (and thus, time-independent) mean component $\overline{\mathbf{U}}$ and $\overline{p}$, and a time-dependent fluctuating part $\mathbf{u}$ through a process called *Reynolds decomposition* such that

$$V_i(x, y, z, t) = \overline{U}_i(x, y, z) + u_i(x, y, z, t) \tag{1.16}$$

$$P_i(x, y, z, t) = \overline{p}_i(x, y, z) + p_i(x, y, z, t) \tag{1.17}$$

where the time-averaged mean speed is found by calculating

$$\overline{U}_i(x, y, z) = \lim_{T\to\infty} \left(\frac{1}{T} \int_0^T u(x(t), y(t), z(t))\, dt \right) \tag{1.18}$$

Substituting into Eq. 1.1 and taking averages over the quantities,

$$\frac{\partial U}{\partial t} + U_j \frac{\partial U_i}{\partial x_j} = -\frac{1}{\rho}\frac{\partial P}{\partial x_i} + \frac{\partial}{\partial x_j}\left(\frac{\mu}{\rho}\frac{\partial U_i}{\partial x_j} \right) + \frac{\partial(-\overline{u_i u_j})}{\partial x_j} \tag{1.19}$$

It is the $\partial(-\overline{u_i u_j})/\partial x_j$ term, known as the Reynolds stress, term that invites the closure problem. We see that velocity fluctuations still appear. In order to obtain equations with only a mean velocity and pressure, we need to forcibly close the equations, e.g. by modeling the Reynolds stress as a function of the mean flow. Introducing an equation for the Reynolds stress necessarily involves the addition of equations involving higher-order correlations between the fluctuating velocity components. This is the closure problem.

The NSE are four equations (one dynamical equation for each of component of the velocity, and the continuity equation which enforces incompressibility) and five unknowns (the three velocity components, the pressure, and the density) which leads to the notorious closure problem. To solve the system, the values of the component velocities, as well as the pressure gradient ∇P, must be specified at the boundaries. Among the techniques available

for tackling this issue is the Pressure-Poisson equation. See Section 2.3.

1.4.3 Nonlocality of the Navier-Stokes Equations

The incompressible NSE are nonlocal, a consequence of the pressure term. In general, partial differential equations relate the value of an unknown function to its derivatives of various orders. In order for a PDE to hold at a particular point x, one needs to know the values of the function in an arbitrarily small neighborhood $x + y$ so that the relevant derivatives can be computed. When this calculation can be done, the PDE is local.

However, for some PDEs (including the NSE), values of the function far from the point x are needed, typically due to integral operators, e.g.

$$\frac{\partial V}{\partial t} = \int_{R^d} \left(V(x+y,t) - V(x,t)K(y)\right) dy \tag{1.20}$$

for some kernel K. To see this in the NSE, taking the divergence of Eq. 1.1 yields a term

$$\underbrace{-\nabla^2 p}_{\text{requires information at boundary } \Omega} = \nabla \cdot (\nabla p) = \nabla \cdot (\mathbf{V} \cdot \nabla \mathbf{V}) = \underbrace{\partial_i \partial_j \left(V_i V_j\right)}_{\text{local}} \tag{1.21}$$

which requires knowledge of the pressure of the boundary Ω. The Laplacian $\nabla^2 p$ is determined by local information about V, but ∇p is not.

1.4.4 Spreading turbulence

For transitional Reynolds numbers, flow is spatiotemporally intermittent, with localized turbulent patches surrounded by quiescent laminar flow. In the range $2000 \leq Re \leq 3000$, steady puffs of constant length (about $20 - 25D$ in length) are observed with the upstream and downstream fronts of the puff moving at the same speed, about $0.9 - 0.95\ \overline{U}$, where $\overline{U}$ is the mean speed of the flow[7]. Above $Re \approx 3000$, the upstream and downstream fronts move apart, with the head of the puff traveling about 30% faster than $\overline{U}$ and the tail

(a)

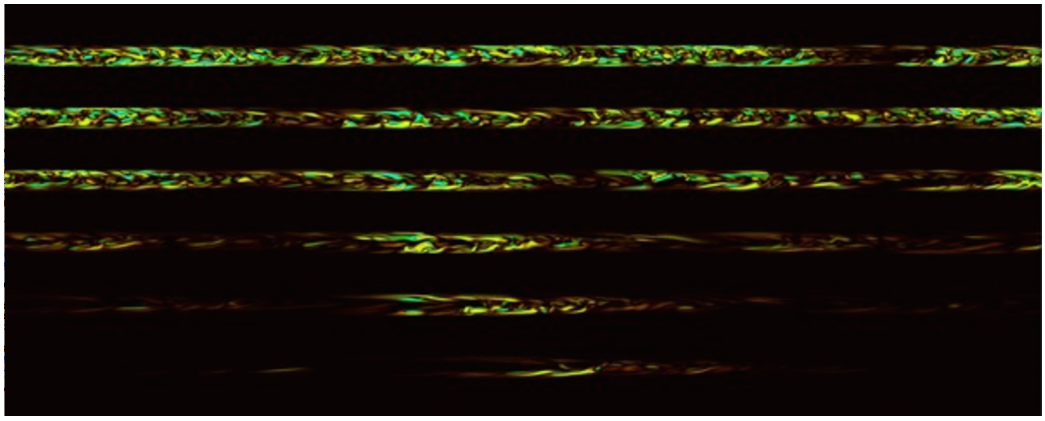

(b)

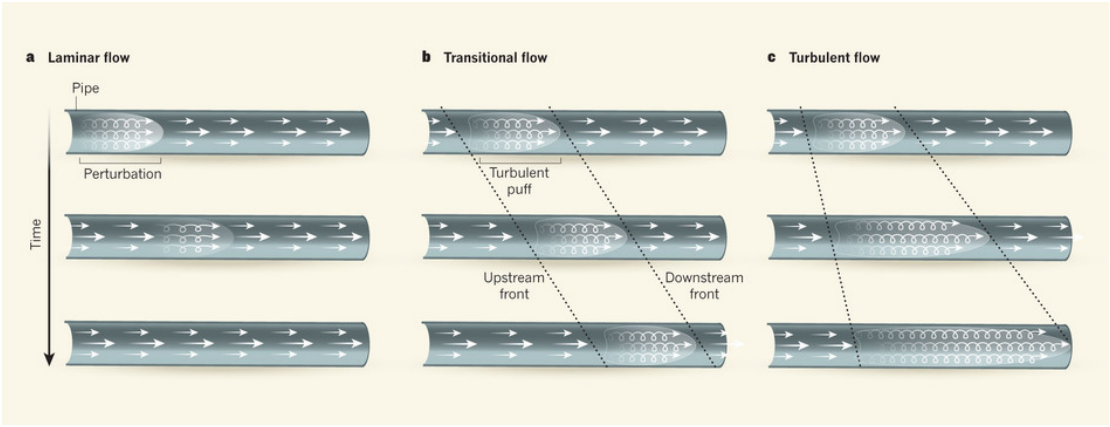

Figure 1.1: (a) The spreading of localized turbulent puffs in a pipe, with time increasing from bottom to top. (b) The transition to turbulence for pipe, with Reynolds number Re increasing from left to right. At the beginning of the transition, unstable localized patches of turbulence are seen that eventually decay, after which the laminar state is recovered. As Re increases, the localized structures give way to long-lived metastable puffs (analogous to stripes and bands seen in several $2D$ flows) that advect through the pipe. As Re is increased yet further, the puffs split and spread, filling the whole pipe with turbulent flow.

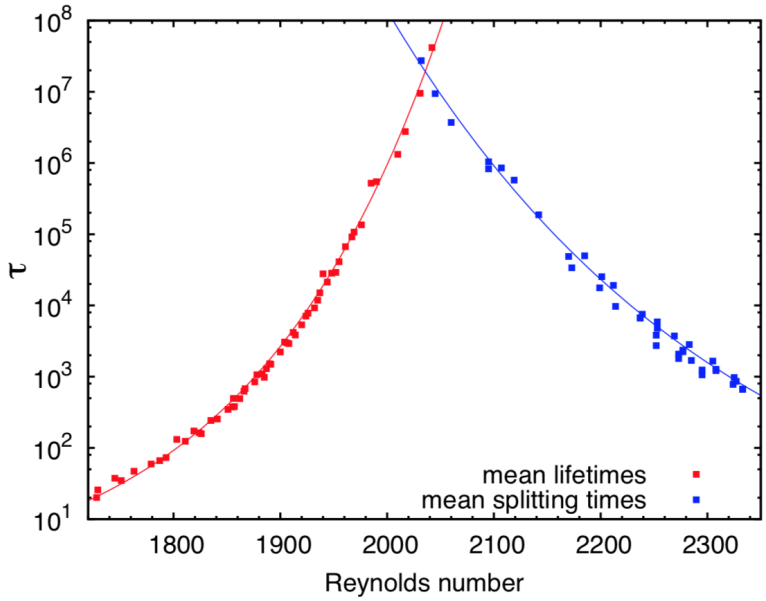

Figure 1.2: The transition to sustained turbulence in pipe occurs when puff splitting exceeds puff decay. The crossover occurs at $Re = 2040$. To the right of this value, puff splitting occurs on a faster time scale τ than does decay, sustaining turbulence via spatio-temporal intermittency.

traveling about 30% slower than $\overline{U}$ so that the turbulent puff expands to fill the whole pipe (see Fig.1.1).

Recent experiment results suggest that the transition to sustained turbulence in pipe occurs when the rate at which puffs split exceeds the rate at which puffs relaminarize. The point at which the rates are equal defines a transition point. This critical point was experimentally determined to be $Re = 2040$ for pipe[8]. See Fig.1.2

1.4.5 The Role of Boundary Conditions

The canonical fluid flows under discussion in this dissertation are either closed or open fluid systems. Closed systems retain all the fluid and recirculate it, e.g. by shearing action of walls; no fluid leaves or enters the system. Open systems, by contrast, have fluid that leaves at a boundary with a matching amount reintroduced at another boundary to keep the total amount of fluid constant. Notably, pipe flow and channel flows are open systems: fluid enters the pipe or channel at an inlet and leaves the system at an exit downstream.

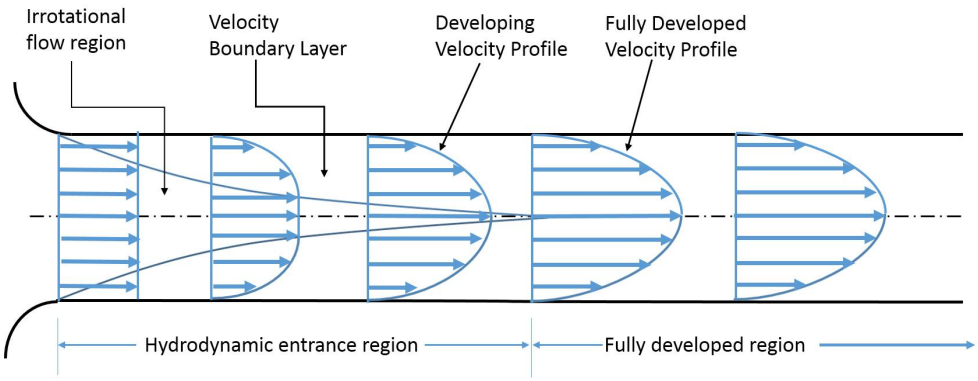

Figure 1.3: Development of the full flow in pipe.

The open nature of pipe flow leads to additional concerns. On the experimental side, care must be taken to maintain the Reynolds number of the fluid under study, whether by enforcing constant mass flux or a constant pressure gradient. The introduction and control of perturbative jets of fluid into the pipe must be carefully considered.

On the theoretical side, open systems can be convectively unstable, leading to convective chaos and noise-sustained structures that advect down the axis of the pipe. Interestingly, noise-sustained structures in other convectively unstable systems have behavior that qualitatively resembles that of puff and slugs in pipe, prompting the question of whether or not the inlet perturbations can trigger convectively chaotic slugs. Though most recent data suggest that instabilities in the entrance flow do not trigger the transition to turbulence further downstream, transient growth in the inlet may contribute.

1.4.6 Inlet behavior

The linearly stable parabolic profile—the Hagen-Poiseuille profile—is not realized throughout the whole of the pipe (Fig. 1.3). The pipe can be separated into two regions: the hydrodynamic entrance region and the fully developed region. The hydrodynamic entrance length L_h can be approximated for laminar flow as [9],

$$L_h \approx 0.05 Re\ D \tag{1.22}$$

Thus, at $Re = 2000$, $L_h \approx 100D$.

The dynamics at the entrance of the pipe can play a crucial role in the dynamics of the fluid far downstream. Quoting Mukund and Hof[10],

> *even in pipes several thousand diameters long, the spatio-temporal intermittent flow patterns observed at the end of the pipe strongly depend on the initial conditions...*

1.5 Outsmarting the NSE

1.5.1 Scalar potential functions and the NSE

A stream function formulation of the incompressible Navier-Stokes equations allows the system of four coupled equations—three velocity components and the attendant pressure—to be written in terms of two stream functions. The pressure terms are eliminated, greatly simplifying the system, and the continuity equation is automatically satisfied.

Two approaches are available to us. The first defines the velocity field $\mathbf{V}$ in terms of two scalar stream surfaces ψ and ϕ:

$$\mathbf{V} = \nabla\psi \times \nabla\phi \tag{1.23}$$

Here, the velocity is orthogonal to both gradients, i.e., $\mathbf{V}$ is tangent to $\psi = constant$ and $\phi = constant$. Consequently, the intersections of ψ with ϕ gives the streamlines, the trajectories along which the flow is constant. This formulation requires the two scalar functions to be defined on the boundaries.

The second approach exploits the incompressibility of $\mathbf{V}$. The vector identity

$$\nabla \cdot (\nabla \times \mathbf{A}) = 0 \tag{1.24}$$

ensures that the incompressibility condition $\nabla \cdot \mathbf{V} = 0$ is automatically satisfied when we

define a vector potential $\mathbf{A}$ such that

$$\mathbf{V} = \nabla \times \mathbf{A} \tag{1.25}$$

One possible form of $\mathbf{A}$ is

$$\mathbf{A} \equiv \psi \, \nabla\phi \tag{1.26}$$

where ψ and ϕ are again scalar. Plugging in this expression,

$$\begin{aligned} \mathbf{V} &= \nabla \times \mathbf{A} \\ &= \nabla \times (\psi \nabla\phi) \\ &= \psi\nabla \times (\nabla\phi) + (\nabla\psi \times \nabla\phi) \\ &= \nabla\psi \times \nabla\phi \end{aligned} \tag{1.27}$$

as the curl of a gradient is zero (identically). We note that this form of $\mathbf{A}$ yields the first formulation described in Eq. 1.23.

Stream functions most often arise in the study of two-dimensional flows, where only one such function is required to describe the flow. The following forms for $2D$ flows are frequently encountered:

$$i) \quad u = \frac{\partial\psi}{\partial y}, \quad v = -\frac{\partial\psi}{\partial x} \quad (2D \text{ cartesian}) \tag{1.28}$$

$$ii) \quad u = -\frac{1}{r}\frac{\partial\psi}{\partial z}, \quad v = \frac{1}{r}\frac{\partial\psi}{\partial r} \quad (2D \text{ polar}) \tag{1.29}$$

$$iii) \quad u = \frac{1}{r}\frac{\partial\psi}{\partial\theta}, \quad v = -\frac{\partial\psi}{\partial r} \quad (\text{spherical with azimuthal symmetry}) \tag{1.30}$$

For example, Barnett *et al*. [11] used a single streamfunction ψ in their stuff of 2D plane

Poiseuille flow:

$$u = \overline{U} + \partial_y \psi, \quad v = -\partial_x \psi \tag{1.31}$$

where $\overline{U} = 1 - y^2$ is the laminar parabolic profile.

Stream function formulations are more challenging in three dimensions where two, rather than one, stream functions are required to describe the velocity field. In general, there is no general approach to determining stream functions for 3D flows. An example of two stream functions for a $3D$ rectilinear flow is the ansatz,

$$u = \left(\frac{\partial \psi}{\partial y} - \frac{\partial \phi}{\partial z} \right), \quad v = -\frac{\partial \psi}{\partial x}, \quad w = \frac{\partial \phi}{\partial x} \quad (3D \text{ cartesian}) \tag{1.32}$$

A variation of the two stream function approach to describing $3D$ flows is the poloidal-toroidal decomposition:

$$\mathbf{V} = (\hat{z} \times \nabla \mathcal{T}) + \nabla \times (\hat{z} \times \nabla \mathcal{P}) \tag{1.33}$$

where $\mathcal{P}$ and $\mathcal{T}$ are the poloidal and toroidal [scalar] potentials, respectively, and $\hat{z}$ is the streamwise direction of flow. For example, In terms of three Cartesian components, the decomposition is

$$\mathbf{V} = \left(-\mathcal{P}_{xz} - \mathcal{T}_y\right) \hat{x} + \left(-\mathcal{P}_{yz} + \mathcal{T}_x\right) \hat{y} + \left(\mathcal{P}_{xx} + \mathcal{P}_{yy}\right) \hat{z} \tag{1.34}$$

where the subscripts denote differentiation. A related, hybrid approach to modeling $3D$ fluids combines a single scalar stream function ψ with a vorticity $\omega \equiv \nabla \times \mathbf{V}$[12] to write the $3D$ NSE. The vorticity form of the NSE is

$$\begin{aligned} \frac{\partial \omega}{\partial t} + \nabla \times (\omega \times (\nabla \times \psi)) &= \nu \nabla^2 \omega \\ \omega &\equiv -\nabla^2 \psi \end{aligned} \tag{1.35}$$

The vorticity ω may also be written in terms of the poloidal and toroidal scalar potentials; for example, in $3D$ Cartesian coordinates:

$$\omega = \left(\nabla^2 \mathcal{P}_y - \mathcal{T}_{xz}\right) \hat{x} + \left(-\nabla^2 \mathcal{P}_x - \mathcal{T}_{yz}\right) \hat{y} + \left(\mathcal{T}_{xx} + \mathcal{T}_{yy}\right) \hat{z} \tag{1.36}$$

If $\hat{x}$ is taken to be the streamwise direction, then the poloidal field $\mathcal{P}$ has no streamwise vorticity, and $\mathcal{T}$ no streamwise velocity.

1.5.2 Symmetries

The NSE possess some important symmetries[4]. Mathematically, a group G of transformations of the solution $\mathbf{v}(\mathbf{r}, t)$ is a symmetry group of the NSE if and only if $\forall g \in G$, $\mathbf{v}$ is a solution to the NSE $\Rightarrow g\mathbf{v}$ is also a solution.

Notable symmetries include:

- Translationally invariance in space:

$$g_s \mathbf{V}(\mathbf{x}, t) = \mathbf{V}(\mathbf{x} - \xi, t) \tag{1.37}$$

- Translationally invariance in time for an arbitrary shift τ:

$$g_t \mathbf{V}(\mathbf{x}, t) = \mathbf{V}(\mathbf{x}, t - \tau) \tag{1.38}$$

[4]Whether the solutions to the NSE possess the same symmetries depends on the geometry of the domain under study, boundary conditions, and Re. In general, solutions do not possess all of the symmetries of the NSE equations, though some many possess some. This fact is exploited during our search for relative periodic orbits in pipe where the translational flow along the pipe axis is "reduced".

such that

$$x^* = x \tag{1.39}$$

$$t^* = t - \tau \tag{1.40}$$

$$\mathbf{V}^* = \mathbf{V} \tag{1.41}$$

$$p^* = p \tag{1.42}$$

- The Navier-Stokes equations are invariant with respect to a uniform translation in space in the frame of reference (a Galilean transformation):

$$g\mathbf{V}(\mathbf{x}, t) = \mathbf{U} + \mathbf{V}(\mathbf{x} - \mathbf{U}t, t) \tag{1.43}$$

The one-dimensional subgroup obeying space-time translations of the form

$$V(x, t) = f(x - ct) \tag{1.44}$$

are traveling wave (TW) solutions.

Note: The imposed pressure gradient in pipe flow causes the fluid to move down the axis of the pipe with some speed $c(z, t)$. In a frame of reference co-moving with the mean bulk velocity $\overline{c}$, a traveling wave (TW) will appear as an equilibrium solution (also called a *relative equilibrium*).

- Reflection Invariant (parity):

$$g_P\mathbf{V}(\mathbf{x}, t) = -\mathbf{V}(-\mathbf{x}, t) \tag{1.45}$$

- The incompressible Navier-Stokes equations are scale invariant:

$$g_{scale}\mathbf{V}(\mathbf{x},\mathbf{t}) = \mathbf{V}^{(\lambda)}(\mathbf{x},t) = \frac{1}{\lambda}\,\mathbf{V}\left(\frac{\mathbf{x}}{\lambda},\frac{t}{\lambda^2}\right) \tag{1.46}$$

for a fixed value of viscosity ν. The pressure is similarly rescaled:

$$g_{scale}\;p(\mathbf{x},t) = \frac{1}{\lambda^2}\,p\left(\frac{\mathbf{x}}{\lambda},\frac{t}{\lambda^2}\right) \tag{1.47}$$

Rescaling invariance leads to the Principle of Hydrodynamic Similarity.

$$Re^{(\lambda)} = \frac{U^{(\lambda)}L^{(\lambda)}}{\nu^{(\lambda)}} = Re \tag{1.48}$$

Similarly, the ratio of pressure forces to inertial forces yields the Euler number Eu:

$$\frac{\text{pressure forces}}{\text{inertial forces}} \sim \frac{\Delta p\;L_o^2}{(\rho L_o^3)(V_o^2/L_o)} = \frac{\Delta p}{\rho V_o^2} \equiv Eu \tag{1.49}$$

The Euler number Eu characterize energy losses in the flow where a perfectly frictionless flow corresponds to an Euler number of 0. Hydrodynamic similarity also requires $Eu^{(\lambda)} = Eu$.

- The Navier-Stokes equations are invariant with respect to a uniform rotation of the frame of reference:

$$g_{rot}\mathbf{V}(\mathbf{x},t) = \mathbf{R}\mathbf{V}(\mathbf{R}^{-1}\mathbf{x},t), \quad \mathbf{R}\in SO(d) \tag{1.50}$$

where $\mathbf{R}$ is the rotation matrix obeying $\mathbf{R}\mathbf{R}^T = \mathbf{R}^T\mathbf{R} = I$ and $|\mathbf{R}| = 1$, such that

$$t^* = t \tag{1.51}$$

$$x_i^* = R_{ij}x_j \tag{1.52}$$

$$V_i^* = R_{ij}V_j \tag{1.53}$$

$$p^* = p \tag{1.54}$$

$$\nu^* = \nu \tag{1.55}$$

Particular systems can admit specific forms of the aforementioned symmetries due to geometries inherent in the systems. For example, steady flow through a rectangular channel called plane Poiseuille flow (also called 2D channel flow) is invariant under translations along its streamwise direction z, and reflection symmetric in y:

$$f(y, z) = f(-y, z) \tag{1.56}$$

Flow through a pipe with circular cross section may possess a discrete rotational symmetry. For the state $\mathbf{V} = (u, v, w, p)^T$, the action $\mathbf{g}_{rot}$ maps the solution $\mathbf{V}$ to a physically-equivalent solution $\mathbf{V}'$:

$$(u, v, w, p)(r, \theta, z) \to (u, v, w, p)\left(r, \theta + \frac{2\pi}{m}, z\right), \quad m = 1, 2, 3, ... \tag{1.57}$$

Similarly for shift-and-reflect symmetry σ where $\mathbf{g}_\sigma\mathbf{V} \to \mathbf{V}'$:

$$(u, v, w, p)(r, \theta, z) \to (u, -v, w, p)\left(r, -\theta, z + \frac{\pi}{\alpha}\right), \quad \text{where } \alpha = \frac{2\pi}{\lambda} \tag{1.58}$$

as well as axial translation symmetry akin to that seen in 2D channel flow.

Periodic Orbit Theory, discussed in [13] and which provided the impetus for the work

done in Sections 3 and 4, predicts that relative periodic orbits form the "backbone" for turbulence. Symmetry reduction offers several computational benefits. For example, transforming to a frame of reference that allows for a symmetry reduction makes finding relative periodic orbits much easier. In addition, the uninteresting dynamics are quotiented out, leaving behind the more complicated symmetryless dynamics for further study.

1.6 Symmetries and Pattern Formation

In 2D space, a spatial translation of (x, y) by (α, β) results in a shifted pattern

$$f(x-\alpha, y-\beta) = F(k,l)e^{-i(\alpha k+\beta l)} \tag{1.59}$$

where k and l are the wavenumbers in the x and y directions, respectively. The Fourier representation of this Galilean invariance in $\hat{x}$ and $\hat{y}$ is:

$$\mathbf{k}' = \mathbf{k} \tag{1.60}$$

$$\omega' = \omega - \mathbf{c}\cdot\mathbf{k} \tag{1.61}$$

$$\mathbf{V}(\mathbf{k},\omega) = \mathbf{V}'(\mathbf{k},\omega-\mathbf{c}\cdot\mathbf{k}) + \mathbf{c}\delta^3(\mathbf{k})\delta(\omega) \tag{1.62}$$

$$\sigma(\mathbf{k},\omega) = \sigma'(\mathbf{k},\omega-\mathbf{c}\cdot\mathbf{k}) \tag{1.63}$$

1.7 Related Equations

There are several partial differential equations with close relationships with that incompressible Navier-Stokes equations, the study of which elucidates our understanding of the NSE as well. In general, these equations have fewer complicating terms and have more tractable solutions.

1.7.1 The Euler Fluid Equations

In the limit of $Re \to \infty$ ($\nu \to 0$) the incompressible Navier-Stokes equation becomes the incompressible Euler fluid equation:

$$\frac{\partial \mathbf{V}}{\partial t} + (\mathbf{V} \cdot \nabla)\, \mathbf{V} + \nabla P = 0 \tag{1.64}$$

Because there is no friction, i.e. $\nu \to 0$, the Euler equations are time reversal invariant and conserves energy.

$$\frac{\partial}{\partial t}\left(\frac{1}{2}|\mathbf{V}|^2\right) + \nabla \cdot \left(\frac{1}{2}|\mathbf{V}|^2\mathbf{V} + p\mathbf{V}\right) = 0 \tag{1.65}$$

The Euler equation is nonlinear with the same quadratic nonlinearity in $\mathbf{V}$ seen in the NSE. It is also symmetric under time reversal:

$$t \to -t \quad ; \quad V \to -V \tag{1.66}$$

and conserves energy, a consequence of vanishing viscosity.

Like the NSE, the Euler equation is scale invariant:

$$\mathbf{x} \to \lambda \mathbf{x} \quad ; \quad t \to \lambda t \tag{1.67}$$

where $\lambda > 0$ is a scalar, implying that it has the same behavior at all lengthscales, large and small.

Like the NSE, the retained pressure term renders the Euler equations nonlocal: One cannot compute the time derivative of the velocity field $\mathbf{V}(\mathbf{x}, \mathbf{t})$ only from the knowledge of the function $\mathbf{V}$ in the neighborhood of x at time t.

The Navier-Stokes equations are a singular perturbation of the Euler equations.

1.7.2 Burgers Equation

An equation related to the NSE is Burgers equation:

$$\frac{\partial \mathbf{V}}{\partial t} + (\mathbf{V} \cdot \nabla)\,\mathbf{V} = \nu \nabla^2 \mathbf{V} \tag{1.68}$$

which lacks the pressure term of the NSE. When viscosity ν is small, most of the dissipation happens in shocks, i.e. small spatial regions with large gradients in the velocity field. The field may be elsewhere smooth but otherwise discontinuous at the location of a shock. In the limit of $\nu \to 0$, the resulting shocks are singularities; there is no viscosity to smooth them out.

As there is non-zero dissipation in Burgers equation, it is not symmetric under time reversal.

The Burger's equation is Galilean invariant:

$$\mathbf{V}(x,t) = \mathbf{U} + \tilde{u}(x - \mathbf{U}t, t) \tag{1.69}$$

where $\mathbf{V}(x,t)$ is the velocity field of the flow and $\tilde{u}(x - \mathbf{U}t, t)$ is the velocity field of the flow in the frame of reference x' moving at velocity $\mathbf{U}$; this field is stationary in coordinate system x such that $x' = x - \mathbf{U}t$.

It admits the following equivalence:

$$\mathbf{v}(x,t) \Leftrightarrow \mathbf{U} + \mathbf{v}(x - \mathbf{U}t) \tag{1.70}$$

Burger's equation has odd reflection symmetry such that

$$V(x,t) \Leftrightarrow -V(-x,t) \tag{1.71}$$

as well as Galilean invariance:

$$V(x,t) = c + \tilde{V}(x - ct, t) \tag{1.72}$$

where V is the velocity field and $\tilde{V}$ is the field in the coordinate system x' moving at speed c.

Burger's equation also displays scale invariance in the limit of small, but non-vanishing viscosity[14].

The Burger's equation has the same quadratic nonlinearity as the Navier-Stokes equation, balanced by a diffusive term, as well as the same spatial and temporal invariances and parity invariances. According to Bec & Khanin[15], Burger had hoped the equation would contribute to the understanding of fluid turbulence. However, "such hopes appeared to be shattered when in the fifties, Hopf and Cole showed that the Burgers equation can be integrated explicitly. This model thus lacks one of the essential properties of Navier-Stokes turbulence: sensitivity to small perturbations in the initial data and thus the spontaneous arise of randomness by chaotic dynamics. Unable to cope with such a fundamental aspect, the Burgers equation then lost its interest in 'explaining' fluid turbulence."

However, the Burger's equation with random forcing found import in cosmology where, in the limit of vanishing viscosity $\nu \to 0$, it is known as the Adhesion Model to model matter distributions in the early universe given matter fluctuations[15].

1.7.3 Linear Stability Analysis

(Author's Note: A more thorough explanation of linear stability analysis can be found in [16])

Solutions to the NSE are regarded as fixed points in state space. Their existence alone is insufficient to understand the time evolution—qualitative or quantitative—of the system as it approaches a fixed point solution. Additional information may be acquired by linearizing

in the neighborhood of the fixed point via Taylor's theorem.

To begin, let us consider the linear stability of a one-dimensional system. Let x^o be an exact solution of the system under study, and $\epsilon(t) = x(t) - x^o$ be a small perturbation of x^o. To determine whether a perturbation grows or decays in time, we take the time derivative

$$\frac{d}{dt}\epsilon(t) = \frac{d}{dt}\left(x(t) - x^o\right) = \dot{x} - 0 = \dot{x} \tag{1.73}$$

since x^o is a fixed point of the system and therefore doesn't change in time. Taylor expanding,

$$f(x^o + \epsilon) = f(x^o) + \epsilon\ f'(x^o) + \mathcal{O}(\epsilon^2) \tag{1.74}$$

where $\mathcal{O}(\epsilon^2)$ are the quadratic and higher-order terns in ϵ. As $f(x^o) = 0$,

$$\dot{\epsilon} = \epsilon\ f'(x^o) + \mathcal{O}(\epsilon^2) \tag{1.75}$$

If the $\mathcal{O}(\epsilon^2)$ terms are negligibly small, then we arrive at a linear equation in ϵ:

$$\dot{\epsilon} \approx \epsilon\ f'(x^o) \tag{1.76}$$

From this, we see that a perturbation $\epsilon(t)$ will grow exponentially in time if $f'(x^o) > 0$ and will decay exponentially towards the fixed point solution if $f'(x^o) < 0$.

Note: If $f'(x^o) = 0$, then the $\mathcal{O}$ terms are not negligible and a nonlinear analysis is required to determine the stability about x^o.

A similar approach is taken for higher-dimensional systems. Consider here a $2D$ system

of coordinates x and y:

$$\dot{x} = f(x, y) \tag{1.77}$$

$$\dot{y} = g(x, y) \tag{1.78}$$

where (x^o, y^o) is a fixed point ("solution") of the system such that $f(x^o, y^o) = 0$ and $f(x^o, y^o) = 0$. Consider a small perturbation about this fixed point,

$$u = x - x^o, \quad v = y - y^o \tag{1.79}$$

Following the $1D$ example above, we find

$$\dot{u} = u\frac{\partial f}{\partial x} + v\frac{\partial f}{\partial y} + \mathcal{O}(u^2, v^2, uv) \tag{1.80}$$

$$\dot{v} = u\frac{\partial g}{\partial x} + v\frac{\partial g}{\partial y} + \mathcal{O}(u^2, v^2, uv) \tag{1.81}$$

To first order, this can be expressed in matrix form as

$$\begin{pmatrix} \dot{u} \\ \dot{v} \end{pmatrix} = \begin{pmatrix} \frac{\partial f}{\partial x} & \frac{\partial f}{\partial y} \\ \frac{\partial g}{\partial x} & \frac{\partial g}{\partial y} \end{pmatrix} \begin{pmatrix} u \\ v \end{pmatrix} + \text{higher order terms} \tag{1.82}$$

The matrix

$$\mathbf{J} \equiv \begin{pmatrix} \frac{\partial f}{\partial x} & \frac{\partial f}{\partial y} \\ \frac{\partial g}{\partial x} & \frac{\partial g}{\partial y} \end{pmatrix} \tag{1.83}$$

is called the Jacobian matrix evaluated at the fixed point (x^o, y^o). When the higher order terms are negligible, we have a linearized system of equations. The stability of the solution is determined by the eigenvalues of $\mathbf{J}$. Positive eigenvalues indicate a repulsion along the corresponding eigenvector; negative eigenvalues indicate an attraction towards the solution.

A solution whose eigenvalues have a non-positive real part is said to be [absolutely] linearly stable.

1.7.4 Linearized *à la* Meseguer & Trefethen

As in the previous section, the incompressible Navier-Stokes equations can be linearized around their solutions, including the laminar solution corresponding to the Hagen-Poiseuille parabolic profile $\overline{w} = 1 - r^2$ as well as invariant numerical solutions, e.g. traveling wave (TW) and relative periodic orbits (RPO) solutions.

To ascertain the linear stability of the laminar parabolic solution in infinitely-long cylindrical pipe, Meseguer & Trefethen[17] considered the *linearized* form of the NSE. In cylindrical coordinates (r, θ, z), the NSE, linearized about the $\overline{w}$, are

$$u_t + \overline{w}u_z = -p_r + \frac{1}{Re}\left(u_{rr} + \frac{u_r}{r} + \frac{u_{\theta\theta}}{r^2} + u_{zz} - \frac{2v_\theta}{r^2} - \frac{u}{r^2}\right) \quad (1.84)$$

$$v_t + \overline{w}u_z = -\frac{p_\theta}{r} + \frac{1}{Re}\left(v_{rr} + \frac{v_r}{r} + \frac{v_{\theta\theta}}{r^2} + v_{zz} - \frac{2u_\theta}{r^2} - \frac{v}{r^2}\right) \quad (1.85)$$

$$w_t + u\overline{w_r} + \overline{w}w_z = -p_z + \frac{1}{Re}\left(w_{rr} + \frac{w_r}{r} + \frac{w_{\theta\theta}}{r^2} + w_{zz}\right) \quad (1.86)$$

where subscripts denote partial derivatives with respect to the cylindrical coordinates (r, θ, z). The statement of incompressibility $\nabla \cdot \mathbf{V}$ in cylindrical coordinates is

$$u_r + \frac{v_\theta}{r} + w_z + \frac{u}{r} = 0 \quad (1.87)$$

Solving this system using a Fourier-Chebyshev-Galerkin spectral method, Meseguer & Trefethen[17] showed that the parabolic laminar profile is linearly stable to $Re = 10^7$. Their approach yielded eigenvalues for Fourier modes $n = 1, k = 0$ and $n = 1, k = 1$. As shown in Fig.1.4, all eigenvalues has negative real part, indicating the linear stability of the laminar solution.

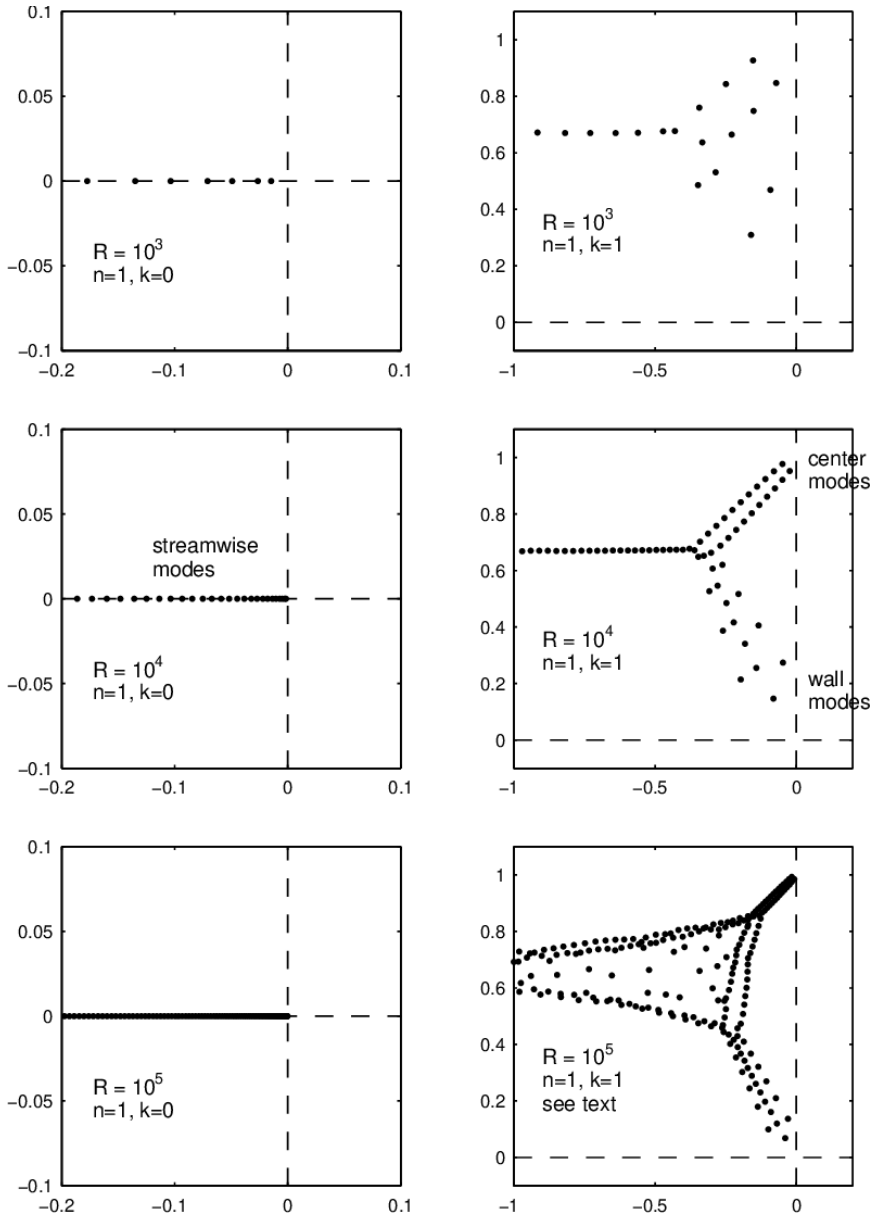

Figure 1.4: Linear stability of pipe flow as determined by Meseguer & Trefethen[17]. Numerically computed eigenvalues in the complex plane for $n = 1$ and $k = 0, 1$ with $Re = 10^3, 10^4, 10^5$. All eigenvalues have zero real part, indicating linear stability of the parabolic Hagen-Poiseuille velocity profile for an infinitely long pipe.

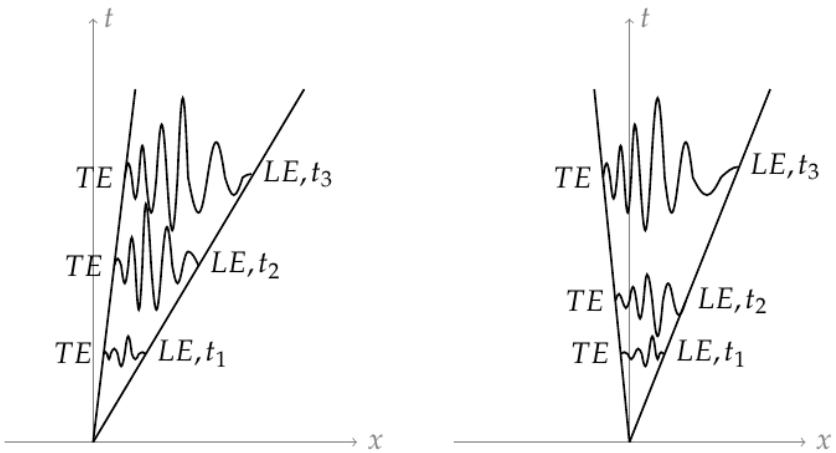

(a) Convective instability (b) Absolute instability

Figure 1.5: Absolute versus convective instability.

1.7.5 Absolute stability versus convective instability

The preceding discussions on eigenvalues is necessarily a discussion of the absolute stability of a solution. However, other instabilities may arise, including convective instabilities in open systems such as pipe flow and channel flow. Notably, metastable *noise-sustained* structures may arise in convectively unstable systems subject to small disturbances in the inlet of the system. See Fig.1.5

Sensitivity to inlet conditions, despite linear stability of the flow, is reminiscent of convectively unstable systems[18][19]. Plane Poiseuille flow is absolutely stable for Reynolds numbers $Re < 5772$[20] but sees turbulent structures well below that. Barkley's original pipe model, discussed in Chapter 5, can also be convectively unstable on certain domains, permitting chaotic behavior and additional solutions not seen in periodic domains mimicking infinitely long pipes.

1.8 Coherent structures and exact solutions of the NSE

In general, two categories of structures in pipe flow are of interest to us. The first set are the fundamental elements of Periodic Orbit Theory (POT): the numerically-exact solutions

to the Navier-Stokes equations—including traveling waves (TW), periodic orbits (PO), and relative periodic orbits (RPO)—the heteroclinic connections that tether the solutions together in state space, and the stable and unstable manifolds of each solution.

The second type of structures are the characteristic localized patches of turbulence ("spots" in 2D flows, "puffs" and "slugs" in pipe) that pervade the transitional regime but are not themselves solutions to the NSE. Both kinds of structures exist during the transitional regime.

Solutions to the NSE are known to localize as domain size increases; current understanding is that localization occurs through a subharmonic bifurcation of key wavenumbers[21][22] .

1.9 Patterns

1.9.1 Fluid flow as nonequilibrium phenomenon

Myriad mechanisms are used to drive fluidic systems out of equilibrium, causing the flow of fluid. Most commonly, wall shear stresses or pressure gradients drive the fluid, as is the case with cylindrical pipe, plane Couette, plane Poiseuille and Taylor-Couette flows. However, these are not the only mechanisms for driving fluid. Some Kolmogorov flows, for example, rely on a sinusoidally varying magnetic field to move a ferrofluid, and the Rayleigh-Bénard system relies on a temperature gradient to induce convection. Regardless, the nonuniformity induced by the driving mechanism means that the system is not in state of thermal equilibrium. Further, the requirement of an external driving mechanism necessitates contact with an external system or reservoir. Consequently, sustained fluid flows are, by definition, open nonequilibrium systems.

Crucially, the relative strength of the driving mechanism is described by a dimensionless quantity that parameterizes the flow. Cross and Greenside explain[16]:

There are mechanisms that can drive a system out of thermodynamic equilib-

rium, such as a flux of energy, momentum, or matter through the system. This driving is opposed by one or more dissipative mechanisms such as viscous friction, heat conduction, or electrical resistance that restore the system to thermal equilibrium. The relative strength of the driving and dissipative mechanisms can often be summarized in the form of one or more dimensionless parameters, e.g. the Rayleigh number R in the case of convection. Nonequilibrium systems often become unstable and develop an interesting spatiotemporal pattern when the dimensionless parameter exceeds some threshold, which we call the critical value of that parameter.

For many of the fluid flows being discussed in this document, the dimensionless quantity is the Reynolds number Re, which can be thought of as the ratio of inertial forces to viscous forces (or, if the reader prefers, the ratio of inertial to viscous timescales):

$$Re = \frac{\text{inertial}}{\text{viscous}} \tag{1.88}$$

where the inertial forces are related to the quantities that drive the flow and the viscous to the forces that dissipate energy. As a general rule, when the relevant inertial force far exceeds the viscous, turbulence erupts.

In pipe with a fixed circular cross section, the inertial forces are related to the momentum flux induced by a pressure or mass gradient. That is,

$$Re = \frac{\text{momentum flux}}{\text{viscosity}} = \frac{\rho\, \Delta V\, \Delta x}{\mu}$$

Here, ρ is the density of the fluid, ΔV is a characteristic difference in velocity between two parcels of fluid separated by a characteristic length Δx, and μ is the dynamic viscosity. The larger the difference in momentum flux between two regions of the fluid, the larger viscosity must be to even out momentum variations and keep the fluid moving smoothly (*laminar flow*). When Re is small ($Re \ll 1$), flow will be smooth (laminar). Conversely,

when Re is large ($Re \gg 1$), neighboring particles of fluid may move at very different velocities—that is, fluid parcels may exhibit large variations in momentum—giving rise to complex *turbulent* flow.

By convention, the characteristic distance Δx described above is taken to be the diameter D of the pipe. Thus, Reynolds number for pipe is

$$Re_{pipe} = \frac{\overline{V}D}{\nu} \quad \text{(pipe)} \tag{1.89}$$

where $\overline{V}$ is the mean speed of the fluid through the pipe and and $\nu \equiv \mu/\rho$ is the kinematic viscosity. In the absence of a gradient to drive the flow, the viscous forces would restore equilibrium by bringing all fluid to dynamic equilibrium. Because of the no-slip boundary condition at the walls,

$$\mathbf{V} \times \hat{r}\Big|_{\partial\Omega} = 0 \quad \text{where} \quad \partial\Omega \equiv r = D/2 \tag{1.90}$$

$V \to 0$ for all the fluid in the pipe in the absence of an external driving mechanism. Thus, the only equilibrium fluid state is that corresponding to no flow at all. It follows then that all sustained flows are nonequilibrium states.

Pipe flow is the prototype for the study of fluid flows, but it is hardly the only one of interest to physicists. Two-dimensional plane Couette flow (Figures 1.6 and 1.8) is a canonical flow whereby two infinite parallel plates move in opposite directions with speed U, resulting in a shear stress that drives the flow. The relevant Reynolds number is similar to that for pipe:

$$Re_{pc} = \frac{Uh}{\nu} \quad \text{(plane Couette)} \tag{1.91}$$

where $2h$ is the gap between the two plates, U is the speed of the plates, and ν is the kinematic viscosity.

Another effectively two-dimensional system is Taylor-Couette. Taylor-Couette flow is driven out of equilibrium by a velocity gradient between two concentric cylinders (either one cylinder stationary and the other rotating relative to it, or the inner and outer cylinders counter rotating) and, as a result, has two relevant Reynolds numbers, one for the inner cylinder and one for the outer cylinder:

$$R_i = \frac{\omega_i r_i (r_o - r_i)}{\nu} \quad , \quad R_o = \frac{\omega_o r_o (r_o - r_i)}{\nu} \quad \text{(Taylor-Couette)} \tag{1.92}$$

Interestingly, as the ratio of the two cylinder radii goes to unity ($r_o/r_i \to 1$)—that is, as the radii of the two cylinders both go infinitely large—the character of the Taylor-Couette flow is expected to approach that of plane Couette[23].

In the two-dimensional Kolmogorov flow described by [24], a shallow electrolytic fluid is driven by an externally applied magnetic field[25] and the relevant Reynolds number is

$$Re_k = \sqrt{\frac{\lambda^3 \chi}{8\nu^2}} \quad \text{(Kolmogorov)} \tag{1.93}$$

where the sinusoidal forcing is $f = \chi \sin(\kappa y)\hat{x}$, ν is the kinematic viscosity, and $\lambda = 2\pi/\kappa$.

In Rayleigh-Bénard convection (Figure 1.7), a temperature gradient is applied to drive flow[16]. The useful parameter is proportional to the temperature gradient that drives the convection and is called the Rayleigh number R_{RB}:

$$R_{RB} = \frac{\alpha g d^3 \Delta T}{\nu \kappa} \quad \text{(Rayleigh-Bénard)} \tag{1.94}$$

where α is the coefficient of expansion for the fluid, g is gravitational acceleration, d is the depth of the fluid, ν is the kinematic viscosity, and κ is the fluid's thermal diffusivity.

Here we have listed several disparate nonequilibrium fluid flows with different driving mechanisms and different geometries. Yet, despite their differences, they share one important feature: they exhibit pattern formation during the transition to turbulence.

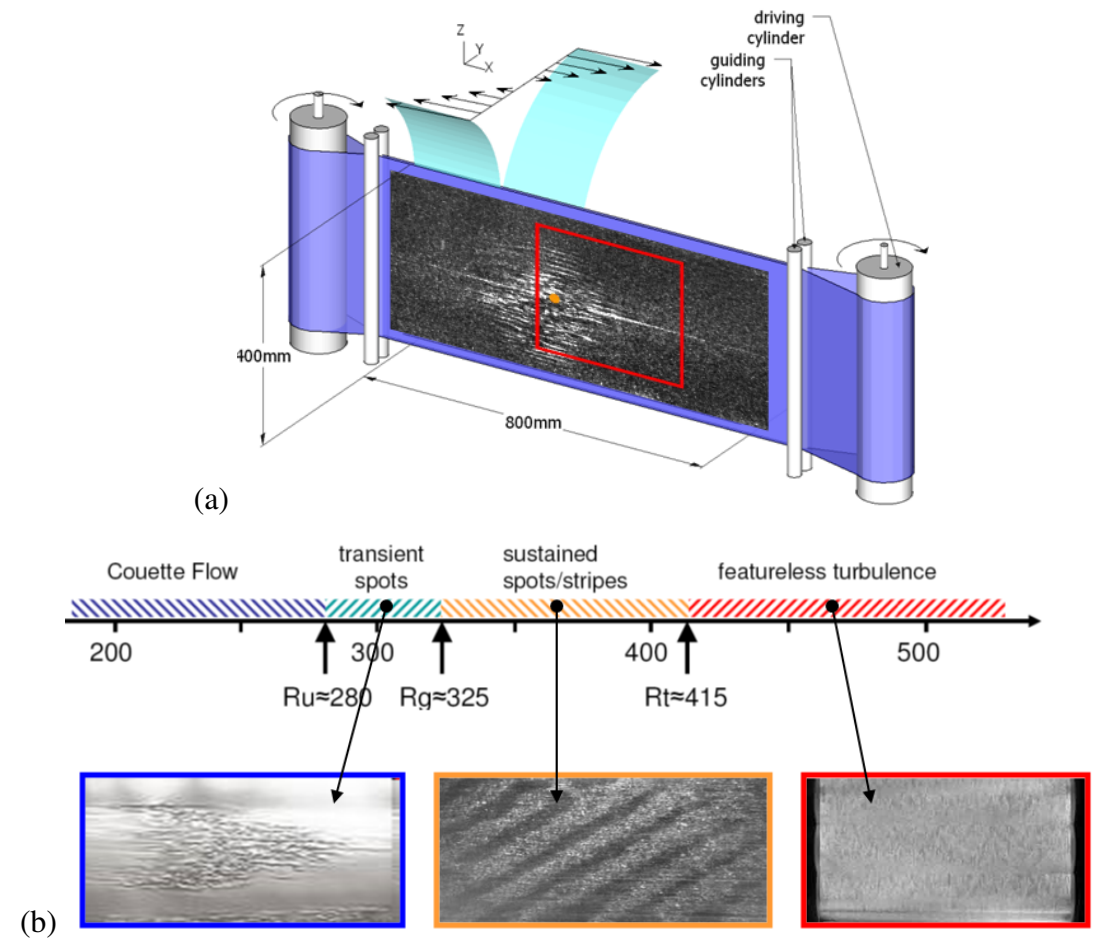

Figure 1.6: (a) Experimental set-up for plane Couette. (b) The transition to turbulence in plane Couette. As with other flows discussed in this paper, the transition follows the localized spot $\rightarrow$ spatially periodic pattern $\rightarrow$ featureless turbulence route.

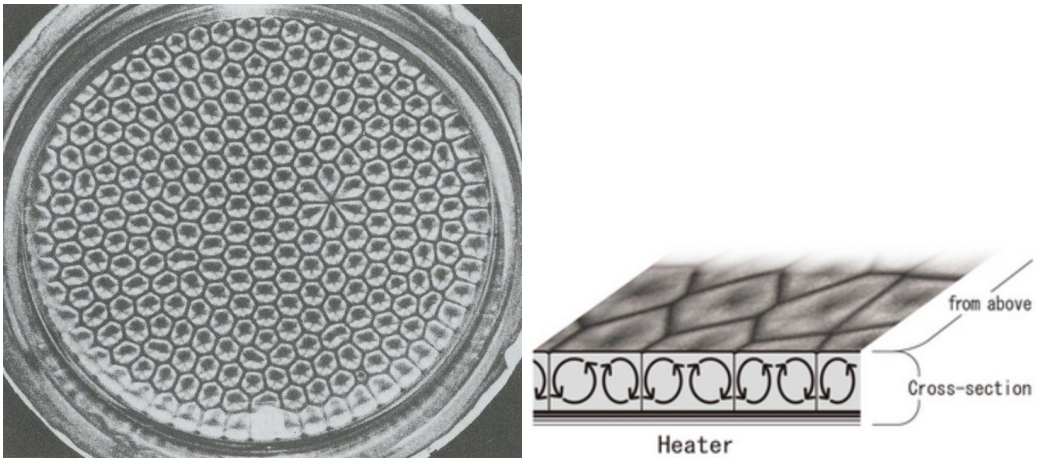

Figure 1.7: (a) The Rayleigh-Bénard experiment as seen from above. (b) Cross-section of the Rayleigh-Bénard convective cells.

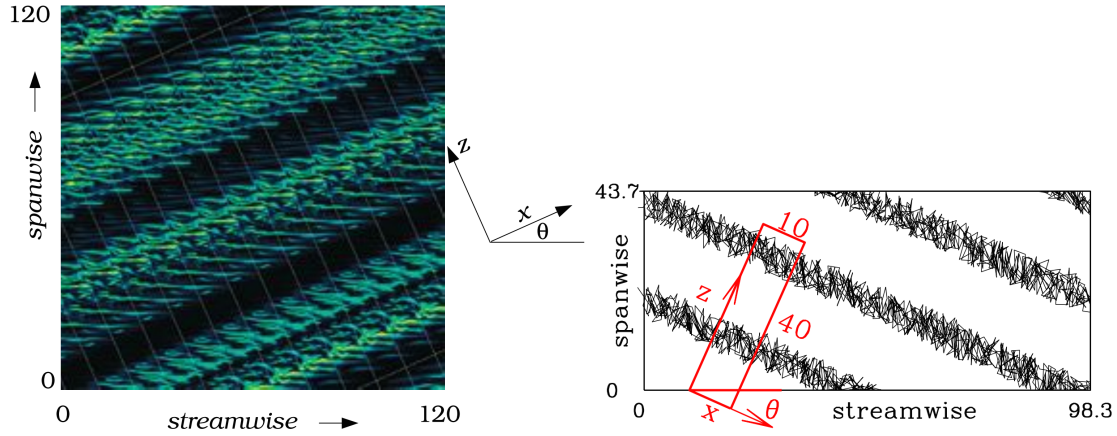

Figure 1.8: (a) Barkley and Tuckerman observe stripe patterns in plane Couette simulations. (b) Stripes seen in numerical simulations of plane Poiseuille flow.

1.9.2 The role of patterns in the transition to turbulence

Patterns in two-dimensional incompressible fluid flows

In 1965, Coles[26] first observed spiral patterns in counter-rotating Taylor-Couette flow. Pringent, *et al.*[27] found that large aspect plane Couette flow exhibits spot and stripe patterns during the turbulent transition. Likewise, banded patterns are observed in plane Poiseuille flow[4].

Pringent, *et al.*[27] found that large-aspect plane Couette flow exhibits tell-tale patterns during the turbulent transition. Like the patterns first seen by Coles in Taylor-Couette, the patterns seen in plane Couette are distinct spatially-periodic bands of coexisting turbulent and laminar flow with a well-defined wavelength. Direct numerical simulations conducted by Barkley and Tuckerman confirmed the existence of these patterns. They observe: "It now appears that turbulent-laminar patterns are inevitable intermediate states on the route from turbulent to laminar flow in large aspect ratio plane Couette flow."[28]. See Figure 1.8.

Patterns in three-dimensional incompressible fluid flows: Pipe

The quintessential three-dimensional fluid flow, and the one Reynolds himself focused on, is that of cylindrical pipe flow. In pipe, coherent turbulent structures called puffs and slugs analogize to the spots, stripes, and bands seen in two-dimensional flows. In sufficiently long pipes, a regular array of puffs can be seen, with a more or less fixed separation of $\sim 20 - 25D$ between neighboring puffs[5], evocative of the preferred wavelengths for stripes seen in two-dimensional flows and indicative of an interaction distance between neighboring puffs. Puffs and slugs, like spots and stripes in 2D systems, are energy dissipating structures.

Our understanding of pattern formation in pipe flow is limited, and is currently an active research topic[4]. It is well-accepted that turbulent puff and slug patterns seen in three-dimensional pipe analogize to localized spots and stripes seen in two-dimensional fluid flows, but the mechanisms underlying pattern formation are even less-understood in pipe than in two-dimensional flows. Knobloch notes in a 2008 review[30],

> *Even more problematic is the case of patterns localized in two or three spatial dimensions since there appears to be no way of dealing simultaneously with more than one time-like variable. In fact, to the author's knowledge, there have been no studies of fully three-dimensional localized structures, despite the fact that such structures are expected to form in subcritical Turing bifurcations in three-dimensional media.*

That said, the recent work of Reetz *et al.*[31] suggests a possible course of investigation for pipe: continuation of a traveling wave solution that undergoes a pattern-forming bifurcation leading to a long wavelength modulation of the underlying periodic solution.

[5] Samanta, *et al.*: "[T]urbulent puffs have a well-defined interaction distance, which sets their minimum spacing as well as the maximum observable turbulent fraction."[29]

1.9.3 Turing patterns as nonequilibrium phenomena

The Second Law of [equilibrium] Thermodynamics states that an isolated system will evolve in such a way as to maximize total entropy[6]. However, the emergence of structure or pattern in a system indicates a decrease in local entropy. Thus, patterns—in particular, Turing patterns—can only occur in open systems, and any *local* decrease in entropy due to pattern formation is met with an even larger increase in total entropy of the external environment[32].

Quoting D. Bullara and Y. De Decker[33]:

> *[Turing] structures are a class of spatiotemporal organizations that can be obtained only far from equilibrium, where a system can continuously dissipate entropy in its environment, which compensates the entropy produced by the internal irreversible processes and keeps the system in an organized state.*

The patterns seen in transitionally turbulent regime in canonical fluid flows are suggestive of Turing patterns seen in two-dimensional reaction-diffusion-advection systems[7]. We are thus prompted to review the mechanism behind Turing patterns.

1.9.4 Turing patterns: general mathematical treatment

Author's Note: Elementary mathematical treatments of Turing instabilities are readily found; Cross and Greenside's text[16] is one such reference.

The surprising discovery found by Turing is that a spatially homogeneous solution may be stable in the absence of diffusion but can destabilize when subjected to nonuniform perturbations in the presence of diffusion. To see this, consider a general reaction diffusion

[6] Despite much effort, a "law of entropy" for nonequilibrium systems, analogous to the Second Law of Thermodynamics for equilibrium systems, remains elusive. Some have speculated that entropy production rates should be a minimum; others have suggested entropy production rates should be a maximum. Neither seems correct.

[7] Less is understood about Turing patterns in three dimensions, but the author has found some interesting articles, including [34].

system involving [at least] two different interacting species of the form

$$\begin{aligned}\frac{\partial u_1}{\partial t} &= D_1 \nabla^2 u_1 + f_1(u_1, u_2) \\ \frac{\partial u_2}{\partial t} &= D_2 \nabla^2 u_2 + f_2(u_1, u_2)\end{aligned} \tag{1.95}$$

where $u_i = u_i(x,t)$ depend on space and time, D_i are the respective diffusion coefficients, and f_i are the reactive terms, which may be linear or nonlinear. For simplicity, we assume the diffusion coefficients are constant and independent of spatial location, time, and the values of u_i.

When $f_1(u_1, u_2) = f_2(u_1, u_2) = 0$, a stationary and uniform solution emerges: a homogeneous solution. Near the homogeneous solution, which we denote as $\mathbf{u}^*$, the linearized system of equations is

$$\begin{aligned}\frac{\partial\ \delta u_1}{\partial_t} &= D_1 \frac{\partial^2\ \delta u_1}{\partial x^2} + a_{11}\ \delta u_1 + a_{12}\ \delta u_2 \\ \frac{\partial\ \delta u_2}{\partial_t} &= D_2 \frac{\partial^2\ \delta u_2}{\partial x^2} + a_{21}\ \delta u_1 + a_{22}\ \delta u_2\end{aligned} \tag{1.96}$$

where δu_1 and δu_2 are infinitesimal perturbations of the homogeneous state. Define A and the diffusion matrix D: We can express the system in the more compact vector form as

$$\frac{\partial \mathbf{u}^*}{\partial t} = \mathbf{D} \frac{\partial^2 \mathbf{u}^*}{\partial x^2} + \mathbf{A}\mathbf{u}^* \tag{1.97}$$

On an infinite domain or a domain with periodic boundary conditions, the system maintains translationally invariant and we can expect particular solutions of the form

$$\delta \mathbf{u} = \delta \mathbf{u}\ e^{\lambda_k t + ikx} \tag{1.98}$$

where $\lambda_k > 0$ ($\lambda_k < 0$) describes growth (decay) of the solutions, and k are wavenumbers.

Substituting this solution into the linearized equation, we arrive at an eigenvalue problem:

$$\mathbf{A}_k \ \delta\mathbf{u}_k = \lambda_k \ \delta\mathbf{u}_k \tag{1.99}$$

with the corresponding characteristic equation: Solving for the eigenvalues,

$$\lambda_k = \frac{1}{2} Tr\mathbf{A}_k \pm \frac{1}{2}\sqrt{(Tr\mathbf{A}_k)^2 - 4\det \mathbf{A}_k} \tag{1.100}$$

Stability is assured when the real part of eigenvalue is negative, i.e. $\mathrm{Re}\,(\lambda_k) < 0$, for all wavenumbers, or equivalently when

$$Tr\mathbf{A}_k = a_{11} + a_{22} - (D_1 + D_2)k^2 < 0 \tag{1.101}$$

$$\det \mathbf{A}_k = (a_{11} - D_1 k^2)(a_{22} - D_2 k^2) - a_{12}a_{21} > 0 \tag{1.102}$$

For the homogeneous steady state in the absence of diffusion (where $D_i = 0$), the stability conditions are

$$a_{11} + a_{22} < 0 \tag{1.103}$$

$$a_{11}a_{22} - a_{12}a_{21} > 0 \tag{1.104}$$

In the presence of diffusion, the condition for linear stability is

$$D_1 a_{22} + D_2 a_{11} > 0 \tag{1.105}$$

The homogeneous state will destabilize, however, when

$$\frac{D_2}{D_1} > -\frac{a_{22}}{a_{11}} \tag{1.106}$$

We conclude that Turing pattern formation will not occur unless the two diffusion coeffi-

cients differ substantially.

We can define characteristic diffusion lengths

$$l_1 = \sqrt{\frac{D_1}{a_{11}}} \quad , \quad l_2 = \sqrt{\frac{D_2}{a_{22}}} \tag{1.107}$$

which allows us to write the critical wavenumber k_c in terms of these characteristic lengths:

$$k_c^2 = \frac{1}{2}\left(\frac{1}{l_1^2} - \frac{1}{l_2^2}\right) > \sqrt{\frac{a_{11}a_{22} - a_{12}a_{21}}{D_1 D_2}} \tag{1.108}$$

which implies that l_2 must be sufficiently larger than l_1 to induce a Turing instability.

The treatment above applies to multi-species systems on an infinite spatial domain. Cross and Greenside emphasize that finite systems can admit different solutions [16]:

> *[These equations] cannot accurately describe a sustained nonequilibrium chemical system since they lack a transverse confined coordinate along which reactants can be fed into the system and products removed. The neglect of a confined coordinate is a major simplification. Indeed, an accurate treatment of the feed direction introduces complicated spatial structure...which makes the linear stability analysis considerably harder.*

A finite domain lacks translational invariance. For such a system, a superposition of

$$\exp \lambda_k t \exp ik \cdot x_\perp \tag{1.109}$$

terms, rather than a single Fourier mode, is required to satisfy the linearized problem. Wavevectors for which $\mathrm{Re}\,(\lambda_k) < 0$ will be damped, whereas other wavevectors that satisfy $\mathrm{Re}\,(\lambda_k) > 0$ will grow exponentially until grounded by nonlinearities. Dispersion relations tell us the growing modes and predict the characteristic length scale of the pattern, $\lambda_c = 2\pi/k_c$ that emerges just beyond the onset of the instability.

In a three-dimensional discretized isotropic system, the wavenumber k is given by

$$k = |\mathbf{k}| = 2\pi\sqrt{\left(\frac{n_x}{L_x}\right)^2 + \left(\frac{n_y}{L_y}\right)^2 + \left(\frac{n_z}{L_z}\right)^2} \tag{1.110}$$

where L_i denotes the system size in the ith direction and n_i the relevant index of the corresponding wavevector. We observe that the system isotropy introduces a degeneracy into the problem: multiple wavevectors can correspond to single unstable wavenumber. If k_c is unstable for one such wavevector, it will likewise be unstable for the others, as well. Which degenerate modes, and ultimately which pattern will be "selected", must be determined from a *nonlinear* analysis of the problem.

1.10 Patterns in two-dimensional incompressible fluid flows

In 1965, Coles[26] first observed spiral patterns in counter-rotating Taylor-Couette flow. Prigent, *et al.*[35] found that large aspect plane Couette flow exhibits spot and stripe patterns during the turbulent transition. Likewise, banded patterns are observed in plane Poiseuille flow[4].

Prigent, *et al.*[35] found that large-aspect plane Couette flow exhibits tell-tale patterns during the turbulent transition. Like the patterns first seen by Coles in Taylor-Couette, the patterns seen in plane Couette are distinct spatially-periodic bands of coexisting turbulent and laminar flow with a well-defined wavelength. Direct numerical simulations conducted by Barkley and Tuckerman confirmed the existence of these patterns. They observe: "It now appears that turbulent-laminar patterns are inevitable intermediate states on the route from turbulent to laminar flow in large aspect ratio plane Couette flow."[28].

1.11 Patterns in three-dimensional incompressible fluid flows

The quintessential three-dimensional fluid flow, and the one Reynolds himself focused on, is that of cylindrical pipe flow. In pipe, coherent turbulent structures called puffs and slugs

analogize to the spots, stripes, and bands seen in two-dimensional flows. In sufficiently long pipes, a regular array of puffs can be seen, with a more or less fixed separation wavelength/separation between neighboring puffs, evocative of the preferred wavelengths for stripes seen in two-dimensional flows. Puffs and slugs, like spots and stripes in 2D systems, are energy dissipating structures.

Our understanding of pattern formation in pipe flow is limited, and is currently an active research topic[4]. It is well-accepted that turbulent puff and slug patterns seen in three-dimensional pipe analogize to localized spots and stripes seen in two-dimensional fluid flows, but the mechanisms underlying pattern formation are even less-understood in pipe than in two-dimensional flows. Knobloch notes in a 2008 review[30],

> *Even more problematic is the case of patterns localized in two or three spatial dimensions since there appears to be no way of dealing simultaneously with more than one time-like variable. In fact, to the author's knowledge, there have been no studies of fully three-dimensional localized structures, despite the fact that such structures are expected to form in subcritical Turing bifurcations in three-dimensional media.*

1.12 A connection between an ECS and pattern formation

The connection between exact numerical solutions of the NSE and pattern formation in fluid flows has been a recent line of inquiry. In 2019, Reetz, *et al.* found that a stripe pattern in plane Couette flow emerges from the Nagata equilibrium solution. Specifically, they found that a sequence of pattern-forming bifurcations from the Nagata solution leads to a large-scale modulated stripe pattern (see Fig.1.9). At the time of this writing, a connection between an ECS in pipe and spatiotemporal intermittency (e.g. alternating tubulent-laminar regions) has not been found but initial observations of long-pipe solutions hint that a similar result may hold for pipe as well.

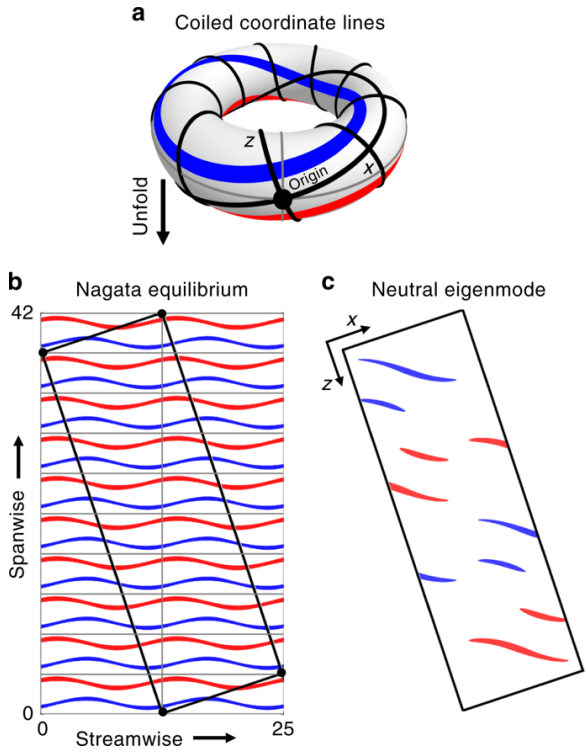

Figure 1.9: Stripe pattern in plane Couette emerges from Nagata equilibrium solution.

1.13 Organization of Dissertation

This document is outlined as follows: Chaper 2 provides an overview of the methodologies employed during the work. Chapters 3 and 4 feature published work regarding invariant solutions in pipe [36, 37]. Chapter 5 presents a published paper concerning the discovery of periodic solutions and chaos in Barkley's pipe model[38]. Conclusions are presented in Chapter 6 which also itemizes some possible extensions of the work presented here.

Note: All fluids discussed in this document are assumed incompressible, obeying the incompressibility condition, $\nabla \cdot \mathbf{V} = 0$.

CHAPTER 2

METHODOLOGY: THE EXACT

2.1 Periodic orbit theory in a nutshell

In the dynamical systems approach, solutions to the NSE are regarded as fixed points in state space, objects anchored in a high-dimensional pinball machine where the time evolution of the system is treated as a pinball bouncing from one solution to the next via solutions' stable and unstable manifolds and the heteroclinic connections that directly link one solution to another. Most solutions have a combination of stable and unstable eigenvectors and are therefore saddles in state space with some directions (eigenvectors) being attractive and others being repulsive. Further, how attractive or how repulsive a solution is depends on the size and number of its eigenvalues. The traveling wave solutions reported in Sections 3 and 4 have a larger number of unstable eigenvalues than do the RPOs, and the magnitudes of the TWs' most unstable eigenvalues exceeded that of most RPOs. The expectation then was that the flow dynamics in the pipe would spend more time near RPOs than TWs; observations of many simulations verified this hypothesis.

Periodic Orbit Theory (POT) predicts that a weighted average of a large number of computationally-extracted invariant solutions of the NSE will reproduce the turbulence statistics obtained from laboratory experiments. But before POT can be tested, a large number of invariant solutions must first be found. Finding solutions is a two-step process: First, a direct numerical simulation (DNS) of a pipe flow is run with the flow state of the system recorded at regular time intervals; from the recorded states a recurrence diagram (Figure 2.1) is generated from which the observer identifies possible recurring flows. Next, the candidate states corresponding to possible recurring flows—those that might be in the state space neighborhood of a TW or RPO—is put into a Newton-Krylov solver to see if it

converges to an invariant solution. The likelihood of convergence of a solution is improved by the removal of any unphysical symmetries. Thus symmetry reduction is embraced.

Once a solution has been found, it may be parametrically continued to smaller or larger values of Re or pipe length L using arclength continuation. Arclength continuation is not without its obstacles, though. Bifurcations and termination of solution branches can halt continuations. Further, as a solution is continued to increasing Re and L, it acquires more and more unstable eigenvalues, making it hard to track.

2.2 Numerical Approach

Direct numerical simulation in this dissertation was conducted using an open source hybrid spectral finite-difference code, Open Pipe Flow[39] created by collaborator A.P. Willis. To simulate pipe flow, we consider an incompressible newtonian fluid driven through a horizontal pipe of length L with circular cross section of radius $r = D/2$ and fixed mass flux in the axial direction. The NSE are formulated in standard cylindrical-polar coordinates (r, θ, z) with r the radial, θ the azimuthal, and z the axial coordinates, respectively. The full velocity field is decomposed into laminar and fluctuating components $\mathbf{U}(r) + \mathbf{u}$ and represented by $[u, v, w, p](r, \theta z)$ with u the radial velocity component of the flow, v the azimuthal component of the flow, w the streamwise (axially-directed) velocity component, and p the pressure.

The governing equations are thus,

$$\frac{\partial \mathbf{u}}{\partial t} + \mathbf{U}\cdot\nabla\mathbf{u} + \mathbf{u}\cdot\nabla\mathbf{U} + \mathbf{u}\cdot\nabla\mathbf{u} = -\nabla p + 32\frac{\beta}{Re}\hat{\mathbf{z}} + \frac{1}{Re}\nabla^2\mathbf{u} \quad , \quad \nabla\cdot\mathbf{u} = 0 \quad (2.1)$$

The laminar Hagen-Poiseuille profile is taken to be $\mathbf{U}(r) = 2(1-(2r))^2\hat{\mathbf{z}}$ and $Re = UD/\nu$ where U is the mean speed of the flow, D is the pipe diameter, and ν is the kinematic viscosity. The density of the fluid is assumed to be unity. Here $\beta = \beta(t)$ is the fractional pressure gradient required to maintain a contain the constant mass flux beyond that needed

to induce the laminar flow.

The numerical domain is periodic along the pips axis so that $u(r, \theta, z) = u(r, \theta, z + L)$ where $L = \pi/\alpha$ is the length of the pipe. The code is a hybrid spectral code with Fourier modes in the axial and azimuthal directions and Chebyshev in the radial variable. The deviation velocity field $\mathbf{u}$ is expanded accordingly:

$$\mathbf{u}(r_n, \theta, z, t; \alpha, m_o) = \sum_{k=-K}^{K} \sum_{m=-M}^{M} \mathbf{u}_{nkm}(r, t)\, e^{i(m_o m\theta + 2\alpha kz)} \tag{2.2}$$

where m_o is the order of the discrete rotational symmetry, e.g. in a flow constrained to a 4-fold azimuthally symmetric pipe, $m_o = 4$.

Typical resolutions were $N = 64$ finite-difference points in the radial direction, $M = 12$ Fourier modes in the azimuthal direction, and a variable number of axial Fourier modes depending on length of the pipe, from $K = 18$ in the shortest $7.4R$-length pipe up to $K = 360$ modes in the $L = 55R$ pipe. With a 9-point stencil, the resolution is $\mathcal{O}(8MNK)$; thus the $7.4R$ pipe has resolution of over 110,000 and the longest length pipe studied over 2.2 million.

2.3 Poisson-Pressure Equation

The Pressure Poisson Equation can be used to construct a system of equations, with attendant boundary conditions, equivalent to the incompressible Navier-Stokes equations. Consider an incompressible velocity field $\mathbf{u}(\mathbf{x}, t)$ on the domain Ω with a piecewise smooth boundary $\partial\Omega$ that satisfies the NSE with boundary conditions

$$\mathbf{u} = \mathbf{g}(\mathbf{x}, t) \quad \text{for} \quad \mathbf{x} \in \partial\Omega \tag{2.3}$$

Because an incompressible fluid must have zero flux through the boundary at $r = R$,

$$\int_{\partial\Omega} \hat{r} \cdot \mathbf{g} \, dA = 0 \tag{2.4}$$

where $\hat{r}$ is the outward normal on the boundary and dA is an area element on $\partial\Omega$. The initial conditions are

$$\mathbf{u}(\mathbf{x}, 0) = \mathbf{u_o} \quad \text{for} \quad \mathbf{x} \in \Omega \tag{2.5}$$

$$\nabla \cdot \mathbf{u}_o = 0 \quad \text{for} \quad \mathbf{x} \in \Omega \tag{2.6}$$

$$\mathbf{u}_o(\mathbf{x}) = \mathbf{g}(\mathbf{x}, 0) \quad \text{for} \quad \mathbf{x} \in \partial\Omega \tag{2.7}$$

and the no-flux, no-slip boundary conditions at the fixed impermeable walls can be expressed as

$$\mathbf{u} \cdot \hat{r} = 0 \tag{2.8}$$

$$\mathbf{u} \times \hat{r}|_{\partial\Omega} = 0 \tag{2.9}$$

To obtain the pressure equation, we first take the divergence of the momentum equation and apply the incompressibility constraint. This yields a Poisson equation for the pressure:

$$\nabla^2 p = -\nabla \cdot (\mathbf{u} \cdot \nabla \mathbf{u}) \tag{2.10}$$

This additional equation introduces an additional boundary condition that permits replacing the NSE with

$$\mathbf{u} + (\mathbf{u} \cdot \nabla)\, \mathbf{u} = \mu \nabla^2 \mathbf{u} - \nabla p \tag{2.11}$$

$$\nabla^2 p = -\nabla \cdot (\mathbf{u} \cdot \nabla \mathbf{u}) \tag{2.12}$$

with boundary conditions

$$\mathbf{u} = \mathbf{g}(\mathbf{x}, t) \tag{2.13}$$

$$\nabla \cdot \mathbf{u} = 0 \quad \text{for} \quad \mathbf{x} \in \partial\Omega \tag{2.14}$$

This additional boundary condition ensures that the pressure enforces incompressibility throughout the flow.

2.4 Newton-Krylov Solver

The solutions hunted during this work included traveling waves (TW) possessing translational invariance long the pipe axis $\hat{z}$:

$$V(r, \theta, z; t) = V(r, \theta, z - ct) \tag{2.15}$$

with phase speed c, and relative periodic orbits (RPOs) having both translational invariance (moving at speed $\overline{c}$) and dynamical periodicity of period T_p

$$V(r, \theta, z; t) = V(r, \theta, z - \overline{c}t; t + T_p) \tag{2.16}$$

In a frame of reference co-moving with the solutions, the TW appears as a relative equilibrium and the RPO appears as a traveling wave. To find solutions, we consider a recurrent flow $\mathbf{u}$ and a nonlinear function $\mathbf{f}(\mathbf{u})$ such that:

$$\mathbf{f}(\mathbf{u}) = 0 \tag{2.17}$$

A Jacobian-free Newton-Krylov (JFNK) method is used to find the roots of the nonlinear function $\mathbf{f}(\mathbf{u})$. In the case of pipe flow, one takes advantage of the symmetries inherent in

the solutions to write $\mathbf{f}(\mathbf{u})$ as

$$\mathbf{f}\left(\mathbf{u}(0),t\right) = g(0,-ct)\mathbf{u}(t) - \mathbf{u}(0) = 0 \tag{2.18}$$

for a traveling wave solution with Galilean symmetry, where c is the streamwise phase velocity of the solution. Likewise, a relative periodic orbit solution that undergoes an axial shift l after time T_p, satisfies

$$\mathbf{f}\left(\mathbf{u}(0),t,l\right) = g(0,-l)\mathbf{u}(T_p) - \mathbf{u}(0) = 0 \tag{2.19}$$

starting with an initial guess for the fluid state with period T_p and axial shift l. Initial guesses for the algorithm are found with recurrence diagrams.

Recall that the Newton-Raphson method converges towards the roots x of the 1D function $f(x)$ by interating

$$x_{i+1} = x_i - \frac{f(x_i)}{f'(x_i)} \tag{2.20}$$

where $f' = df/dx$ and x_o is an initial guess. The iteration can also be expressed as

$$x_{i+1} = x_i + dx_i, \qquad f'(x_i)dx_i = -f(x_i) \tag{2.21}$$

Solving the linear system $f'(x_i)dx_i = -f(x_i)$ for the unknown dx_i supplies the update.

In higher dimensions, Newton's method is

$$\mathbf{x}_{i+1} + \mathbf{x}_i + d\mathbf{x}_i, \quad \left.\frac{\partial \mathbf{F}}{\partial \mathbf{x}}\right|_{x_i} = -\mathbf{F}(\mathbf{x}_i) \tag{2.22}$$

where $\mathbf{F}(x) = (f_1(x), f_2(x), f_3(x), ..., f_n(x))$ and each $f_i(x)$ maps a real n-vector x into a scalar in a continuous and differential way. The goal of the Newton method is to success-

fully solve a linear system, e.g.

$$\mathbf{J}(x)dx = -\mathbf{F}(x) \tag{2.23}$$

where

$$\mathbf{J}(x) = \left(\frac{\partial f}{\partial x_i}\right)_{n\times n} \tag{2.24}$$

is the Jacobian matrix of $\mathbf{F}(x)$. However, when n is large, evaluating the Jacobian matrix at each iteration of the Newton method is computationally expensive. Thus, an approximation to $\mathbf{J}(x)$ is desirable. Fortunately, Eq. 2.23 is has the form $\mathbf{A}d\mathbf{x} = \mathbf{b}$ which may be solved using the Krylov-subspace method, *generalized minimal residual method* (GMRES). The GMRES algorithm need not know the matrix $\mathbf{A}$ itself, only the result of multiplying a vector by $\mathbf{A}$. This Jacobian-free Newton-Krylov method (JFNK) combines a matrix-free approach with nonsymmetric Krylov subspace methods. It is a projection method for solving the linear system $\mathbf{A}d\mathbf{x} = \mathbf{b}$ using the Krylov subspace K_j:

$$K_j = span\left(r_o, Ar_o, A^2r_o, ..., A^{j-1}r_o\right) \tag{2.25}$$

where $r_o = b - Ax$.

Iterations of the GMRES algorithm involve calculating products of the Jacobian with the vector $d\mathbf{x}$, which may be approximated as

$$\frac{\partial \mathbf{F}}{\partial \mathbf{x}}dx \approx \frac{1}{\epsilon}\left(\mathbf{F}(\mathbf{x}_i + \epsilon dx)\right) - \mathbf{F}(\mathbf{x}_i) \tag{2.26}$$

for some small ϵ.

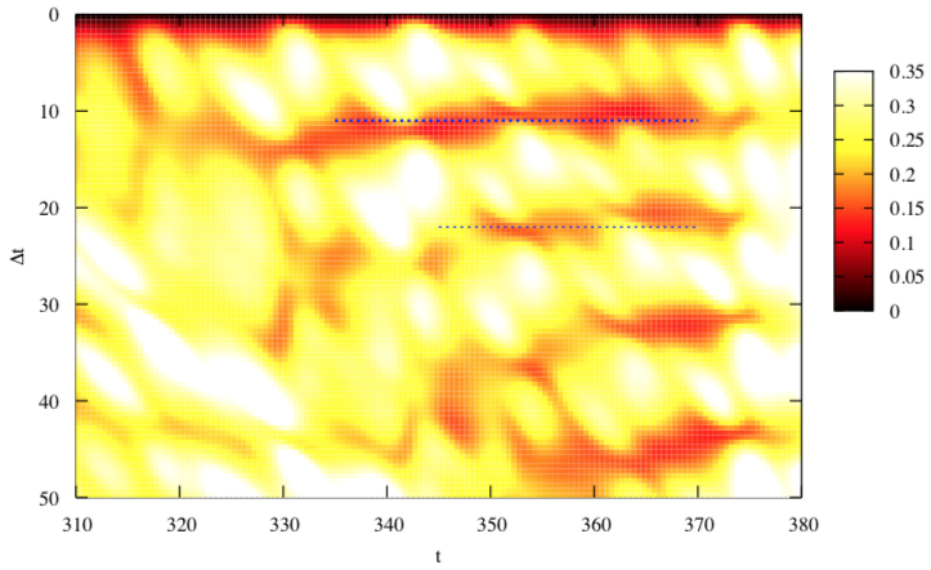

Figure 2.1: Recurrence diagrams used to identify initial guesses for Newton-Krylov. Here, minima around the horizontal lines suggest shadowing of a periodic orbit with temporal period $T_p \approx 11$.

2.5 Initial Guesses

Initial guesses for Newton searches are found with the aid of recurrence diagrams generated by plotting velocity flow states $\mathbf{u}$ at subsequent times according to,

$$\frac{\left|\left|\mathbf{u}_t - \mathbf{u}_{t-\Delta t}\right|\right|}{\left|\left|\mathbf{u}_{t-\Delta t}\right|\right|} \tag{2.27}$$

and looking for recurring minima. As an example, an examination of Fig. 2.1 finds repetition in the flow, signaled by the periodic minima of $\Delta t \approx 11$ (dashed horizontal lines in Fig. 2.1), suggesting the flow may have shadowed a relative periodic orbit of period $T_p \approx 11$.

Initial guesses for exact solutions of the incompressible Navier-Stokes equations (NSE) were put into a Newton-Krylov solver. For example, initial guesses for an RPO looked for

zeros of

$$\mathbf{f}(u(0), T_p, l) = g(0, -l), u(T_p) - u(0) = 0 \tag{2.28}$$

with an initial guess for a state u, period T_p, and shift l.

In addition to the continuous Galilean symmetries, most work was done in pipe with constrained azimuthal symmetry such that

$$(U, V, W)(r, \theta, z) \rightarrow (U, V, W)(r, \theta + 2\pi/m, z) \tag{2.29}$$

where m is the order of the rotational symmetry subspace, e.g. $m = 4$. Similarly, most solutions were found in the shift-and-reflect symmetry subspace where

$$(U, V, W)(r, \theta, z) \rightarrow (U, V, W)\left(r, \theta + \frac{\pi}{m}, z - \frac{\pi}{m}\right) \tag{2.30}$$

The wavelength of the solution is $2\pi/\alpha$.

CHAPTER 3
SYMMETRY REDUCTION IN HIGH DIMENSIONS, ILLUSTRATED IN A TURBULENT PIPE

3.1 Abstract

Equilibrium solutions are believed to structure the pathways for ergodic trajectories in a dynamical system. However, equilibria are atypical for systems with continuous symmetries, i.e. for systems with homogeneous spatial dimensions, whereas *relative* equilibria (traveling waves) are generic. In order to visualize the unstable manifolds of such solutions, a practical symmetry reduction method is required that converts relative equilibria into equilibria, and relative periodic orbits into periodic orbits. In this article we extend the fixed Fourier mode slice approach, previously applied 1-dimensional PDEs, to a spatially 3-dimensional fluid flow, and show that is substantially more effective than our previous approach to slicing. Application of this method to a minimal flow unit pipe leads to the discovery of many relative periodic orbits that appear to fill out the turbulent regions of state space. We further demonstrate the value of this approach to symmetry reduction through projections (projections only possible in the symmetry-reduced space) that reveal the interrelations between these relative periodic orbits and the ways in which they shape the geometry of the turbulent attractor.

3.2 Introduction

Chaotic dynamics can be interpreted as a trajectory in state space, where each coordinate corresponds to a degree of freedom. For higher-dimensional systems it can be difficult to predict which coordinate choices will provide the most instructive projections, given that plots of these trajectories are limited to displaying two or three dimensions at a time.

To avoid clutter in the projection caused by families of orbits related by translations or reflections, symmetry-invariant measures such as spatial averages are often favored. In practice, however, there are only so many quantities that may be averaged and, in addition, information held in the spatial structure is wiped out in the averaging process. Often such averaging results in a largely uninformative projection of the dynamics.

The study of turbulence is one example where substantial progress has recently been made by viewing the flow as a dynamical system, but now a more informative means of projection is required to comprehend the way in which the unstable manifolds of relative equilibria and other invariant solutions shape the dynamics. These invariant solutions correspond to recurrent but unstable motions[40] that share some characteristics with fully turbulent flows. Experiments[40, 41] and simulations[42, 43] have identified transient visits to spatiotemporal patterns that mimic traveling wave solutions. Certain low-dissipation traveling waves of the Navier-Stokes equations have been shown to be important in the transition to turbulence, where they lie in the laminar-turbulent boundary, separating initial conditions that ultimately relaminarize from those that develop into turbulence[44]. Spatiotemporal flow patterns called 'puffs' and 'slugs' are observed during the evolution to turbulence. Recently, spatially-localized solutions representative of puffs have been discovered[45] and shown to be linked to spatially-periodic traveling waves in minimal domains[46]. As traveling waves are steady in their respective co-moving frames, they are *relative* equilibria, solutions that do not exhibit temporal shape-changing dynamics. Their unstable manifolds, however, mold the surrounding state space, carving pathways for relative periodic orbits, invariant orbits embedded in turbulence whose temporal evolution captures dynamics of ergodic trajectories that shadow them. A detailed understanding of these recurrent motions is crucial if one is to systematically describe the repertoire of all turbulent motions. With the removal of spatial translations, which obscure visualizations of the dynamics, a far greater number of projections of chaotic trajectories is possible. In this article, we show that visualizations of the symmetry reduced dynamics can help us

understand relationships between distinct families of periodic orbits and traveling wave solutions, which in turn lends support to the dynamical systems interpretation that *relative* periodic orbits form the backbone of turbulence in pipe.

3.3 Results

Our approach is dynamical: writing the Navier–Stokes equations as $\dot{\boldsymbol{u}} = \boldsymbol{v}(\boldsymbol{u})$, the fluid state $\boldsymbol{u}$ at a particular moment in time is represented by a single point in state space $\mathcal{M}$[47]; turbulent flow is represented by an ergodic trajectory that wanders between accessible states in $\mathcal{M}$[48]. Essential to this analysis is that any two physically equivalent states be identified as a single state: a symmetry-reduced state space $\hat{\mathcal{M}} = \mathcal{M}/G$ is formed by contracting the volume of state space representing states that are identical except for a symmetry transformation to a single point $\hat{\boldsymbol{u}}$. Only after a symmetry reduction are the relationships between physically distinct states revealed. In this article symmetry reduction is implemented with an extension of the 'first Fourier mode slice' method[49], a variant of the method of slices[50]. The method of slices separates coordinates into phases along symmetry directions ('fibers', 'group orbits' that parametrize families of physically-equivalent dynamical states) from the remaining coordinates of the symmetry-reduced state space $\hat{\mathcal{M}}$. The latter capture the dynamical degrees of freedom—those associated with structural changes of the flow.

The Navier-Stokes equations are invariant under translations, rotations, and inversions about the origin, and the application of any of these symmetry operations to a state $\boldsymbol{u}(\boldsymbol{x})$ results in another dynamically equivalent state. The boundary conditions for pipe flow restrict symmetries to translations along the axial and azimuthal directions, and reflections in the azimuthal direction. In the computations presented here,axial periodicity is assumed so that the symmetry group of the system is $O(2)_\theta \times SO(2)_z$. In order to illustrate the key ideas, we constrain azimuthal shifts, and focus on the family of streamwise translational

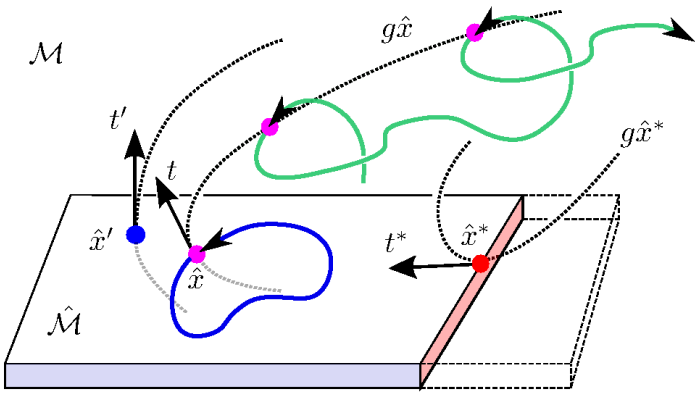

Figure 3.1: Schematic of symmetry reduction by the method of slices. The blue point is the template $\hat{x}'$. Group orbits are marked by dotted curves, so that all pink points are equivalent to $\hat{x}$ up to a shift. The relative periodic orbit (green) in the d-dimensional full state space $\mathcal{M}$ closes into a periodic orbit (blue) in the slice $\hat{\mathcal{M}} = \mathcal{M}/G$, a $(d-1)$-dimensional slab transverse to the template group tangent t'. A typical group orbit crosses the slice hyperplane transversally, with a non-orthogonal group tangent $t = t(\hat{x})$. A slice hyperplane is almost never a global slice; it is valid up to the slice border, a $(d-2)$-dimensional hypersurface (red) of points $\hat{x}^*$ whose group orbits graze the slice, i.e. points whose tangents $t^* = t(\hat{x}^*)$ lie in $\hat{\mathcal{M}}$. Beyond the slice border (dashed 'chunk'), group orbits do not cross the slice hyperplane locally.

shifts $\{g\}$ parametrized by a single continuous phase parameter ℓ,

$$(g(\ell)\,\boldsymbol{u})(z) = \boldsymbol{u}(z-\ell)\,.$$

If periodic axial symmetry is assumed, application of g gives a closed curve family of dynamically equivalent states — topologically a circle, called a *group orbit* — in state space $\mathcal{M}$. Were azimuthal ('spanwise') shifts included, equivalent states would lie on a 2-torus.

Symmetry reduction simplifies the state space by reducing each set of dynamically equivalent states to a unique point $\hat{\boldsymbol{u}}$. The *method of slices* achieves this with the aid of a fixed *template* state $\boldsymbol{u}'$ (see Fig. 3.1). A shift is applied so that the symmetry-reduced state $\hat{\boldsymbol{u}} = g(-\ell)\boldsymbol{u}$ lies within the hyperplane orthogonal to $\boldsymbol{t}' = \lim_{\ell\to 0}(g(\ell)\boldsymbol{u}' - \boldsymbol{u}')/\ell$, the tangent to the template $\boldsymbol{u}'$ in the direction of the shift. For a time-dependent flow, one

determines $\ell = \ell(t)$ by chosing $\hat{\boldsymbol{u}}$ to be the point on the group orbit of $\boldsymbol{u}$ closest to the template, $\langle \hat{\boldsymbol{u}} - \boldsymbol{u}' | \boldsymbol{t}' \rangle = 0$ in a given norm. In this work we use the L2 or 'energy' norm $E = \langle \boldsymbol{u} | \boldsymbol{u} \rangle / 2 = \int \boldsymbol{u}^2 / 2 \, dV$.

As traveling waves drift downstream without changing their spatial structure, the family of traveling wave states $\boldsymbol{u}(t)$ is dynamically equivalent (lies on the same group orbit $g(\ell)\,\boldsymbol{u}$) and may be represented by a single state $\hat{\boldsymbol{u}}_q$. Thus all traveling waves are simultaneously reduced to equilibria in the slice, irrespective of their individual phase velocities, a powerful property of the method of slices. Furthermore, all relative periodic orbits p, flow patterns each of which recurs after a different time period T_p, shifted downstream by a different ℓ_p, close into periodic orbits in the slice hyperplane.

Dynamics within the slice is given by

$$\dot{\hat{\boldsymbol{u}}} = \boldsymbol{v}(\hat{\boldsymbol{u}}) - \dot{\ell}(\hat{\boldsymbol{u}})\, \boldsymbol{t}(\hat{\boldsymbol{u}}) \,, \tag{3.1}$$

$$\dot{\ell}(\hat{\boldsymbol{u}}) = \langle \boldsymbol{v}(\hat{\boldsymbol{u}}) | \boldsymbol{t}' \rangle \,/\, \langle \boldsymbol{t}(\hat{\boldsymbol{u}}) | \boldsymbol{t}' \rangle \,, \tag{3.2}$$

where the expression for the phase velocity $\dot{\ell}$ is known as the *reconstruction equation*[51]. No dynamical information is lost and we may return to the full space by integrating Eq. 3.2. In contrast to a Poincaré section, where trajectories pierce the section hyperplane, time evolution traces out a continuous trajectory within the slice. In principle, the choice of template is arbitrary; in practice, some templates are preferable to others. While one is concerned with the dynamics within the slice $\hat{\boldsymbol{u}}(t)$, in practice it may be simpler to record $\ell(t)$ and to post-process, or to process on the side, visualizations within the slice—slicing is much cheaper to perform than gathering $\boldsymbol{u}(t)$ from simulation or laboratory experiment.

The enduring difficulty with symmetry reduction is in determining a unique shift ℓ for a given state $\boldsymbol{u}$, while avoiding discontinuities in $\ell(t)$ that arise when multiple 'best fit' candidates $\hat{\boldsymbol{u}} = g(-\ell)\boldsymbol{u}$ to the template $\boldsymbol{u}'$ occur. A singularity arises if the group orbit $g\boldsymbol{u}$ grazes the slice hyperplane (Fig. 3.1). At the instant this occurs, the tangents to the fluid

state $\hat{\boldsymbol{u}}$ and the template $\boldsymbol{u}'$ are orthogonal, and there is a division by zero in the reconstruction equation 3.2. In [52] it was shown that the hyperplanes defined by multiple templates could be used to tile a slice, but while switching may permit the symmetry reduction of longer trajectories, it is often not possible to both switch templates before a slice border is reached and to simultaneously maintain continuity in ℓ. Furthermore, it is uncertain when to switch back to the first template, in order to produce a unique symmetry-reduced state. Our aim in this article is to avoid such difficulties through the use of a single template with distant slice borders. The approach of Budanur *et al.*[49] for the case of one translational spatial dimension fixes the phase of a single Fourier coefficient. This 'Fourier' slice is a special case within the slicing framework, with the effect of extreme smoothing of the group orbit. Here the approach is extended to a spatially 3-dimensional case, that of turbulent pipe flow.

For the case of a scalar field defined on one spatial dimension[49] there is a unique Fourier coefficient appropriate for determining the symmetry reduction. Here, for the 3-dimensional turbulent flow, there are three components of velocity with a spatial discretization for each, and it is not obvious which coefficients to fix in order to define an effective symmetry-reducing slice. In this paper we construct a template $\boldsymbol{u}'(r,\theta,z) = \boldsymbol{u}_c\cos(\alpha z) + \boldsymbol{u}_s\sin(\alpha z)$, where $\boldsymbol{u}_c(r,\theta) = \int_0^L \tilde{\boldsymbol{u}}\cos(\alpha z)\,\mathrm{d}z$, $\boldsymbol{u}_s(r,\theta) = \int_0^L \tilde{\boldsymbol{u}}\sin(\alpha z)\,\mathrm{d}z$, and $L = 2\pi/\alpha$, for some chosen state $\tilde{\boldsymbol{u}}$. This corresponds to (all of) the first coefficients in the streamwise Fourier expansion for $\tilde{\boldsymbol{u}}$. Arbitrary states $\boldsymbol{u}$ may then be projected onto a plane via $a_1 = \langle \boldsymbol{u}|\boldsymbol{u}'\rangle$ and $a_2 = \langle \boldsymbol{u}\,|\,g(L/4)\,\boldsymbol{u}'\rangle$, respectively (see Fig. 3.2). In this projection, the group orbit $g\boldsymbol{u}$ of any state is a circle centered on the origin, and the polar angle θ for the point (a_1, a_2) corresponds to a unique shift $\ell = \theta(L/2\pi)$. The symmetry reduced state $\hat{\boldsymbol{u}} = g(-l)\,\boldsymbol{u}$ is the closest point on its group orbit to the template $\boldsymbol{u}'$. The slice is projected onto the positive a_1-axis in this projection.

Note that the approach is independent of discretization, and does not actually require a Fourier decomposition. Note also that the inner-product gathers information from the full

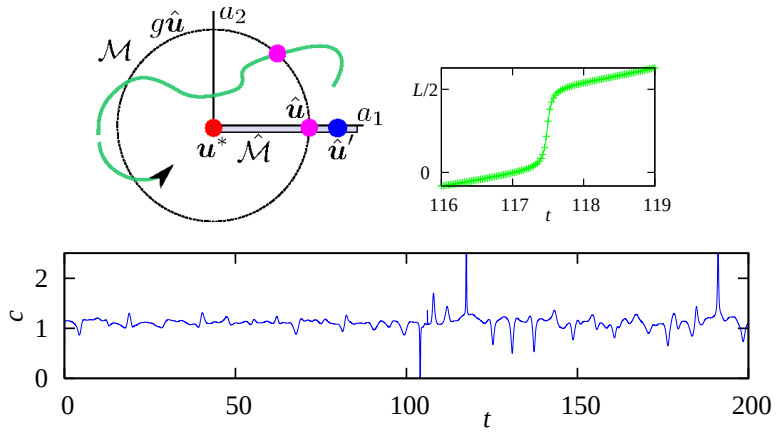

Figure 3.2: (*top left*) Schematic of the first Fourier mode slice, with a_1, a_2 defined in the text. In this projection the slice border is a zero-measure 'point' at the origin. (*bottom*) For a generic ergodic trajectory the phase velocity $c = \dot{\ell}(t)$ appears to encounter singularities whenever it approaches the slice border, which, however, is never reached[49]. Closer inspection reveals a rapid but continuous change in the shift (*top right*) by $\approx L/2$ in the $\ell(t) - \bar{c}t$ Galilean frame, moving (for our parameter values) at $\bar{c} = 1.1092$. These apparent jumps are well resolved: each '+' corresponds to 10 time integration steps.

velocity field.

As group orbits are circles crossing perpendicular to the a_1-axis in this projection, $\langle \boldsymbol{t}(\hat{\boldsymbol{u}}) | \boldsymbol{t}' \rangle$ in Eq. 3.2 can only be zero if the circle shrinks to a point at the origin. This requires that both inner products $\langle \boldsymbol{u} | \boldsymbol{u}' \rangle$ and $\langle \boldsymbol{u} \,|\, g(L/4)\, \boldsymbol{u}' \rangle$ are zero at the same time, which has vanishing probability. While we thus avoid the slice border, there is a rapid change in θ by $\approx \pi$ (in ℓ units by $\approx L/2$) whenever the trajectory $(a_1, a_2)(t)$ sweeps past the origin, see the inset to Fig. 3.2. Rapid phase shifts notwithstanding, this choice of template has made possible the discovery and analysis of the many relative periodic orbits discussed below.

'Minimal flow units'[54], which capture much of the statistical properties of turbulence, have been invaluable in analyzing fundamental self-sustaining processes[55]. Here, the fixed-flux Reynolds number for all calculations is $Re = DU/\nu = 2500$, where lengths are non-dimensionalized by diameter D and velocities are normalized by the mean axial speed U. The minimal flow unit is in the $m = 4$ rotational subspace, such that $(r, \theta, z) \in [0, \frac{1}{2}] \times [0, \frac{\pi}{2}] \times [0, \frac{\pi}{1.7}]$. The size of the domain is more usefully measured in terms of wall units, ν/u_τ, where $u_\tau^2 = -\nu \, (\partial_r u_z)|_{\text{wall}}$, which allows comparison with flow units

Table 3.1: A subset of traveling waves and relative periodic orbits of the lowest Kaplan-Yorke dimension[53], out of respectively 10 and 29 extracted so far and plotted in 3.4. Traveling waves are labeled by their dissipation rate, and relative periodic orbits are labeled by their period T. Listed are mean dissipation $\overline{D}$, mean down-stream phase velocity $\overline{c}$, the number of unstable eigen-directions (two per each complex pair), Kaplan-Yorke dimension D_{KY}, the real part of the largest stability eigenvalue/Floquet exponent $\mu^{(max)}$, and either the corresponding imaginary part $\omega^{(max)}$ for traveling waves, or the phase θ of the complex Floquet multiplier for relative periodic orbits, or its sign, if real: -1 indicates inverse hyperbolic.

	$\overline{D}$	$\overline{c}$	#	D_{KY}	$\mu^{(max)}$	ω or θ
$\mathrm{TW}_{N4L/1.38}$	1.380	1.238	3	6.97	0.1809	0
$\mathrm{TW}_{2.03}$	2.039	1.091	7	15.21	0.1159	0
$\mathrm{TW}_{1.97}$	1.968	1.104	9	20.01	0.1549	0.259
$\mathrm{TW}_{2.04}$	2.041	1.095	8	20.04	0.1608	0
$\mathrm{TW}_{N4U/3.28}$	3.279	1.051	30	73.67	0.9932	3.136
$\mathrm{RPO}_{6.66}$	1.806	1.122	3	7.99	0.0535	1.690
$\mathrm{RPO}_{27.30}$	1.815	1.127	4	8.98	0.0678	0.961
$\mathrm{RPO}_{13.19}$	1.839	1.119	5	9.68	0.0581	2.038
$\mathrm{RPO}_{20.43}$	1.809	1.130	5	11.03	0.0771	+1
$\mathrm{RPO}_{4.95}$	2.015	1.090	3	11.54	0.1509	1.643
$\mathrm{RPO}_{7.72}$	1.708	1.141	5	11.62	0.0983	+1
$\mathrm{RPO}_{15.46}$	1.781	1.027	7	12.69	0.1162	+1
$\mathrm{RPO}_{9.74}$	2.050	1.088	7	12.87	0.1873	-1
$\mathrm{RPO}_{23.36}$	1.980	1.113	6	13.37	0.1011	1.251
$\mathrm{RPO}_{7.42}$	1.838	1.111	6	13.89	0.1195	0.388
$\mathrm{RPO}_{17.46}$	1.917	1.122	6	14.67	0.0841	0.196
$\mathrm{RPO}_{14.05}$	1.902	1.109	7	14.75	0.1403	-1
ergodic	1.956	1.109				

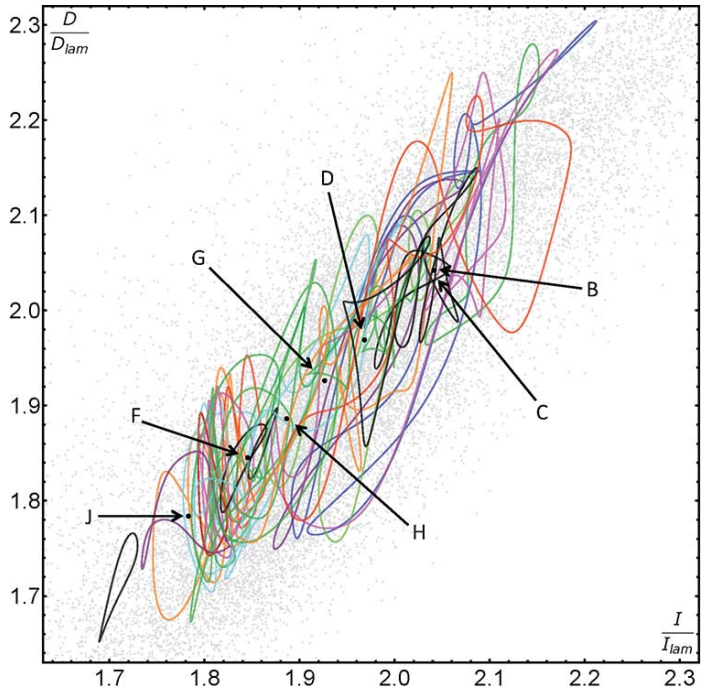

Figure 3.3: Projection of 32 relative periodic orbits and traveling waves using symmetry-invariant coordinates, I/I_{lam}, D/D_{lam} where $I_{lam} = D_{lam}$ are energy rates for the laminar flow. All discovered traveling waves are included: (B) $\mathrm{TW}_{2.04}$, (C) $\mathrm{TW}_{2.03}$, (D) $\mathrm{TW}_{1.97}$, (G) $\mathrm{TW}_{1.93}$, (H) $\mathrm{TW}_{1.89}$, (F) $\mathrm{TW}_{1.85}$ and (J) $\mathrm{TW}_{1.78}$, except for $\mathrm{TW}_{N4L/1.38}$, $\mathrm{TW}_{N4U/3.28}$ and $\mathrm{TW}_{1.57}$, which lie far outside the ergodic cloud (grey dots).

used in other geometries. In these units, the domain is of size $\Omega^+ \approx [100, 160, 370]$ in the wall-normal, spanwise and streamwise dimensions, respectively. Our flow unit compares favorably with the minimal flow units for channel flow[54] $\Omega^+ \approx [> 40, 100, 250 - 350]$ and Couette flow[55] $\Omega^+ \approx [68, 128, 190]$. Recurrent flows have been identified in [47] for a box of size $\Omega^+ \approx [68, 86, 190]$. Our domain is sufficiently large to reproduce $Re_\tau = (D/2)u_\tau/\nu = 100 \pm 1$ to within 10% of its value in the infinite domain. The mean wall friction for turbulent flow is approximately 100% greater than that for laminar flow at this flow rate.

A Newton-Krylov scheme is used to search for relative periodic orbits. Initial guesses are taken from near recurrences of ergodic trajectories[47] within the symmetry-reduced state space. This preferentially identifies structures embedded in regions of high natural measure (regions most frequented by ergodic trajectories), with isolated traveling waves

and relative periodic orbits that sit in the less frequented reaches of state space less likely to be found. Our searches have so far identified 10 traveling waves and 32 relative periodic orbits. An abbreviated summary of data is given in Table 3.1; the complete data set is available online at `Openpipeflow.org`, along with the open source code used to calculate these orbits.

Visualizations of high-dimensional state space trajectories are necessarily projections onto two or three dimensions. A common choice is to monitor the flow in terms of the rate of energy dissipation $D = \rho\nu \int \boldsymbol{u} \cdot \nabla^2 \boldsymbol{u}\, dV$ and the external input power required to maintain constant flux $I = Q\,\Delta p$, where $Q = \int \boldsymbol{u} \cdot \boldsymbol{dS}$ is the flux at any cross-section and Δp and is the pressure drop over the length of the pipe. As the time-averages of I and D are necessarily equal, traveling waves and orbits, which may be well-separated in state space, are contracted onto or near the $I = D$ line, a drawback of the 2-dimensional (I, D) projection. Fig. 3.3 shows that the orbits appear to overlap with the ergodic region, but reveals little of the relationships between solutions; we use D values only to distinguish traveling waves solutions listed in Table 3.1.

In the symmetry-reduced state space it is possible to construct coordinates that are intrinsic to the flow itself, using spatial information that would otherwise be smeared out by translational shifts. To obtain a global portrait of the turbulent set, 3.4, we project solutions onto the three largest principal components $\hat{\boldsymbol{e}}_i$ obtained from a PCA of N=2000 independent $\hat{\boldsymbol{u}}'_i = \hat{\boldsymbol{u}}_i - \bar{\hat{\boldsymbol{u}}}$, where $\bar{\hat{\boldsymbol{u}}}$ is the mean of the data, using the SVD method (on average the square of the projection $p_i = \langle \hat{\boldsymbol{u}}'(t) | \hat{\boldsymbol{e}}_i \rangle$ equals the i^{th} singular value of the correlation matrix $R_{ij} = \frac{1}{N-1} \langle \hat{\boldsymbol{u}}'_i | \hat{\boldsymbol{u}}'_j \rangle$).

The lower / upper branch pair $\mathrm{TW}_{N4L/1.38}$ / $\mathrm{TW}_{N4U/3.28}$ were obtained by continuation from a smaller 'minimal flow unit'[52]. In Table 3.1 and in the (I, D)-projection Fig. 3.3 the upper branch traveling wave $\mathrm{TW}_{N4U/3.28}$ appears to be far removed from turbulence, unlikely to exert influence. The PCA projection of the symmetry-reduced state space, however, reveals the strong repelling influence of $\mathrm{TW}_{N4U/3.28}$ whose 30-dimensional unstable

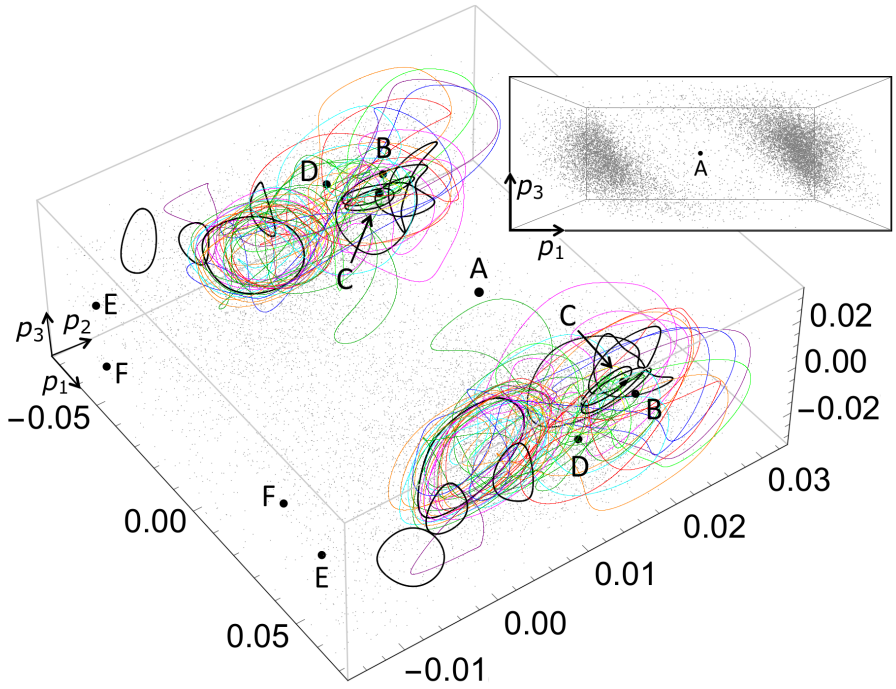

Figure 3.4: Projection of the symmetry-reduced infinite-dimensional state space onto the first 3 PCA principal axes, computed from the L2-norm average over the natural measure (the gray 'cloud') in the slice. 32 relative periodic orbits, and a subset of the 7 shortest relative periodic orbits, together with traveling waves (A) $\mathrm{TW}_{N4U/3.28}$, (B) $\mathrm{TW}_{2.04}$, (C) $\mathrm{TW}_{2.03}$, (D) $\mathrm{TW}_{1.97}$, (E) $\mathrm{TW}_{1.98}$, (F) $\mathrm{TW}_{1.85}$. While $\mathrm{TW}_{1.93}$ appears to lie in the very center of the (I, D) projection 3.3, it is revealed in this state space projection to lie far from the ergodic cloud, outside the box plotted, as are (E) $\mathrm{TW}_{N4L/1.38}$ and (F) $\mathrm{TW}_{1.85}$. Due to a 'rotate-and-reflect' symmetry, each solution appears twice, with the exception of (A) $\mathrm{TW}_{N4U/3.28}$ (and the far-away $\mathrm{TW}_{N4L/1.38}$), which belong to the 'rotate-and-reflect' invariant subspace. Our relative periodic orbits capture the regions of high natural measure very well. The symmetry-invariant subspace has a strong repulsive influence, separating the natural measure into two weakly communicating regions. The inset shows the ergodic cloud from another perspective.

manifold acts as a barrier to the dynamics, cleaving the natural measure into two 'clouds', forcing a trajectory to hover around one neighborhood until it finds a path to the other, bypassing $\mathrm{TW}_{N4U/3.28}$. The two ergodic 'clouds' are related by the 'rotate-and-reflect' symmetry ($\pi/4$ rotation), under which $\mathrm{TW}_{N4U/3.28}$ is invariant (for symmetries of pipe flow see [52]).

The symmetry-reduced state space projections reveal sets of relative periodic orbits with qualitatively similar dynamics. The short-period orbits are well spread over the dense regions of natural measure, and the long relative periodic orbits in (a) appear to 'shadow' short orbits in (b), but also exhibit extended excursions that fill out state space. While sets of relative periodic orbits often share comparable dissipation rates and Floquet exponents (Table 3.1 and `Openpipeflow.org` data sets), it is the state space projections that are essential to establishing genuine relationships.

3.4 Conclusions

In summary, we have shown that symmetry reduction can be applied to a dynamical system of very high dimensions, here turbulent pipe flow. An appropriately constructed template renders the method of slices substantially more effective for projecting the dynamics and for Newton searches for invariant solutions. The method is general and can be applied to any dynamical system with continuous translational or rotational symmetry. Projections of the symmetry-reduced space reveal fundamental properties of the dynamics not evident prior to symmetry reduction. In the application at hand, to a turbulent pipe flow, the method has enabled us to identify for the first time a large set of relative periodic orbits embedded in turbulence, and to demonstrate that the key invariant solutions strongly influence turbulent dynamics. To follow this demonstration of the power of symmetry reduction, work is now underway to determine the relationship between relative periodic orbits[37]. Analysis of their unstable manifolds are expected to reveal the intimate links between traveling waves and relative periodic orbits, allowing for explicit construction of the invariant skeleton that

gives shape to the strange attractor explored by turbulence.

CHAPTER 4
RELATIVE PERIODIC ORBITS FORM THE BACKBONE OF TURBULENT PIPE FLOW.

4.1 Abstract

Chaotic dynamics of low-dimensional systems, such as Lorenz or Rössler flows, is guided by the infinity of periodic orbits embedded in their strange attractors. Whether this also be the case for the infinite-dimensional dynamics of Navier–Stokes equations has long been speculated, and is a topic of ongoing study. Periodic and relative periodic solutions have been shown to be involved in transitions to turbulence. Their relevance to turbulent dynamics—specifically, whether periodic orbits play the same role in high-dimensional nonlinear systems like the Navier–Stokes equations as they do in lower-dimensional systems—is the focus of the present investigation. We perform here a detailed study of pipe flow relative periodic orbits with energies and mean dissipations close to turbulent values. We outline several approaches to reduction of the translational symmetry of the system. We study pipe flow in a minimal computational cell at $Re = 2500$, and report a library of invariant solutions found with the aid of the method of slices. Detailed study of the unstable manifolds of a sample of these solutions is consistent with the picture that relative periodic orbits are embedded in the chaotic saddle and that they guide the turbulent dynamics.

4.2 Introduction

Revealing the underlying mechanisms of fluid turbulence is a multidisciplinary endeavour that brings together pure and applied mathematics, high performance computation, and experimental physics. Over the past two decades, this effort has led to significant progress in our understanding of transitionally turbulent fluid flows in physically motivated geome-

tries, such as a circular pipe. Today we have numerical evidence that the laminar state of the pipe flow [56, 57] is linearly stable for all cases that can be observed in laboratory experiments, i.e., for Reynolds numbers up to $Re = 10^7$ [17]. In addition, both numerical and laboratory experiments [58, 59] indicate that turbulence of finite spatial extent, either in the form of a localised patch or turbulence or within a geometry of finite volume, has a finite lifetime at transitional *Re* values. (When the spatial expansion of turbulence in larger domains defeats relaminarisations, such that it persists indefinitely, the system becomes a strange attractor [60].) These observations suggest, from the dynamical systems point of view, that the study of a turbulent pipe flow is the study of a chaotic saddle, i.e., a strange repeller in the infinite-dimensional state space of the solutions to Navier–Stokes equations. For low-dimensional dynamics, it is known that strange sets are shaped by the 'invariant solutions' and their stable and unstable manifolds. [1]

This intuition motivated several groups [52, 61, 62, 63] to investigate invariant solutions of Navier–Stokes equations in a circular pipe; these studies, in turn, were followed by experimental observations [40, 41] of relatively close visits of the turbulent trajectories to some of the numerical traveling wave solutions. With a fast-growing catalogue of exact invariant solutions of the Navier–Stokes equations in hand, acquired by our group and others [36, 64], we are nearing the point where focus turns from finding invariant solutions to constructing their stable and unstable manifolds, the building blocks of a chaotic saddle.

Most of the early studies of invariant solutions in pipe flow had focused on structures that play role in transition to turbulence. Typically these solutions emerged in saddle-node bifurcations (or further bifurcations of such solutions) as lower/upper-branch pairs. Lower-branch solutions appeared to belong to state space regions that separated initial conditions into those that uneventfully relaminarize, and those that develop into turbulence. Moreover, these solutions are characterized by structures smoother than those observed in turbulence,

[1] Here by 'invariant solutions' or 'exact coherent structures' we mean compact, time-invariant solutions that are set-wise invariant under the time evolution and the continuous symmetries of the dynamics. Invariant solutions include, for instance, equilibria, traveling waves, periodic orbits and invariant tori. Note in particular that the closure of a relative periodic orbit is an invariant torus.

hence their numerical study was relatively simple and required moderate numbers of computational degrees of freedom. Upper-branch solutions, on the other hand, undergo very complex sequences of bifurcations [65] upon increasing *Re*, giving rise to complicated dynamics with many of the resulting solutions distant from the turbulent regions. While these bifurcations are precursors of turbulence in pipe flow, a complete continuation from upper-branch solutions to turbulence is a very hard task: Many solutions undergo sequences of bifurcations in different regions of the state space, then sometimes merge through boundary crises that are hard to detect.

By contrast, the strategy of the present study is to extract invariant solutions from close recurrences of turbulent flow simulations [66], for a given *Re* and domain geometry, with the aim of identifying dynamically relevant structures, without any prior knowledge of the bifurcation sequences from which they might have originated.

Pipe flow is driven by a pressure gradient; hence, all of its finite-amplitude solutions drift downstream. The simplest invariant solutions in such translationally-invariant systems are traveling waves. Due to the azimuthal-rotation invariance of the pipe flow, in general one anticipates finding traveling waves that simultaneously drift downstream and rotate about the axis of the pipe (rotational waves). Since the motions of such solutions can be eliminated by a change to the co-moving frame, moving along the system's symmetry directions, the physical observables associated with them, such as wall friction or dissipation, do not change in time. In other words, the dynamical information contained in these solutions is rather limited. The simplest time-dependent invariant solutions that capture dynamics in terms of time-dependent, but symmetry-invariant, observables are the relative periodic orbits, which are velocity field profiles that exactly recur at a streamwise (downstream) shifted location after a finite time. More generally, relative periodic orbits may have azimuthal rotations in addition to the streamwise drifts, however, such orbits are not contained in the symmetry-subspace we study here.

In this work, we present the 48 relative periodic orbits and 10 traveling waves, adding

19 new solutions to the 29 solutions reported in [36]. Six of these new relative periodic orbits are computed by the method of multi-point shooting (for the first time in the pipe flow context) whereby the initial guesses for longer orbits are constructed from known shorter orbits that shadow them (see Appendix § B).

Next, we investigate the role the invariant solutions play in shaping the turbulent dynamics. To this end we carry out global and local state space visualizations, both in the symmetry-reduced state space, and in its Poincaré sections. For global visualizations, we take a data-driven approach and project relative periodic orbits and turbulent dynamics onto 'principal components' obtained from the symmetry-reduced turbulence data. We show that this approach has only limited descriptive power for explaining the organization of solutions in the state space. We then move onto examining the unstable manifold of our shortest relative periodic orbit and illustrate how it shapes the nearby solutions. This computation extends [67]'s method for studying the unstable manifolds of 'edge state' relative periodic orbits to the solutions that are embedded in turbulence, with unstable manifold dimensions greater than one. Finally, we demonstrate that when a turbulent trajectory visits the neighbourhood of this relative periodic orbit, it shadows it for a finite time interval.

Our results demonstrate the necessity of symmetry reduction for state space analysis. We reduce the continuous translational symmetry along the pipe by bringing all states to a symmetry-reduced state space (the slice), and contrast this with the 'method of connections'. The remaining discrete azimuthal symmetry is reduced by defining a *fundamental domain* within the slice, where each state has a unique representation. We demonstrate, on concrete examples, that this symmetry reduction makes possible a dynamical analysis of the pipe flow's state space.

The paper is organized as follows. In § 4.3 we describe the pipe flow and its symmetries. In § 4.4 we discuss the method of slices used to reduce the continuous symmetry. The computed invariant solutions are listed and discussed in § 4.5. In § 4.6 we investigate the dynamical role of the invariant solutions using global and local state space visualisations.

§ 4.7 contains our concluding remarks.

4.3 Pipe flow

The flow of an incompressible viscous fluid through a pipe of circular cross-section is considered. Fluid in a long pipe carries large momentum, which in turn smooths out fluctuations in the mass flux on short time-scales. We therefore consider flow with constant mass flux whose governing equations read

$$\frac{\partial \boldsymbol{u}}{\partial t} + \boldsymbol{U}\cdot\boldsymbol{\nabla}\boldsymbol{u} + \boldsymbol{u}\cdot\boldsymbol{\nabla}\boldsymbol{U} + \boldsymbol{u}\cdot\boldsymbol{\nabla}\boldsymbol{u} = -\boldsymbol{\nabla}p + 32\frac{\beta}{\boldsymbol{Re}}\hat{\mathbf{z}} + \frac{1}{\boldsymbol{Re}}\boldsymbol{\nabla}^2\boldsymbol{u}\,, \quad \boldsymbol{\nabla}\cdot\boldsymbol{u} = 0 \quad (4.1)$$

The equations are formulated in cylindrical-polar coordinates (r, θ, z) denoting the radial coordinate r, the azimuthal angle θ and the stream-wise (or axial) coordinate z along the pipe. The Reynolds number is defined as $\boldsymbol{Re} = UD/\nu$, where U is the mean velocity of the flow, D is the pipe diameter, and ν is the kinematic viscosity. The governing equation Eq. 4.1 is non-dimensionalized by scaling the lengths by D, the velocities by U, and time by D/U. The velocity $\boldsymbol{u}$= (u, v, w) denotes the deviation from the dimensionless laminar Hagen–Poiseuille flow equilibrium $\boldsymbol{U}(r) = 2\,(1-(2r)^2)\,\hat{\boldsymbol{z}}$. In addition to the pressure gradient required to maintain laminar flow, the excess pressure required to maintain constant mass flux is measured by the feedback variable $\beta = \beta(\boldsymbol{u})$ — the total dimensionless pressure gradient is $(1+\beta)(32/Re)$ and $\beta = 0$ for laminar flow. The Reynolds number used throughout this work is $Re = 2500$.

Our computational cell is in the $m_0 = 4$ rotational subspace, $\Omega : (r, \theta, z) \in [0, \frac{1}{2}] \times [0, \frac{\pi}{2}] \times [0, \frac{\pi}{\alpha}]$ with $\alpha = 1.7$, or in wall units for the wall-normal, spanwise and streamwise dimensions respectively, $\Omega^+ \approx [100, 160, 370]$. The variables in Eq. 4.1 are discritised on N non-uniformly spaced points in radius, with higher resolution near the wall, and with Fourier modes with index $|m| < M$ and $|k| < K$ in θ and z respectively. Our resolution is $(N, M, K) = (64, 12, 18)$, so that following the $\frac{3}{2}$-rule, variables are evaluated

on $64 \times 36 \times 54$ grid points, $(\Delta\theta\, D/2)^+ \approx 5$ and $\Delta z^+ \approx 7$. Whilst this domain is small, it is sufficiently large to reproduce the wall friction observed for the infinite domain to within 10%, and already sufficiently large to exhibit a complex array of periodic orbits (see [36] for details.)

4.3.1 Symmetries of the pipe flow

Here we briefly review the symmetries of the problem, and then focus on the properties of the *shift-and-reflect* flow-invariant subspace, to which we restrict the study that we present in this article. For a detailed discussion of flow-invariant subspaces of the pipe flow see, for example, the Appendix of [52]. It will be seen presently that the *shift-and-reflect* symmetry leads to two dynamically equivalent regions of state space, later observed in simulations.

In pipe flow the cylindrical wall restricts the rotation symmetry to rotation about the z-axis, and translations along it. Let $g(\phi, \ell)$ be the shift operator such that $g(\phi, 0)$ denotes an azimuthal rotation by ϕ about the pipe axis, and $g(0, \ell)$ denotes the stream-wise translation by ℓ; let σ denote reflection about the $\theta = 0$ azimuthal angle:

$$\begin{aligned} g(\phi, \ell)\, [u, v, w, p](r, \theta, z) &= [u, v, w, p](r, \theta - \phi, z - \ell) \\ \sigma\, [u, v, w, p](r, \theta, z) &= [u, -v, w, p](r, -\theta, z) \end{aligned} \tag{4.2}$$

The symmetry group of stream-wise periodic pipe flow is $\mathrm{SO}(2)_z \times \mathrm{O}(2)_\theta$; in this paper we restrict our investigations to dynamics restricted to the 'shift-and-reflect' symmetry subspace

$$S = \{e, \sigma g_z\} \tag{4.3}$$

where g_z denotes a streamwise shift by $L/2$, i.e., flow fields (Eq. 4.2) that satisfy

$$[u, v, w, p](r, \theta, z) = [u, -v, w, p](r, -\theta, z - L/2) \tag{4.4}$$

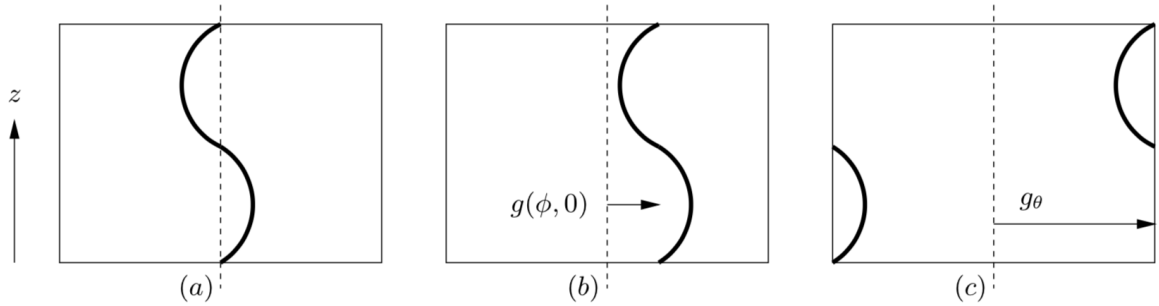

Figure 4.1: (a) Sketch of a shift-and-reflect symmetric state in the doubly-periodic domain $(\theta, z) \in [-/m_0, /m_0] \times [0, L]$ (same after shift by $L/2$ in z followed by reflection across the dotted line $\theta = 0$). (b) In general, if the state in (a) is rotated by an angle ϕ, then the shift-and-reflect symmetry is broken. (c) However, the state in (a) rotated by the half-shift $\phi = /m_0$ remains in the shift-and-reflect subspace.

This requirement couples the stream-wise translations with the azimuthal reflection. It is worth emphasising that by imposing the symmetry S, continuous rotations in θ are prohibited. Hence we consider only the simplest example of a continuous group for the streamwise translations, i.e. the one-parameter rotation group $\mathrm{SO}(2)_z$, omitting the subscript z whenever that leads to no confusion. In the azimuthal direction only a discrete rotation by half the spanwise periodicity is allowed, i.e. by π/m_0. We illustrate this property in Eq. 4.1. Thus, the symmetry group G of the pipe flow in the shift-and-reflect subspace is

$$G = \{g_\theta,\, g_z(l)\}\,, \tag{4.5}$$

where g_θ denotes the discrete azimuthal shift by π/m_0 and $g_z(l) = g(0, l)$.

Solutions that can be mapped to each other by symmetry operations Eq. 4.5 are equivalent, i.e. their physical properties, such as instantaneous energy dissipation rates, are same. Since the streamwise shift symmetry $g_z(l)$ is continuous, one may have "relative" invariant solutions in the state space of the pipe flow. Such invariant solutions that we present in this paper are: (i) Traveling waves

$$\boldsymbol{u}_{\mathrm{TW}}(t) = g_z(c_{\mathrm{TW}}\, t)\boldsymbol{u}_{\mathrm{TW}}(0)\,, \tag{4.6}$$

whose sole dynamics is a fixed velocity profile drifting along the axial direction with constant phase speed c_{TW}; and (ii) Relative periodic orbits

$$\boldsymbol{u}_{\mathrm{RPO}}(T_{\mathrm{RPO}}) = g_z(l_{\mathrm{RPO}})\, \boldsymbol{u}_{\mathrm{RPO}}(0)\,, \tag{4.7}$$

which are time-varying velocity profiles which exactly repeat after period T_{RPO}, but shifted stream-wise by l_{RPO}. In principle, one also has relative periodic orbits which are also relative with respect to azimuthal half rotations, such that

$$\boldsymbol{u}_{\mathrm{RPO}}(T_{\mathrm{RPO}}) = g_\theta\, g_z(l_{\mathrm{RPO}})\, \boldsymbol{u}_{\mathrm{RPO}}(0)\,. \tag{4.8}$$

These orbits connect two chaotic saddles related by g_θ. As we shall illustrate in the global visualisations of dynamics in § 4.5, such transitions between the two saddles are quite rare. Therefore, we did not search for relative periodic orbits of 4.8 kind, and focused instead on one of the chaotic saddles related by azimuthal half-rotation.

4.3.2 State-space notation

Let x denote the state space vector which uniquely represents a three-dimensional velocity field $\boldsymbol{u}$ over the given computational domain. While the state space representation x is technically infinite-dimensional, due to numerical discretization of the velocity field (spatial discretization, truncated Fourier expansions, etc.) in practice x is a high- but always finite-dimensional vector.

We denote the semi-flow induced by the time evolution of the Navier–Stokes equations Eq. 4.1 by f^t, so that

$$x(t) = f^t(x(0)) \tag{4.9}$$

traces out a trajectory $x(t)$ in the state space. For an infinitesimal time δt, we can expand

Eq. 4.9 as $x(t+\delta t) = a(t) + v(x(t))\delta t + \mathcal{O}(|\delta t|^2)$, where we refer to

$$\dot{x} = v(x) \tag{4.10}$$

as the *state-space velocity*.

The ordinary differential equation (ODE) Eq. 4.10 has the same symmetry group Eq. 4.5 as the Navier–Stokes equations it approximates, i.e., the state-space velocity $v(x)$ and the flow $f^t(x)$ commute with the symmetry group actions, $gv(x) = v(gx)$ and $gf^t(x) = f^t(gx)$.

4.4 Symmetry reduction by method of slices

In this paper we investigate the geometry of turbulent attractor in terms of shapes and unstable manifolds of a large number of invariant solutions that form its backbone, and for that task a symmetry reduction scheme is absolutely essential. We recapitulate here briefly the construction of a symmetry-reduced state space, or 'slice'. For further detail and historical notes the reader is referred to [68].

The set of points generated by action of all shifts $g(\ell)$ on the state space point x,

$$\mathcal{M}_x = \{g(\ell)\, x |\, \ell \in [0, L)\} \tag{4.11}$$

is known as the *group orbit* of x. All states in a group orbit are physically equivalent, and one would like to construct a 'symmetry-reduced state space' where the whole orbit is represented by a single point $\hat{x}$. The *method of slices* accomplishes this in open neighbourhoods (never globally), by fixing the shift ℓ with reference to a 'template', a state space point denoted $\hat{x}'$. A point on the group orbit with a minimal distance from the template satisfies

$$0 \;=\; \frac{\partial}{\partial \ell}\, ||g(-\ell)\, x - \hat{x}'||^2 \;=\; \frac{\partial}{\partial \ell}\, ||x - g(\ell)\, \hat{x}'||^2 \;=\; 2\, \langle x - g(\ell)\, \hat{x}' | - \frac{\partial}{\partial \ell} g(\ell)\, \hat{x}' \rangle \tag{4.12}$$

for a given ℓ. Here, $\langle\cdot|\cdot\rangle$ denotes an inner product and $\|\cdot\|$ denotes the corresponding norm (see 4.6.1 for several specific choices of such inner products). Let $\boldsymbol{t}'$ be the tangent to the group orbit of $\hat{x}'$, i.e., $\boldsymbol{t}' = \lim_{\delta\ell\to 0}(g(\delta\ell)\,\hat{x}' - \hat{x}')/\delta\ell$. Given that $\langle\hat{x}'|\hat{x}'\rangle$ is a constant,

$$0 = \frac{\partial}{\partial\ell}\langle\hat{x}'|\hat{x}'\rangle = 2\,\langle\hat{x}'|\frac{\partial}{\partial\ell}\hat{x}'\rangle = 2\,\langle\hat{x}'|\boldsymbol{t}'\rangle \tag{4.13}$$

Using also that $g(\ell)$ and $\partial/\partial\ell$ commute, then from Eq. 4.12 the minimum distance between the group orbit of x and the template $\hat{x}'$ occurs for a shift ℓ that satisfies the *slice condition*,

$$0 \;=\; \langle x - g(\ell)\,\hat{x}'|g(\ell)\,\boldsymbol{t}'\rangle \;=\; \langle g(-\ell)\,x - \hat{x}'|\boldsymbol{t}'\rangle \;=\; \langle g(-\ell)\,x|\boldsymbol{t}'\rangle \tag{4.14}$$

We denote by $\hat{x} \;=\; g(-\ell)\,x$ the in-slice representative for the whole group orbit of the full state space state x. The in-slice trajectory $\hat{x}(t)$ can be generated by integrating the dynamics confined to the symmetry-reduced state space, or 'slice',

$$\hat{v}(\hat{x}) \;=\; v(\hat{x}) - \dot{\ell}(\hat{x})\,\boldsymbol{t}(\hat{x})\,, \tag{4.15}$$

$$\dot{\ell}(\hat{x}) \;=\; \langle v(\hat{x})|\boldsymbol{t}'\rangle \,/\, \langle\boldsymbol{t}(\hat{x})|\boldsymbol{t}'\rangle \tag{4.16}$$

The first of these two equations expresses how the symmetry-reduced state-space velocity differs from the full state-space velocity by a small shift along the group orbit, parallel to the tangent, at each instant in time. Taking the inner product with $\boldsymbol{t}'$ leads to the second equation for $\dot{\ell}(t)$. In a time-stepping scheme one has a good estimate for $\ell(t)$ from its previous time step value, so it is more practical to use the slice condition Eq. 4.14 rather than Eq. 4.15 to determine ℓ. The latter condition, however, known as the *reconstruction equation*, is useful in illustrating the behaviour of the phase speed $\dot{\ell}$ (for an example, see Fig. 4.2 (*a*)). When the symmetry-reduced state $\hat{x}$ and the template $\hat{x}'$ are not too distant, their group tangents are partially aligned, and the divisor in Fig. 4.15 is positive. If the tangents become orthogonal, a division by zero occurs, and the phase speed diverges. This

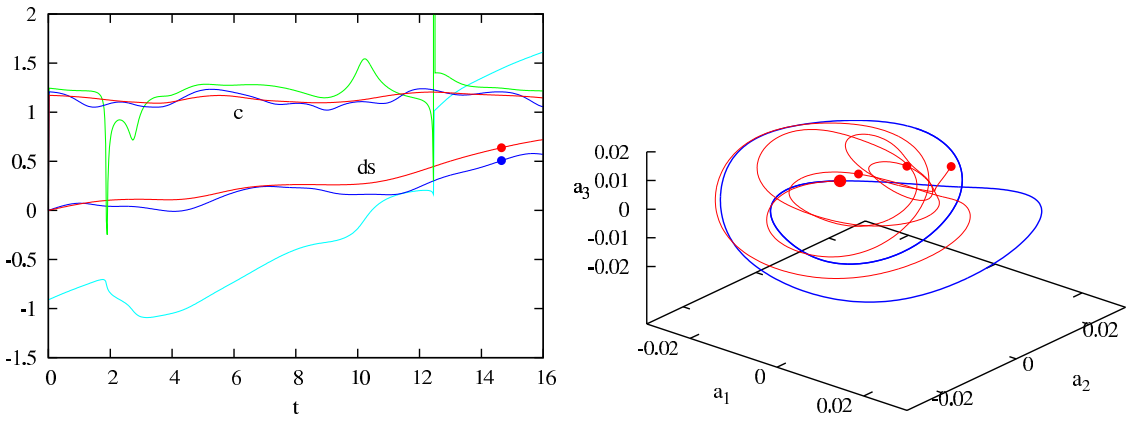

Figure 4.2: Visualisations of the relative periodic orbit $\text{RPO}_{M/14.646}$. (*a*) Phase speed $c = \dot{\ell}$ and deviation in shift $ds = \ell - \bar{c}t$ from a Galilean frame moving with mean phase speed $\bar{c} = 1.11$: (green/cyan) $\hat{x}' \equiv TW_{1.85}$, (blue) template $\hat{x}'$ on $\text{RPO}_{M/14.646}$, taken to be the state for which the wall friction is lowest, (red) method of connections. (*b*) Three $\text{RPO}_{M/14.646}$ periods, starting from the large red dot, (blue) sliced with the template $\hat{x}'$, and (red) method of connections, with times T, $2T$, $3T$ marked by the small red dot. The projection on $x_i = \langle \hat{x} | e_i \rangle$, where the e_i are unit vectors (see main text).

defines the *slice border*.

Figure 4.2 (*a*) shows the method of slices applied to the relative periodic orbit $\text{RPO}_{M/14.646}$ (see table 4.1). For purposes of illustrating that the slice hyperplane defined by Eq. 4.14 is good only in an open neighborhood, we take first a point on the somewhat distant traveling wave $\text{TW}_{1.845}$ as a trial template $\hat{x}'$. At time $t = 2$, $\hat{x}(t)$ approaches the slice border, with a rapid change in $\ell(t)$ and large $c = \dot{\ell}$. Near time $t = 12$ the orbit hits the border, and there is a discontinuity in ℓ.

A nearer template point would be a better choice. Indeed, as illustrated by Fig. 4.2 (*b*), we find that the point of the lowest wall friction on the orbit itself works very well as a template state $\hat{x}'$: the slice now captures the entire $\text{RPO}_{M/14.646}$ without encountering any slice border and any discontinuity (blue).

4.4.1 Method of connections

If one were to use the state itself as a template at each instant in time, then a division by zero would always be avoided. This corresponds to projecting out the component parallel to the shift, i.e., the group orbit tangent, at each moment in time. In [51] this is referred to as the *method of connections*. While very appealing and sometimes deployed [69] to 'calm' a turbulent flow, the method of connections is *not* a symmetry reduction method, in the sense that the dimensionality of the state space is not reduced by 1 for each continuous symmetry parameter (see, e.g., [70, 71]). This is illustrated by Fig. 4.2. Starting with the same initial condition (fat red point), with the method of slices the orbit $\hat{x}(0) = \hat{x}(T)$ closes after one period $T = 14.646$ (blue), while with the method of connections the orbit continues filling out the relative periodic orbit torus ergodically, never closing into a periodic orbit. Fig. 4.2 (*b*) shows a projection of the trajectory generated by the two approaches, for three cycles of the periodic orbit. Whereas the orbit closes for the method of slices, for the method of connections the invariant torus remains a torus. In conclusion, nothing is gained by using the method of connections.

The orthogonal unit vectors used in Fig. 4.2(*b*) are the leading components from a principal component analysis (PCA), using 586 symmetry-reduced states equi-spaced in time around the orbit. Further details are given in § 4.6.

4.4.2 First Fourier mode slice

The method of slices is local, and the slice border discontinuity is avoided only within a neighbourhood of the template. In our previous work [52], a switching approach was applied to help ensure closeness to the template. Whilst this enabled symmetry reduction of longer trajectories, it proved difficult to switch before reaching a border whilst simultaneously ensuring continuity of $\ell(t)$.

A different approach was taken by [49] for one-dimensional PDEs with SO(2) symmetry, where it was shown that the first term in the Fourier expansion of the flow field

can be used as the template for a *global* slice, border of which is never visited by generic ergodic trajectories. This method relied on the observation that projections of group orbits on the subspace spanned by the first Fourier mode components (sine and cosine) are non-overlapping circles; hence one can find a unique polar angle in this projection to quotient the SO(2) symmetry. For a scalar field $u(x,t) = u(x+L,t)$ in one periodic space dimension, a slice template of the form $u' = a\cos(2\pi x/L) + b\cos(2\pi x/L)$, where a and b are constants, defines a first Fourier mode slice. In higher dimensions, one has more freedom in choosing first Fourier mode slice templates. For pipe flow, any $\hat{x}'$ corresponding to a velocity field of the form

$$\boldsymbol{u}'(r,\theta,z) = \boldsymbol{u}_c(r,\theta)\cos(\alpha z) + \boldsymbol{u}_s(r,\theta)\sin(\alpha z) \tag{4.17}$$

where $\boldsymbol{u}_{c,s}$ are three-dimensional vector fields that depend only on r and θ, can be a candidate for a first Fourier mode slice template. The vector fields $\boldsymbol{u}_{c,s}$ should be chosen such that the slice border condition $\langle x|\hat{x}'\rangle + \mathrm{i}\langle x|g_z(L/4)\hat{x}'\rangle = 0$ is avoided by generic flow fields $\boldsymbol{u} = \boldsymbol{u}(r,\theta,z,t)$.

All slices are local, but since $\langle g(-\ell)\,x|\boldsymbol{t}'\rangle = \langle x|g(\ell)\,\boldsymbol{t}'\rangle$, one way to construct slice hyperplanes with larger domains of validity is by picking templates with smoother group orbits. Smoother states (i.e., states dominated by low Fourier modes) tend to be associated with lower dissipation or wall friction. Guided by this intuition, we construct the first Fourier mode slice template Eq. 4.17 by taking a low-dissipation solution from the turbulent set and setting all of its components to 0 other than the ones with axial Fourier modes $k = 1$ [36]. For the calculation in Fig. 4.2, such a template was capable of capturing the whole orbit.

The slice-fixing shift $\ell(t)$ for a trajectory $x(t)$ is computed from the polar angle in the plane spanned by $(\hat{x}', g_z(L/4)\hat{x}')$ as

$$\ell(t) = \frac{L}{2\pi}\,\mathrm{Arg}\left[\langle x(t)|\hat{x}'\rangle + \mathrm{i}\langle x(t)|g_z(L/4)\hat{x}'\rangle\right], \tag{4.18}$$

where Arg denotes the argument of the complex number. One can then find the translation symmetry-reduced trajectory $\hat{x}(t)$ by shifting the full state space trajectory $x(t)$ back to slice by $\hat{x}(t) = g_z(-\ell(t))x(t)$.

4.5 Invariant solutions

By carrying out an extensive search for traveling waves Eq. 4.6 and relative periodic orbits Eq. 4.7, we have found 8 traveling waves and 48 relative periodic orbits of the pipe flow, listed in table 4.1. The traveling waves are labelled by their mean dissipation $\bar{D}$ (in units of the kinetic energy E_0 of the laminar solution), and relative periodic orbits by their periods T (in units of D/U). The numerical method for finding most of these invariant solutions is the Newton–GMRES–hook iteration, discussed in detail in [72] and [73]. Relative periodic orbits with long periods tend to be more difficult (or impossible) to find with the standard Newton–GMRES–hook iteration. In order to capture such long orbits, we implemented a multiple-shooting Newton method, outlined in Appendix B, and found 5 relative periodic orbits, marked with subscript 'M' in table 4.1. The highly symmetric $N4$ type traveling wave of [74] belongs to an invariant subspace with an additional shift-and-rotate symmetry,

$$[u, v, w, p](r, \theta, z) = [u, -v, w, p](r, \theta - \pi/m_0, z - L/2) \,. \tag{4.19}$$

The traveling waves $N4$ appear as a lower/upper branch pair and are therefore labeled as $N4L$ (lower branch) and $N4U$ (upper branch). The terminology refers to the appearance of these solutions from a saddle node bifurcation at a lower *Re* number as a pair of solutions with low ($N4L$) and high ($N4U$) dissipation rates. The lower branch solution is believed to belong to the laminar-turbulent boundary [74].

The traveling waves linear stability exponents $\lambda_j = \mu_j + i\omega_j$ are computed by linearizing the governing equations in the co-moving frame, in which a traveling wave becomes an equilibrium. The leading stability exponent, i.e., the exponent with the largest real part,

is reported in table 4.1. The integer d_U denotes the number of exponents with positive real parts, $\mu_j > 0$, which determine the dimension of the unstable manifold of the traveling wave.

The linear stability of a relative periodic orbit is described by its Floquet multipliers $\Lambda_j = \exp(\mu_j T + i\theta_j)$. As for the traveling waves, in table 4.1 we report the number of the unstable directions d_U, real part μ^{max} of the leading Floquet exponent $\lambda_j = (1/T)\ln|\Lambda_j|$, and the phase θ of the leading Floquet multiplier of the relative periodic orbit.

Twelve relative periodic orbits listed in table 4.1 (indicated by subscript F) are separated from the rest in the table. We refer to these orbits as the *first family* solutions, due to their remarkably similar physical and dynamical properties. The periods of the first family members are approximately integer multiples of the shortest relative periodic orbit, whose period is $T = 6.668$. Indeed, numerical continuations in Re and/or geometry parameters show that several first family members originated from bifurcations off the parent orbit $\text{RPO}_{F/6.668}$. For example, $\text{RPO}_{F/13.195}$ is born out of a period-doubling bifurcation at $Re = 2191$. As is shown in the next section, the first family orbits lie near each other in all state space visualisations, populating a small region of the state space. A detailed bifurcation analysis of the first family orbits is the subject of ongoing research [75].

4.6 State space visualisation of the fluid flows

With the available computational resources, today one can generate a large number of turbulent trajectories as solutions of the Navier–Stokes equations with various initial conditions. What can one learn from the resulting enormous amounts of data?

A routine approach is to seek to understand the statistical properties of physically relevant quantities such as velocity correlations, enstrophy, palinstrophy, etc. One objective of the program of determining *invariant solutions* is to go beyond a statistical description, and explore the state space *geometry* of long-time attractors of such dissipative flows. This should ultimately provide a coarse-grained partition of the state space into regions of qual-

itatively and quantitatively similar behaviours.

Embarking on this path, one is immediately confronted with several fundamental dilemmas with no known resolution:

1. *State space geometry.* Inertial manifolds and attracting sets of nonlinear dissipative flows are nonlinear, curved subsets of the full state space. Even for the Hénon attractor we only have a partial understanding of the topology [76, 77] and the existence of such attracting sets [78]. Our strategy for visualisation of the 'state space geometry' of the Navier–Stokes equations is to populate it by invariant solutions, e.g. equilibria, traveling waves, periodic orbits and relative periodic orbits, and capture the local "curvature" of the attractor by tracing out segments of their unstable manifolds and their heteroclinic connections (see, e.g., [47, 79])

2. *Measuring distances.* The distance between two fluid states is measured using some norm. There is no solid physical or mathematical justification for using the usual L_2 or 'energy' norm. For example, in some problems a Sobolev norm might be preferred in order to either penalize or emphasize the small scale structures (see, e.g., [80, 81, 82] and § 4.6.4). Furthermore, in presence of continuous and discrete symmetries, it is absolutely imperative that symmetries be reduced before a distance can be measured (see, e.g., Eq. 4.35); states on group orbits of nearby states can lie arbitrarily far in the state space. As different choices of a slice yield different distances, this introduces a further arbitrariness into the notion of 'distance'.

3. *Low-dimensional visualisations*. The state space of Navier–Stokes equations is infinite-dimensional. To visualize the geometry of the invariant solutions one inevitably projects the solutions to two- or three-dimensional subspaces. For a discussion of optimal projections that best illuminate the structure of an attractor, see [83].

Although we are in no position to resolve any of these issues in this paper, we will elucidate, through examples, the impact of the choice one makes in answering each question.

4.6.1 Choice of the norm

In this work, we use two rather different norms, the standard energy norm, and a hand-crafted 'low pass' norm. In what follows, we show how the choice of the norm can significantly alter the state space visualisations, and the conclusions drawn from them.

Let $\boldsymbol{u} = \sum_{km} \boldsymbol{u}_{km}(r) \exp(2\mathrm{i}\alpha kz + \mathrm{i}m_0 m\theta)$ denote the Fourier series of a velocity field $\boldsymbol{u}$ defined in a pipe of axial length $L = \pi/\alpha$. The variables $\boldsymbol{u}_{km}$ denote the Fourier coefficients corresponding to the axial and azimuthal directions as functions of the radial distance r. For two velocity fields $\boldsymbol{u}_1$ and $\boldsymbol{u}_2$, we define the L^2 inner product

$$\langle \boldsymbol{u}_1 | \boldsymbol{u}_2 \rangle_{L^2} = \frac{1}{2E_{\mathrm{HP}}} \int_V \boldsymbol{u}_1 \cdot \boldsymbol{u}_2 \, r \, d\theta \, dr \, dz \,, \tag{4.20}$$

$$= \frac{1}{E_{\mathrm{HP}}} \int_0^{1/2} r \, dr \sum_{k,m} \boldsymbol{u}^*_{1,km}(r) \cdot \boldsymbol{u}_{2,km}(r) \,, \tag{4.21}$$

where V denotes the cylindrical flow domain and E_{HP} is the kinetic energy of the Hagen-Poiseuille flow. In 4.21, we write the integral explicitly in terms of Fourier modes and radial integration, which in practice are approximated numerically. This inner product corresponds to the L^2 or the kinetic *energy norm*,

$$E(\boldsymbol{u}) = \frac{1}{2} \|\boldsymbol{u}\|^2_{L^2} = \frac{1}{2} \langle \boldsymbol{u} | \boldsymbol{u} \rangle_{L^2}. \tag{4.22}$$

We sometimes find it more informative to use a metric that emphasizes larger scale structures along the continuous symmetry directions. For this reason, we define the *'low pass'* metric,

$$\langle \boldsymbol{u}_1 | \boldsymbol{u}_2 \rangle_{LP} = \frac{1}{V} \int_0^{1/2} r dr \sum_{k,m} \frac{1}{1 + (\alpha k)^2 + (m_0 m)^2} \, \boldsymbol{u}^*_{1,km}(r) \cdot \boldsymbol{u}_{2,km}(r) \,, \tag{4.23}$$

which penalizes higher Fourier modes (short wavelengths. In the axial and azimuthal directions this is a variation of a Sobolev H^{-1} norm [84]: The weights are smaller for larger

values of k and m, hence shorter wavelengths are de-emphasized.

In the work reported here, we rely primarily on the energy norm Eq. 4.21, except for § 4.6.4 where we contrast state space visualisations using the energy and the low pass norms, and comment on their relative effectiveness in our searches for relative periodic orbits.

4.6.2 Global visualisations: Principal Component Analysis

We begin our investigation of state space with a data-driven method in order to obtain a general qualitative picture. The use of principal component analysis (PCA), otherwise known as proper orthogonal decomposition (POD) in the context of fluids, has been well documented (see e.g. [85]). Broadly speaking, the method extracts a set of orthogonal vectors that span the data with minimal residual, with respect to some norm.

Here we apply the method to extract principal components, relative to the mean $\bar{\hat{x}}$ of the data set of N states $\hat{x}_i$ in the symmetry-reduced state space, symmetrized with respect to g_θ. Singular value decomposition is applied to the matrix of inner products of the deviations $\tilde{\hat{x}}_i = \hat{x}_i - \bar{\hat{x}}$,

$$R_{ij} = \frac{1}{N-1}\langle \tilde{\hat{x}}_i | \tilde{\hat{x}}_j \rangle_{\mathrm{L}^2} , \qquad R = U\, S\, V^T , \tag{4.24}$$

from which the j^{th} principal component is calculated

$$\boldsymbol{e}_j = \sum_{i=1}^{N} \tilde{\hat{x}}_j U_{ij} , \qquad \hat{\boldsymbol{e}}_j = \boldsymbol{e}_j / \langle \boldsymbol{e}_j | \boldsymbol{e}_j \rangle_{\mathrm{L}^2} . \tag{4.25}$$

Each principal component $\hat{\boldsymbol{e}}_j$ has the property that the root-mean-square of the projection $p_j = \langle \tilde{\hat{x}}_i(t) | \hat{\boldsymbol{e}}_j \rangle$ (taking the mean over i) equals the j^{th} singular value, S_{jj}, of the correlation matrix.

Principal components were extracted from 2000 uncorrelated symmetry-reduced states obtained from ergodic trajectories. Fig. 4.3 shows all our relative periodic orbits, 5 trav-

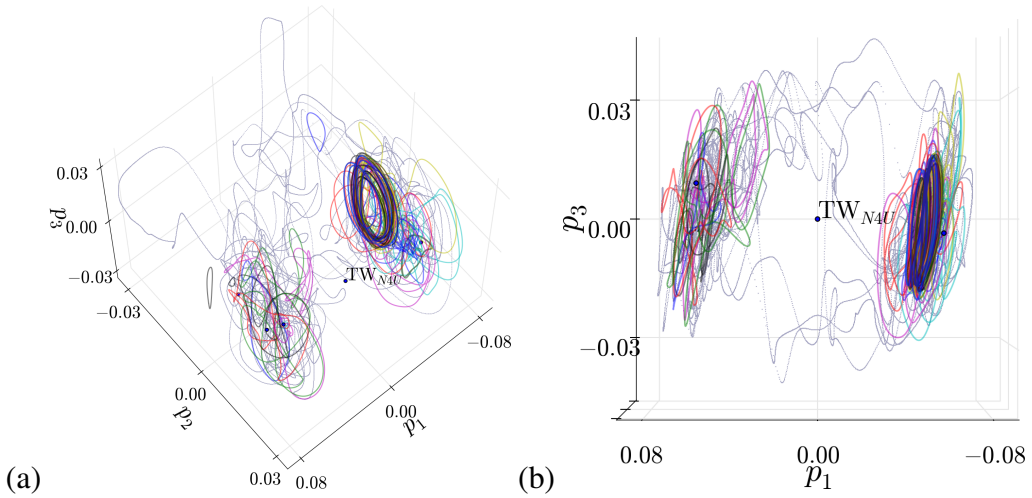

Figure 4.3: (Colour online) Relative periodic orbits (closed curves, different colors), 5 traveling waves (marked with black dots), and an two turbulent trajectories (gray, transparent dots) of the pipe flow projected onto first three principal components (4.25), two different viewing angles.

eling waves, and two turbulent trajectories projected onto the principal components, computed as above. There are some notable observations about Fig. 4.3: Firstly, periodic orbits appear to be localized on two sides of the $p_1 = 0$ plane, and the turbulent trajectories rarely switch from one side to other. The first Fourier mode slice reduces the continuous translation symmetry of pipe flow but the discrete half-rotation symmetry g_θ still remains; the two sides of Fig. 4.3 are related to each other by this discrete symmetry operation. Also note that the highly symmetric $N4$ traveling wave $\mathrm{TW}_{N4U/3.28}$, which is invariant under g_θ, appears to lie at the origin of (p_1, p_3) plane.

It is clear from Fig. 4.3 that the principal component $\hat{e}'_1$ is aligned along the symmetry direction. This makes the information contained along this direction redundant, since each solution with $p_1 > 0$ has a copy with $p_1 < 0$. As we are most interested in the details of the turbulent set and invariant dynamical behaviour of the system, our next step is to reduce the discrete g_θ-symmetry. For this purpose, we define the 'fundamental domain' [68] as $p_1 > 0$ and bring all our data from turbulence simulations and invariant solutions to this half of the state space. With the desymmetrized turbulence data, we recompute principal components $\tilde{e}'_j$, which we will refer to as 'fundamental domain principal components'.

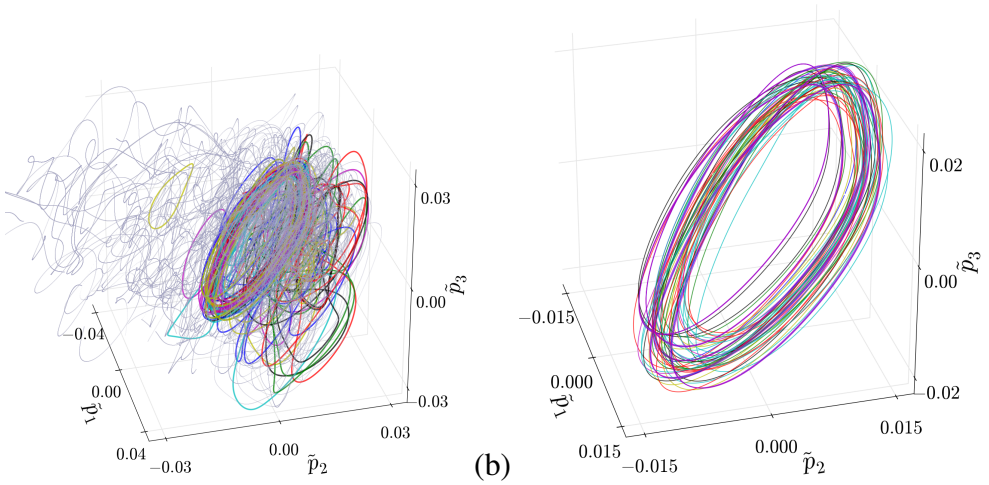

Figure 4.4: (Colour online) (a) Relative periodic orbits (closed curves of various colors) and 5 turbulent trajectories (gray dots) projected onto first three fundamental domain principal components. (b) 11 orbits, which appear to fill out a region of the state space.

Figure 4.4 shows relative periodic orbits and turbulent trajectories projected onto the three dominant fundamental domain principal components. In Fig. 4.4, we no longer have two "clouds" and relative periodic orbits are mostly located in the region of state space where turbulent trajectories spend most of their time. One striking observation from 4.4 (*a*) is that a subset of relative periodic orbits seem to be located close to one another and their projections also qualitatively resemble each other. These are the relative periodic orbits labelled with subscript *F* in table 4.1. We have already noted that the periods of these relative periodic orbits are approximately integer multiples of the shortest one. Their qualitative similarities in the state space projections of Fig. 4.4 provide further evidence that these orbits are related to one another, possibly through sequences of bifurcations at other values of the *Re* number [75].

In order to develop more intuition about the state space geometry, we reduce the flow further to a Poincaré section defined by

$$\langle \tilde{x}_{\mathcal{P}} - \langle \tilde{x} \rangle | \tilde{\boldsymbol{e}}'_3 \rangle_{L^2} = 0\,, \quad \langle \hat{v}(\tilde{x}_{\mathcal{P}}) | \tilde{\boldsymbol{e}}'_3 \rangle_{L^2} > 0\,. \tag{4.26}$$

In the projections of Fig. 4.4, the Poincaré section Eq. 4.26 corresponds to $\tilde{p}_3 = 0$ plane,

and for visualisations of Fig. 4.5, we project intersections onto the $(\tilde{e}'_1, \tilde{e}'_2)$ plane. However, it should be noted that this Poincaré section is a codimension-1 hyperplane in the symmetry reduced state space. Fig. 4.5 (*a*) shows 8560 intersections (grey) of turbulent trajectories with the Poincaré section Eq. 4.26 that were obtained from 147 individual runs, along with those (red and green) of relative periodic orbits.

It is clear in Fig. 4.5 (*a*) that the turbulence visits the region containing relative periodic orbits more often than the rest of the state space. In Fig. 4.5, the 'first family' of relative periodic orbits shown in Fig. 4.4 are marked red, except for $\mathrm{RPO}_{F/6.668}$, the shortest one, which is colored black. Fig. 4.5 (*b*) is a close-up view of the region containing relative periodic orbits, enclosed by the dashed-rectangle in Fig. 4.5 (*a*) and similarly, Fig. 4.5 (*c*) is a close-up of the region containing the first family, marked with the dashed rectangle on figure 4.5 (*b*). In Fig. 4.5 (*d*), we show orbits which approximate the three-dimensional unstable manifold of $\mathrm{RPO}_{F/6.668}$ overlaid over Fig. 4.5 (*c*). (The computational aspects of tracing out the unstable manifold are discussed in § 4.6.3.)

The global visualisations of dynamics we presented above provide us with insights about the state space structure: the most important observation is that turbulent dynamics frequently visits the neighbourhoods of the relative periodic orbits found in this work. In addition, the "first family" orbits—the set sharing similar physical and stability properties—appear close to each other in all projections of Fig. 4.4 and Fig. 4.5. Furthermore, the unstable manifold of the shortest period member of this family visits the intersections of the other members of the family on Fig. 4.4, which provides additional evidence that these orbits emerge from a common bifurcation sequence [75].

Note that in the zoomed-in projection of the Poincaré section, Fig. 4.5 (*c*), some parts are often visited by the turbulent trajectories (as indicated by the overlapping markers), while there are other regions, even the ones that appear close to the frequently visited regions, that tend to remain empty. This illustrates why measuring distances in the state space of a turbulent fluid is a hard problem: Two points in state space that are seemingly

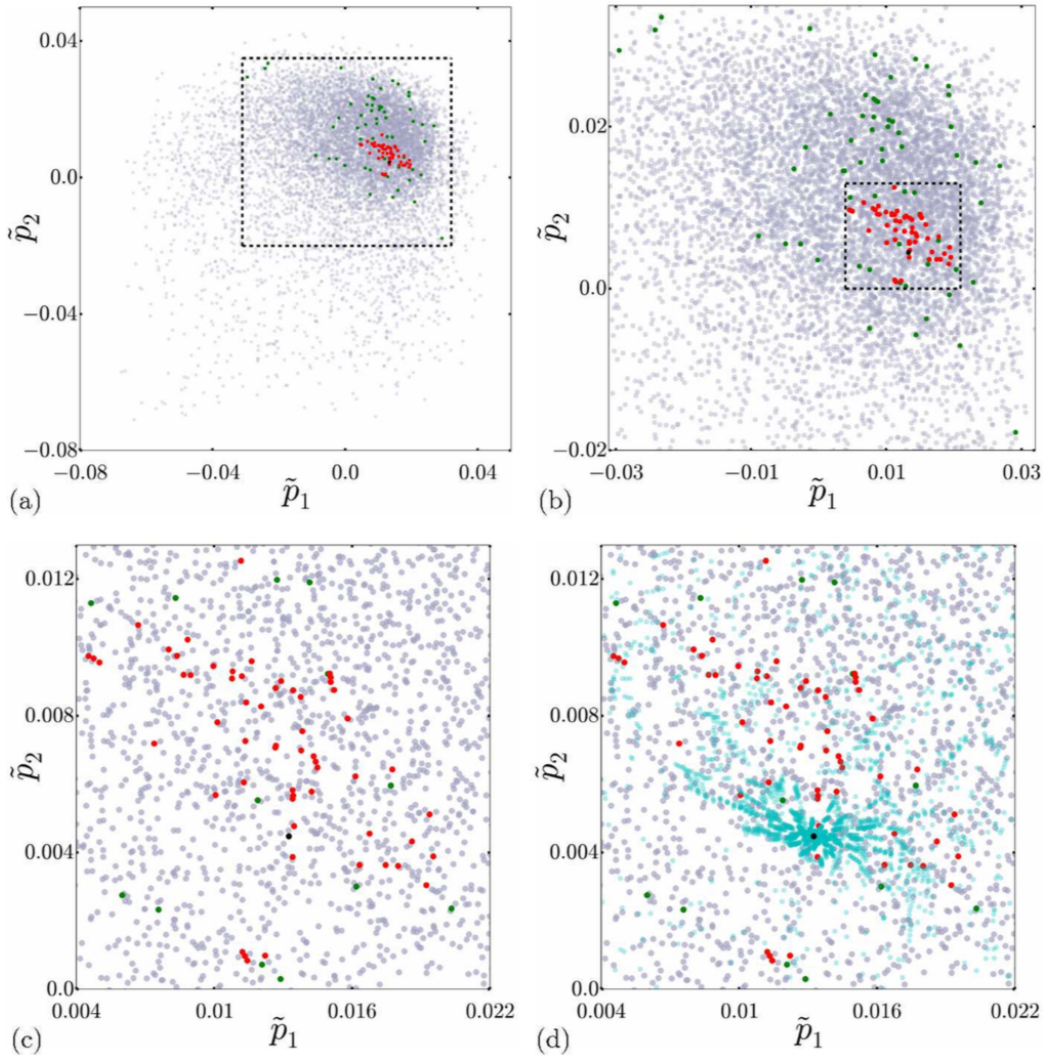

Figure 4.5: (Colour online) (a) Turbulent trajectories (grey), and relative periodic orbits (black: $\mathrm{RPO}_{F/6.668}$, red: other members of the first family, green: the rest) on the Poincaré section 4.26. (b) Zoom-into the region enclosed by the dashed-rectangle on (a). (c) Zoom-into the region enclosed by the dashed-rectangle on (b). (d) Trajectories (cyan) on the unstable manifold of $\mathrm{RPO}_{F/6.668}$ added to (c).

very close to each other in L_2 or a similar norm may be completely separated dynamically, since the geometry of the manifold on which the turbulence takes place can be highly convoluted.

While the global visualisations give us a qualitative view of the state space, they cannot tell us much about the finer structure of the turbulent state space. This is not surprising since the state space in question is very high dimensional; and it is very unlikely that we can obtain a complete picture of dynamics from two- and three-dimensional global visualisations. For a better understanding of the state space geometry, one must study the neighbourhoods of important invariant solutions individually, as illustrated in the next section.

4.6.3 Local visualisations

Global visualisations of the state space in Fig. 4.4 and Fig. 4.5 support the earlier suggestion that the members of the first family of relative periodic orbits, embedded in turbulence and listed separately in Table 4.1, may be dynamically related to each other. The shortest period member $\text{RPO}_{F/6.668}$ of first family has three unstable ($|\Lambda_i| > 1$) Floquet multipliers:

$$\Lambda_{1,2} = -0.1698 \pm i1.418\,, \quad \Lambda_3 = -1.340\,. \tag{4.27}$$

This renders the associated unstable manifold of $\text{RPO}_{F/6.668}$ three-dimensional even after the symmetry reduction of the space and time translation directions. Leading complex conjugate Floquet multipliers imply spiral-out dynamics in the associated neighbourhood, while the negative-real third Floquet multiplier implies that locally there exists a topologically Möbius band-shaped dynamics such as the one observes in period-doubling bifurcations. In the following, we numerically approximate and visualize these one- and two-dimensional unstable sub-manifolds.

[86] numerically approximated the one- and two-dimensional unstable manifolds of

relative periodic orbits in a Kuramoto–Sivashinsky system. In those computations, a local Poincaré section was constructed in the neighbourhood of a periodic orbit where they initiated orbits whose dynamics approximately covered the linear unstable manifold; hence their forward integration approximated the unstable manifold away from the linearized neighbourhood. This strategy was adapted for calculating one-dimensional unstable manifold of the localized "edge state" relative periodic orbit of the pipe flow in [67], in order. We apply here this method to a relative periodic orbit embedded in turbulence, with a three-dimensional unstable manifold, a case that was not considered in the aforementioned studies.

To this end, we first define a local Poincaré section in the neighbourhood of $\mathrm{RPO}_{F/6.668}$ as the half-hyperplane

$$\langle \hat{x}_{\mathcal{P}} - \hat{x}_p | \hat{v}(\hat{x}_p) \rangle_{L^2} = 0\,, \quad \langle \hat{v}(\hat{x}_{\mathcal{P}}) | \hat{v}(\hat{x}_p) \rangle_{L^2} > 0\,, \tag{4.28}$$

where $\hat{x}_p$ is a point on $\mathrm{RPO}_{F/6.668}$, which we have arbitrarily chosen as its intersection with the global Poincaré section Eq. 4.26. The relative periodic orbit $\mathrm{RPO}_{F/6.668}$ is a fixed point of the Poincaré map on the section Eq. 4.28 with stability multipliers equal to its Floquet multipliers. Associated Floquet vectors, however, need to be projected onto this section. This is a two-stage process since we compute the Floquet vectors as eigenfunctions V_i of the eigenvalue problem

$$g_z(-l_p)\frac{df^{T_p}(\hat{\boldsymbol{u}}_p)}{d\hat{\boldsymbol{u}}_p}V_i = \Lambda_i V_i\,, \tag{4.29}$$

in full state space. First we project these vectors onto the slice as

$$\hat{V}_i = V_i - \frac{\langle t' | V_i \rangle_{L^2}}{\langle t(\hat{x}_p) | t' \rangle_{L^2}} t(\hat{x}_p), \tag{4.30}$$

where $\hat{V}_i$ denotes the projected vector on the slice. Then we project translation-symmetry

reduced Floquet vectors onto the Poincaré section as

$$\hat{V}_{i,\mathcal{P}} = \hat{V}_i - \frac{\langle \hat{v}(\hat{x}_p)|\hat{V}_i\rangle_{L^2}}{\langle \hat{v}(\hat{x}_p)|\hat{v}(\hat{x}_p)\rangle_{L^2}}\hat{v}(\hat{x}_p)\,. \tag{4.31}$$

Projections Eq. 4.30 and Eq. 4.31 onto slice hyperplane Eq. 4.14 and onto the Poincaré section hyperplane (4.28) follow the same geometrical principle as the Appendix of [67].

In order to visualise the one-dimensional unstable submanifold of $\text{RPO}_{F/6.668}$, we initiate trajectories from the points

$$\hat{x}_{\mathcal{P}}(\delta) = \hat{x}_p \pm \epsilon|\Lambda_3|^{\delta}\hat{V}_{3,\mathcal{P}}\,, \quad \text{where} \quad \delta \in [0,1)\,. \tag{4.32}$$

These initial conditions approximately cover the locally linear one-dimensional piece of the unstable manifold in $\hat{V}_{3,\mathcal{P}}$ direction such that first-return of $\tilde{x}_{\mathcal{P}}(0)$ coincides with initial location of $\tilde{x}_{\mathcal{P}}(1)$. We discretised Eq. 4.32 by choosing four equidistant points in δ and set $\epsilon = 10^{-3}$ (Floquet vectors are normalized such that $\|x_p\|_{L^2} = \|V_i\|_{L^2}$). We forward-integrate these initial conditions while recording their intersections with the Poincaré section. Eq. 4.28. 4.6 (*a,b*) shows the first 25 intersections of these orbits with the Poincaré section on two-dimensional projections and panels (*c,d*) shows one of these orbits in a three-dimensional projection along with $\text{RPO}_{F/6.668}$ and $\text{RPO}_{F/13.195}$. The origin of the projections in Fig. 4.6 is $\hat{x}_p$ and the projection coordinates are

$$\begin{aligned}
e_1 &= \langle \hat{x}|\mathrm{Re}\,\hat{V}_{1,\perp}\rangle_{L^2}\,,\\
e_2 &= \langle \hat{x}|\mathrm{Im}\,\hat{V}_{1,\perp}\rangle_{L^2},\\
e_3 &= \langle \hat{x}|\hat{V}_{3,\perp}\rangle_{L^2}\,,\\
e_4 &= \langle \hat{x}|\hat{V}_{6,\perp}\rangle_{L^2},\\
e_5 &= \langle \hat{x}|\hat{v}(\hat{x}_p)/\,\|\hat{v}(\hat{x}_p)\|_{L^2}\rangle_{L^2}
\end{aligned} \tag{4.33}$$

where $\hat{V}_{6,\perp}$ is the symmetry-reduced Floquet vector in the least stable direction (comes

after marginal axial and temporal translation directions), and subscript $\perp$ indicates that these vectors are Gram-Schmidt orthonormalized.

Fig. 4.6 (*a,b*) shows that one-dimensional shape of locally linear dynamics is preserved as it is extended far away from the origin. Trajectories in Fig. 4.6 (*a,b*) spread in a higher-dimensional manifold once they reach the neighbourhood of period-doubled $\mathrm{RPO}_{F/13.195}$. For additional comparison, in Fig. 4.6 (*c,d*) we plot different three-dimensional projections of $\mathrm{RPO}_{F/6.668}$, the $\delta = 0$ in (4.32) orbit, and $\mathrm{RPO}_{F/13.195}$ in different three-dimensional projections. Qualitative similarities between the shape of the unstable manifold and $\mathrm{RPO}_{F/13.195}$ are remarkable. For a quantitative conclusion, one should search for a heteroclinic connection from three-dimensional unstable manifold of $\mathrm{RPO}_{F/6.668}$ to the relative periodic orbit $\mathrm{RPO}_{F/13.195}$. That, however, is beyond the scope of the current work.

For further comparison, we visualise the streamwise velocity and vorticity isosurfaces of $\mathrm{RPO}_{F/6.668}$, $\mathrm{RPO}_{F/13.195}$, and three-snapshots on the unstable manifold of $\mathrm{RPO}_{F/6.668}$ in Fig. 4.7. All panels of Fig. 4.7 correspond to their respective intersections with the Poincaré section Eq. 4.28, and only one-eighth (one-quarter in azimuthal and one-half in axial directions) of the pipe is shown. The one-eighth visualisation suffices, since we work in the subspace with 4-fold symmetry in the azimuthal direction, and the other half of the pipe in the axial direction can be obtained from the first half by the shift-and-reflect Eq. 4.4 symmetry.

While all panels of Fig. 4.7 appear similar, they differ in details. Fig. 4.7 (*d*), the initial point on the unstable manifold, is virtually indistinguishable from $\mathrm{RPO}_{F/6.668}$ in Fig. 4.7 (*a*). Flow structures of $\mathrm{RPO}_{F/13.195}$ at its two-intersections with the Poincaré section, Fig. 4.7 (*b,c*), differ from $\mathrm{RPO}_{F/6.668}$ and from each-other only in minute details; one has to compare the streak and roll sizes one-by-one. These nuances are reflected on the selected points on the unstable manifold shown in Fig. 4.7 (*d,e,f*), although only identifiable after a careful inspection. These difficulties illustrate the power of state space visualisation (cf. Fig. 4.6), without which the relation of $\mathrm{RPO}_{F/6.668}$ to $\mathrm{RPO}_{F/13.195}$ would have been very

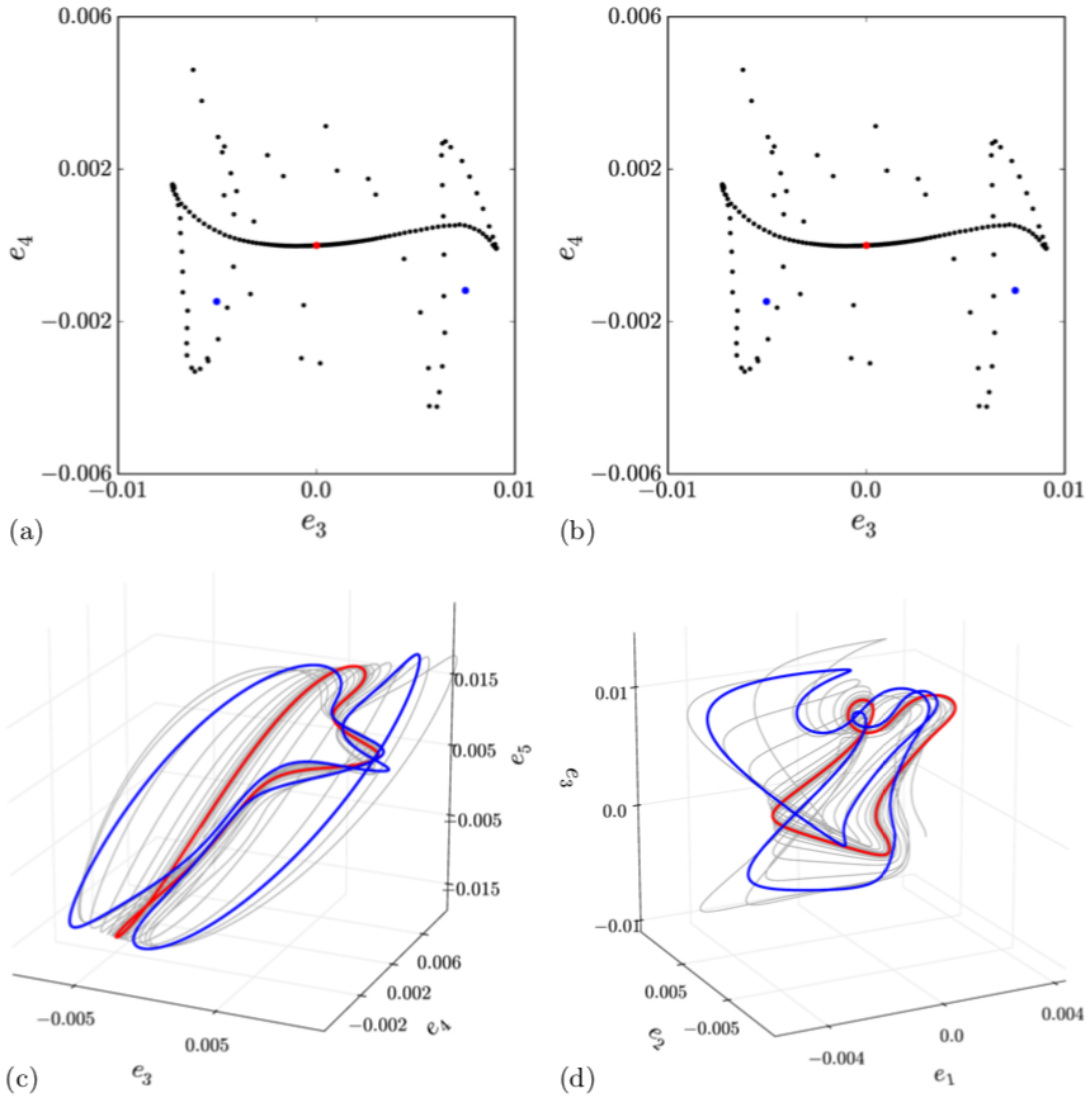

Figure 4.6: (a,b) One-dimensional submanifold in the unstable manifold of $\text{RPO}_{F/6.668}$ capturing locally linear dynamics in the $\hat{V}_{3,\mathcal{P}}$ direction in the Poincaré section, two projections onto local coordinates Eq. 4.33. Fixed point corresponding to $\text{RPO}_{F/6.668}$ is at the origin (red), and the 2-cycle $\text{RPO}_{F/13.195}$ is marked blue. (c,d) Three-dimensional projections of one ($\delta = 0$) of the 8 trajectories in panels (*a,b*).

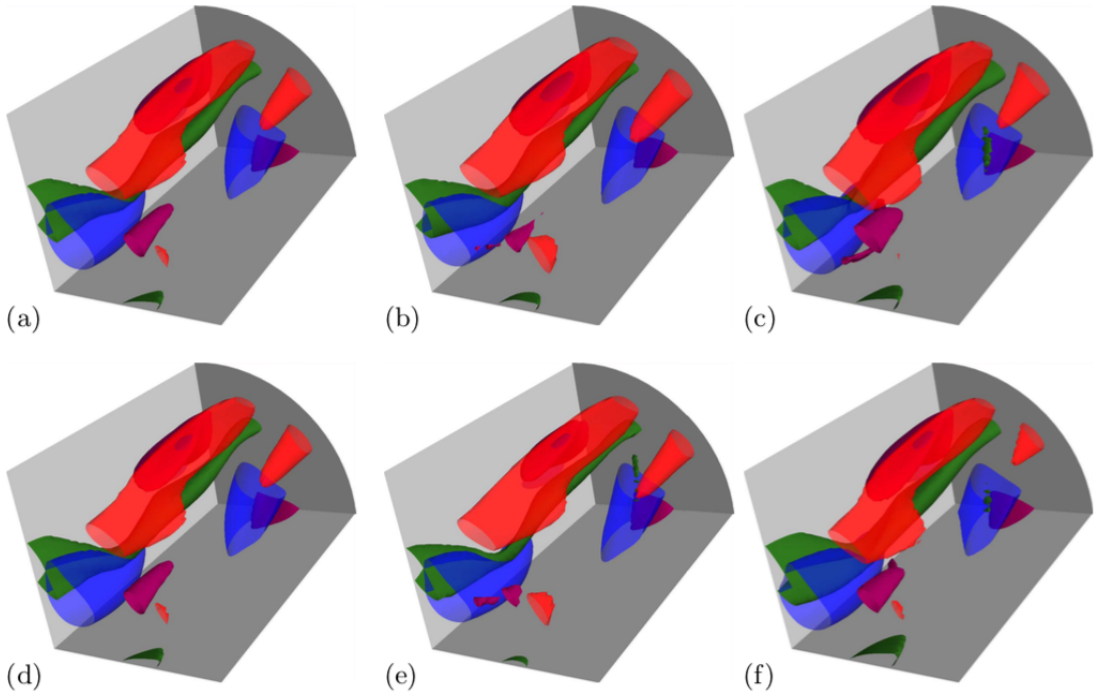

Figure 4.7: Streamwise velocity isosurfaces at $u = \pm 0.5 U_b$ (red and blue) and streamwise vorticity isosurfaces at $\omega_z = \pm 2.4 (U_b/D)$ (purple and green) of (a) $\text{RPO}_{F/6.668}$; (b,c) $\text{RPO}_{F/13.195}$; and (d,e,f) the unstable manifold of $\text{RPO}_{F/6.668}$ at discrete times $n = 0, 23, 24$.

hard to elucidate.

A set of initial conditions that approximately covers the linearised dynamics in the plane $(\mathrm{Re}\,\hat{V}_{1,\mathcal{P}}, \mathrm{Im}\,\hat{V}_{1,\mathcal{P}})$ is given by

$$\tilde{x}_{\mathcal{P}}(\phi, \delta) = \hat{x}_p \pm \epsilon |\Lambda_1|^{\delta} (\mathrm{Re}\,\hat{V}_{1,\mathcal{P}} \cos\phi + \mathrm{Im}\,\hat{V}_{1,\mathcal{P}} \sin\phi)\,, \quad \delta \in [0, 1)\,, \quad \phi \in [0, 2\pi) \tag{4.34}$$

We discretise Eq. 4.34 by choosing 4 equidistant points in δ and 36 points in ϕ and set $\epsilon = 10^{-3}$. First three intersection of these initial conditions with the Poincaré section Eq. 4.28 are visualised in the projection Fig. 4.8 (*a*) in different colours, where black points correspond to the initial conditions. This figure illustrates the motivation for the particular approximation: Initial conditions Eq. 4.34 define an elliptic band in the $(\mathrm{Re}\,\hat{V}_{1,\mathcal{P}}, \mathrm{Im}\,\hat{V}_{1,\mathcal{P}})$ plane, such that the inner ellipse is mapped to the outer one by the linearised dynamics on the Poincaré section. The totality of these initial conditions captures well the linearised

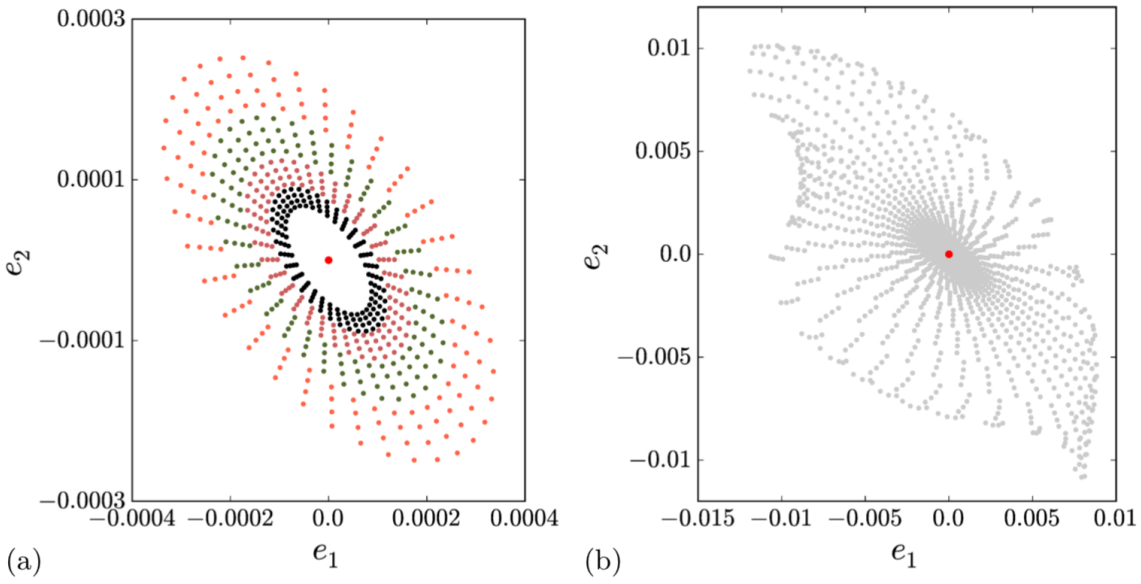

Figure 4.8: Two-dimensional submanifold in the unstable manifold of $\mathrm{RPO}_{F/6.668}$ capturing locally linear dynamics in the $\mathrm{Re}\,\hat{V}_{1,\mathcal{P}}, \mathrm{Im}\,\hat{V}_{1,\mathcal{P}}$ plane in the Poincaré section projected onto local coordinates Eq. 4.33. Panel (a) shows initial conditions (black) and their orbits' first 3 intersections with the Poincaré section, in different colours. 15 intersections shown in (b) illustrating global shape of the $2D$ submanifold.

dynamics in this neighbourhood.

Fig. 4.8 (*a*) also illustrates the validity of linearised dynamics as each initial condition simply expands and rotates according to real and imaginary part of V_1, when their distance to $\hat{x}_p$ is of order 10^{-4}. In Fig. 4.8 (*b*), we show the same projection for 15 intersections of these orbits on the Poincaré section as they leave the neighbourhood of the relative periodic orbit. At this stage, the shape is no longer an ellipse but it is starting to develop corners, possibly due to being distorted by a stable manifold. It should be noted, however, that the sub-manifold associated with the linearised dynamics on the plane $(\mathrm{Re}\,\hat{V}_{1,\mathcal{P}}, \mathrm{Im}\,\hat{V}_{1,\mathcal{P}})$ is still two-dimensional. Note that the scales of axes in Fig. 4.8 (*b*) are about two orders of magnitude larger than those on Fig. 4.8 (*a*), and also that they are comparable to scales of Fig. 4.5 (*d*). In other words, a relative periodic orbit not only guides the dynamics in its immediate neighbourhood, but it indeed guides, through its unstable manifold, nearby motions at considerable finite distances.

The above Poincaré sections illustrate the ways in which a relative periodic orbit shapes

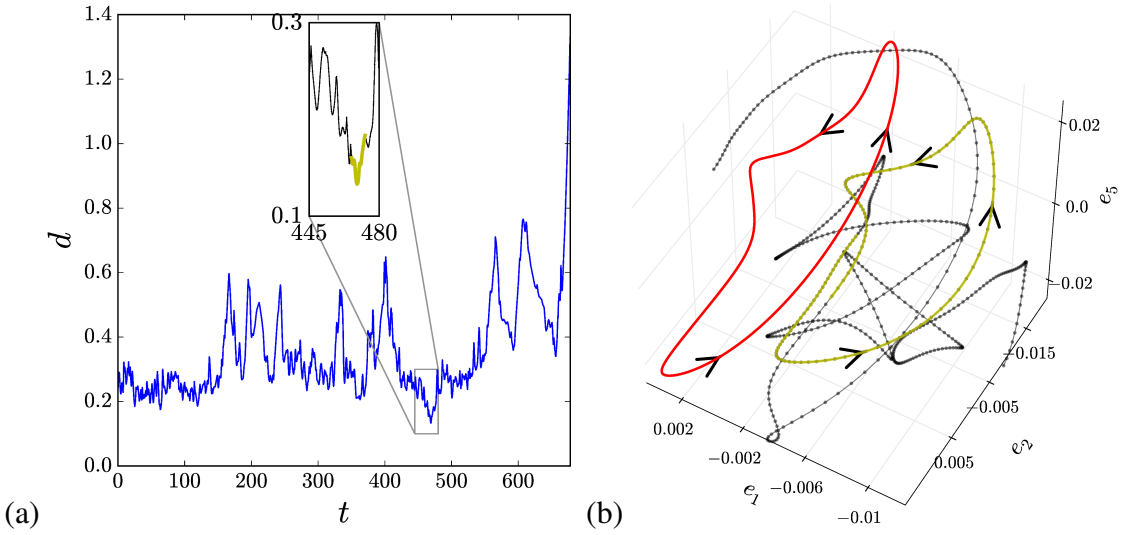

Figure 4.9: (a) Minimum distance (4.35) between a long turbulent trajectory $\hat{x}_{turb}(t')$ and the relative periodic orbit $\text{RPO}_{F/6.668}$. Inset: A time interval containing the closest approach. (b) $\text{RPO}_{F/6.668}$ (red) and a shadowing segment (corresponding to the inset of panel a) of a turbulent trajectory (dotted line) visualized as a projection onto (4.33). The closest approach of the turbulent trajectory to $\text{RPO}_{F/6.668}$, $d < 0.15$, is highlighted yellow.

the geometry of its immediate neighborhood. However, as in the example at hand the unstable manifold Poincaré section is three d, it is hard to discern any structure in the ergodic sea in two d projections such as Fig. 4.5: in all our Poincaré sections the ergodic sea appears to be structureless cloud, exhibiting no foliation typical of —let's say—Lorenz attractor or Kuramoto–Sivashinsky attractor [87]. The influence of a relative periodic orbit is here easier to visualize by studying shadowing episodes, i.e., the turbulent trajectory's visits to a given relative periodic orbit's neighbourhood, such as Fig. 4.9 (a). Here we have defined the minimum distance between trajectories labelled '$turb$' and 'RPO' in the fully symmetry-reduced state space (continuous symmetry reduced by Eq. 4.18, the discrete half-rotation symmetry g_θ Eq. 4.5 reduced to the fundamental domain), measured in the energy norm Eq. 4.22, as

$$d(t) = \min_{t' \in [0, T_{\text{RPO}}]} \frac{\|\tilde{x}_{turb}(t) - \tilde{x}_{\text{RPO}}(t')\|_{L^2}}{\|\tilde{x}_{turb}(t)\|_{L^2}} \tag{4.35}$$

Compared to the typical $\text{RPO}_{F/6.668}$ linearized neighborhood scales (see Fig. 4.6), the

yellow shadow in Fig. 4.9 (b) is a considerable distance away, but it still completes one co-rotating shadowing period very nicely. Such shadowing episodes offer further support to our main thesis, that relative periodic orbits, together with their stable/unstable manifolds, shape the state-space dynamics within their local neighborhoods.

4.6.4 Local visualisation: energy norm vs. lowpass norm

As our final example of a local visualization of the state space, we examine the local unstable manifold of a traveling wave. The primary goal here is to show with this example is how profoundly the choice of the inner product (or norm) can affect the visualisation, and the conclusions drawn from it. Since in the slice the traveling waves reduce to equilibria, there is no need for a Poincaré section. Therefore, visualizing low-dimensional unstable manifolds of traveling waves is more straightforward compared to those of relative periodic orbits discussed above.

Fig. 4.10 shows a two-dimensional unstable submanifold of $\mathrm{TW}_{1.968}$. Note that the unstable manifold of this traveling wave is nine-dimensional ($d_U = 9$ in Table 4.1). The visualized two-dimensional submanifold corresponds to its most unstable subspace characterized by the largest linear stability exponent of the traveling wave. This dominant exponent is complex valued, with a complex eigen-direction V_1 which defines a two-dimensional subspace $(\mathrm{Re}\, V_1, \mathrm{Im}\, V_1)$. The three-dimensional visualizations of Fig. 4.10 are obtained by projecting each state to the subspace formed by $(\mathrm{Re}\, V_1, \mathrm{Im}\, V_1, V_2)$ where V_2 is the third eigen-direction, with a real linear stability exponent.

All computations are carried out in a slice with the traveling wave $\mathrm{TW}_{1.968}$ used as the template for symmetry reduction, and placed at the origin of the plots. The unstable submanifold (gray curves) is approximated by forward-integrating several small perturbations to the traveling wave in the direction $\mathrm{Re}\, V_1$. Because of the instability of the traveling wave, the trajectories spiral away from the origin. The spiraling nature of the trajectories is due to the complex stability exponent. In a small neighborhood of the traveling wave, the

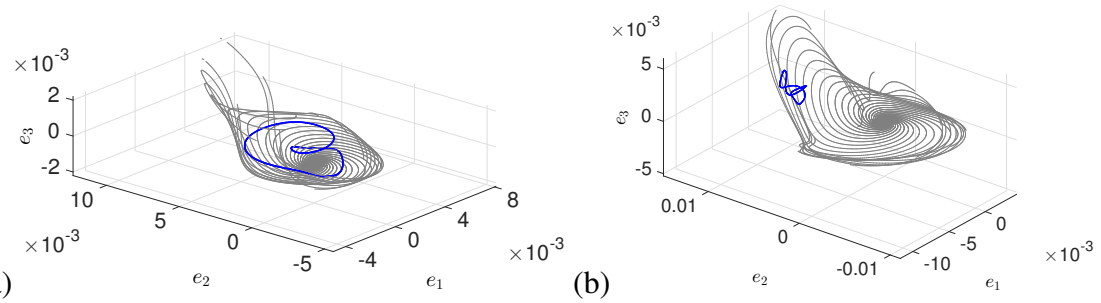

Figure 4.10: Low-dimensional state space visualisation of the traveling wave $\mathrm{TW}_{1.968}$ (origin) and the relative periodic orbit $\mathrm{RPO}_{11.696}$ (blue). A two-dimensional unstable submanifold of the traveling wave is approximated by perturbations (gray curves) around the traveling wave (see the text for the details). Both panels show the same objects projected to the same three-dimensional subspace. Two types of inner products are used for the projections: (a) Low pass inner product 4.23, (b) L^2 inner product 4.21.

ensemble of the trajectories approximates the two-dimensional unstable submanifold that is tangent to the plane $(\mathrm{Re}\, V_1, \mathrm{Im}\, V_1)$. Away from the traveling wave this approximation fails and the trajectories diverge.

Also shown in Fig. 4.10 is the relative periodic orbit $\mathrm{RPO}_{11.696}$ (blue curve). The two panels show the same objects projected to the same subspace $(\mathrm{Re}\, V_1, \mathrm{Im}\, V_1, V_2)$. The difference is that in panel (*a*) the low pass inner product Eq. 4.23 is used for the projection while in panel (b) the L^2 inner product Eq. 4.21 is used.

In the low pass -projection, the relative periodic orbit sits near the traveling wave and appears to be shaped by its unstable manifold. In the L^2 projection, however, the relative periodic orbit appears to lie rather far from the traveling wave, and there is no hint that their shapes are related. We attribute this to the fact that the low pass norm filters small scale features, assessing the distance between fluid states based on their large-scale structures. In the L^2 norm, on the other hand, even minute small-scale differences between two states contribute to the computed distance.

We close by noting that the low pass norm was also used to detect near-recurrences of ergodic trajectories. These near-recurrences then served as the initial Newton iteration guesses for obtaining the relative periodic orbits reported in Table 4.1. We find that the

recurrences measured in the low pass norm tend to converge to relative periodic orbits more frequently than the recurrences measured in the energy norm. A similar observation was reported by [52].

4.7 Conclusion and perspectives

We investigated relative periodic orbits embedded in transitionally turbulent pipe flow confined to a small computational domain. These orbits were found by Newton-type searches, using near-recurrences of the turbulent flow as initial guesses to generate dynamically-relevant solutions. Even in our minimal domain, made small by unphysical symmetry restrictions, this turned out to be a daunting task, practicable only after reduction of problem's continuous symmetry and, in some cases, requiring also the multiple shooting Newton method.

Nonetheless, we were able to identify 48 distinct relative periodic orbits with numerical precision of 10^{-6} or smaller. While this, to the best of our knowledge, is the largest number of periodic orbits for a three-dimensional turbulent flow found so far, the analysis of § 4.6.2 shows that only some of the state-space visited by turbulence are populated by the set of relative periodic orbits found so far. Nevertheless, our relative periodic orbits do occupy a region of the state space frequently visited by turbulent trajectories, suggesting that additional searches for relative periodic orbits are needed to adequately represent a larger portion of state space. This is consistent with our expectation that in the state space, turbulence is "guided" by the exact invariant solutions.

Our main result is that there is an intrinsic geometry of turbulence, but that one has to explore the Navier–Stokes symmetry-reduced state space very closely in order to discern it. This geometry does not follow from naïve traditional statistical assumptions, as illustrated here by the state-space visualisations of § 4.6. Principal component analysis (PCA), which we used for global projections of the dynamics in 4.6.2, treats turbulent data as if it were a multivariate Gaussian distribution. The true global attractor is in no sense a Gaussian; the

intrinsic geometry of turbulence revealed here is dictated by exact time-invariant solutions of Navier–Stokes equations.

Our conclusions are not surprising to a nonlinear dynamicist experienced in working with low-dimensional dynamical systems and their strange attractors, yet the notion that there is an intrinsic geometry to Navier–Stokes long-time dynamics is not as well appreciated in the turbulence community. This under-appreciation is historical, stemming from times when we lacked computational tools to determine the non-trivial exact invariant solutions of Navier–Stokes equations. In this regard, the primary contribution of this paper is the demonstration of the computational feasibility of studying pipe-flow turbulence as a dynamical system. For example, consider Fig. 4.5 where 147 individual turbulent runs were necessary to obtain a very rough feeling for how turbulent trajectories are distributed in the state-space. In the dynamical systems approach, it took 8 carefully chosen trajectories to reveal the shape of $\mathrm{RPO}_{F/6.668}$'s unstable manifold.

Given the exploratory nature of this project, many of its intermediate steps were carried out manually, yet most of these could be automated. The first step would be to initiate relative periodic orbit Newton searches by detecting near-recurrences of turbulent flows without human supervision. A slightly more involved step — time-adaptive integration of symmetry-reduced dynamics — will probably be necessary when the azimuthal rotation symmetry is reduced simultaneously with axial translations. We circumvented this issue here by restricting dynamics to the shift-and-reflect invariant subspace, which precludes continuous rotations. This restriction is unphysical and not present in the full problem.

Our explorations of the state-space geometry relied on visualisations of relative periodic orbits and their unstable manifolds. It is already apparent from our data in Table 4.1 that this strategy has limited applicability since all but two invariant solutions we found have unstable manifolds of dimension larger than 3. Even though partial visualisations of the unstable manifold in § 4.6.3 were insightful, there is no guarantee that this approach can extend to larger computational domains. Ultimately, one needs to develop new methods

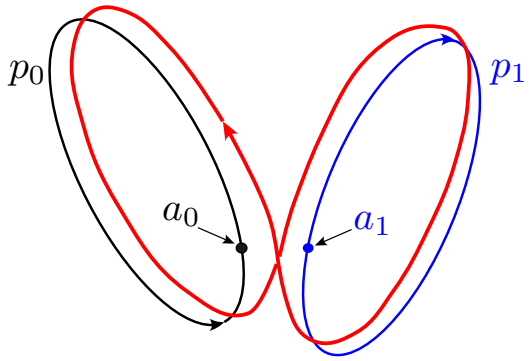

Figure 4.11: An illustration of the multi-point shooting method. A long periodic orbit (red) is obtained from shorter periodic orbits p_0 (black) and p_1 (blue) with periods T_0 and T_1, respectively. Multi-point shooting attempts to find the shortest orbit that shadows both p_0 and p_1, with period T that is approximately the sum of the periods of the shorter orbits, $T \simeq T_0 + T_1$.

for systematic study of high-dimensional manifolds, a dynamical notion of 'distance' that does not depend on the particular choice of norm, and geometric criteria for distinguishing qualitatively different dynamics in state-space.

In conclusion, we reported here our progress in dynamical study of moderate-*Re* turbulence in the context of pipe flow. In particular, we demonstrated that embedded within this flow are relative periodic orbits and that they shape dynamics in their respective neighbourhoods through their unstable manifolds. This required various technical obstacles to be overcome, which forced us to restrict this exploratory study to a small symmetry-restricted computational cell. In this sense, we can say that the dynamical approach to turbulence is still in its infancy, but the stage is now set for study of dynamics of wall-bounded shear flow turbulence in its full glory.

Table 4.1: The list of the invariant solutions reported in this work. Average rate of dissipation $\bar{D}$, average down-stream phase velocity $\bar{c}$, dimension of the unstable manifold d_U, real part of the largest stability eigenvalue / Floquet exponent μ^{max} is shown. Last column corresponds to the imaginary part ω of the leading stability eigenvalue for traveling waves, and phase θ of the leading Floquet multiplier for relative periodic orbits. Traveling waves are labeled by their dissipation rate $\bar{D}$, relative periodic orbits by their period T. A family of twelve relative periodic orbits which appear to have similar physical properties are grouped together and labeled with subscript F. Solutions marked with ‡ were previously reported in Table 1 of [36]. The six solutions marked with M were obtained by the multiple-shooting Newton method of Appendix B.

Solution	$\bar{D}$	$\bar{c}$	d_U	$\mu^{\max}$	ω or θ	Solution	$\bar{D}$	$\bar{c}$	d_U	$\mu^{\max}$	ω or θ
$\mathrm{TW}_{N4L/1.38}$‡	1.38	1.238	3	0.1809	0.0	$\mathrm{TW}_{1.578}$	1.578	1.108	9	0.2877	0.0
$\mathrm{TW}_{2.039}$‡	2.039	1.091	7	0.1159	0.0	$\mathrm{TW}_{1.845}$	1.845	1.039	11	0.5166	0.891
$\mathrm{TW}_{1.968}$‡	1.968	1.105	9	0.1549	0.259	$\mathrm{TW}_{1.783}$	1.783	1.035	8	0.323	1.119
$\mathrm{TW}_{1.885}$	1.885	1.073	8	0.4568	0.206	$\mathrm{TW}_{2.041}$‡	2.041	1.095	8	0.1608	0.0
$\mathrm{TW}_{N4U/3.28}$‡	3.279	1.051	30	0.9932	1.89	$\mathrm{TW}_{1.926}$	1.926	1.096	8	0.2504	0.414
$\mathrm{RPO}_{F/6.668}$‡	1.805	1.12	3	0.0534	1.69	$\mathrm{RPO}_{F/M/33.81}$	1.805	1.128	5	0.0471	1.727
$\mathrm{RPO}_{F/13.195}$‡	1.839	1.117	5	0.0581	2.038	$\mathrm{RPO}_{F/33.968}$	1.806	1.127	5	0.0588	1.671
$\mathrm{RPO}_{F/20.427}$‡	1.809	1.128	5	0.0771	0.0	$\mathrm{RPO}_{F/40.609}$	1.814	1.125	5	0.0505	0.315
$\mathrm{RPO}_{F/26.861}$	1.84	1.121	5	0.0679	π	$\mathrm{RPO}_{F/M/47.449}$	1.826	1.126	5	0.0586	π
$\mathrm{RPO}_{F/26.964}$	1.826	1.124	6	0.0493	0.986	$\mathrm{RPO}_{F/M/53.876}$	1.83	1.124	6	0.0457	1.253
$\mathrm{RPO}_{F/27.299}$‡	1.815	1.126	4	0.0678	0.961	$\mathrm{RPO}_{F/M/67.936}$	1.806	1.128	5	0.0587	2.945
$\mathrm{RPO}_{4.954}$‡	2.015	1.084	3	0.1509	1.643	$\mathrm{RPO}_{M/14.544}$	2.015	1.102	6	0.1846	0.0
$\mathrm{RPO}_{5.468}$	2.003	1.091	6	0.1452	1.351	$\mathrm{RPO}_{M/14.646}$	1.776	1.133	5	0.1473	π
$\mathrm{RPO}_{6.119}$	1.875	1.081	7	0.1912	0.0	$\mathrm{RPO}_{14.961}$	1.945	1.114	5	0.1915	0.878
$\mathrm{RPO}_{6.134}$	1.86	1.086	7	0.1596	0.0	$\mathrm{RPO}_{15.081}$	2.06	1.081	8	0.1392	0.0
$\mathrm{RPO}_{6.18}$	1.865	1.091	5	0.211	0.0	$\mathrm{RPO}_{15.46}$‡	1.781	1.146	7	0.1166	0.0
$\mathrm{RPO}_{6.359}$	1.769	1.054	11	0.2614	0.0	$\mathrm{RPO}_{15.798}$	1.869	1.125	6	0.1089	π
$\mathrm{RPO}_{6.458}$	2.117	1.074	7	0.2055	0.0	$\mathrm{RPO}_{15.915}$	1.951	1.106	8	0.1547	π
$\mathrm{RPO}_{7.246}$	1.982	1.105	5	0.209	0.0	$\mathrm{RPO}_{15.972}$	1.956	1.097	7	0.1473	π
$\mathrm{RPO}_{7.272}$	2.015	1.1	5	0.1852	0.0	$\mathrm{RPO}_{16.271}$	1.978	1.09	7	0.1454	1.977
$\mathrm{RPO}_{7.423}$‡	1.838	1.109	6	0.1195	0.387	$\mathrm{RPO}_{16.878}$	1.969	1.099	5	0.1219	π
$\mathrm{RPO}_{7.741}$‡	1.707	1.138	5	0.0983	0.0	$\mathrm{RPO}_{17.21}$	1.999	1.098	7	0.1523	π
$\mathrm{RPO}_{9.735}$‡	2.05	1.086	7	0.1872	π	$\mathrm{RPO}_{17.46}$‡	1.917	1.121	6	0.0842	0.205
$\mathrm{RPO}_{11.696}$	1.961	1.108	9	0.1129	π	$\mathrm{RPO}_{21.704}$	1.868	1.12	7	0.0951	π
$\mathrm{RPO}_{12.026}$	2.09	1.088	6	0.1476	0.0	$\mathrm{RPO}_{22.063}$	2.032	1.101	7	0.1352	1.723
$\mathrm{RPO}_{12.566}$	2.053	1.083	10	0.1677	π	$\mathrm{RPO}_{23.047}$	1.874	1.12	6	0.1848	0.0
$\mathrm{RPO}_{12.706}$	2.156	1.07	6	0.1692	1.083	$\mathrm{RPO}_{23.356}$‡	1.98	1.112	6	0.101	1.249
$\mathrm{RPO}_{13.592}$	1.987	1.099	7	0.1072	0.0	$\mathrm{RPO}_{26.049}$	2.028	1.097	8	0.1635	π
$\mathrm{RPO}_{14.045}$‡	1.903	1.107	6	0.1403	π	$\mathrm{RPO}_{27.238}$	1.992	1.098	8	0.1258	0.0

CHAPTER 5
PERIODIC SOLUTIONS AND CHAOS IN THE BARKLEY PIPE MODEL ON A FINITE DOMAIN

5.1 Abstract

Barkley's bipartite pipe model is a continuous two-state reaction-diffusion system that models the transition to turbulence in pipes, and reproduces many qualitative features of puffs and slugs, localized turbulent structures seen during the transition. Extensions to the continuous model, including the incorporation of time delays and constraining the system to finite open domains—a trigger for convective instability—reveal additional solutions to the system, including periodic solutions and chaos unseen in the original $1+1$ dimensional system. It is found that the nature of solutions depends strongly on the size of the domain under study as well as choice of boundary conditions: on a finite domain for a particular window of parameter space, period-doubling and chaos are observed.

5.2 Introduction

The subcritical transition to turbulence in canonical fluid flows sees two different behaviors at two different scales: fast turbulent (chaotic) fluctuations on a small spatial scale and long-lived alternating laminar-turbulent patches on a larger spatial scale (spatiotemporal intermittency). Recent results suggest that transitional turbulence is a chaotic transient with a superexponential distribution of lifetimes[88][89] consistent with the dynamical systems view of transient turbulence arising from a chaotic saddle in state space[59][89][90][91][92]. As the laminar solution for plane Couette flow is known to be linearly stable for all Reynolds numbers[93]—and numerical and experimental evidence suggests that this is likewise true for pipe[7][17][94]—the emergence of transient chaos (transient turbulence) must derive

from a mechanism other than perturbation of the laminar flow[89]. For example, the following hypothesized chain of events can lead to the formation of a chaotic saddle that could sustain transient turbulence: Two steady states are created in a saddle node bifurcation. Linear stability analysis shows that the upper branch state is initially linearly stable. Next, a stable periodic orbit is created at a Hopf bifurcation. Eventually the orbit undergoes a period-doubling cascade and a chaotic attractor emerges. A boundary crisis destroys the attractor, after which it becomes a chaotic saddle that supports transient turbulence[90].

On a spatial scale much larger than that of chaotic fluctuations, the transition in pipe sees large-scale spatially intermittent *puffs* and *slugs*—localized turbulent structures—coexisting with quiescent background (laminar) flow[7]. Paradigmatic two-dimensional flows see localized structures analogous to those in pipe: regular spiral bands are observed in Taylor-Couette flows[26], and turbulent spot and stripe phases coexisting with a laminar background in plane Couette[28][35], forming Turing-like patterns evocative of those seen in Swift-Hohenberg and in several two-dimensional reaction-diffusion-advection systems. Manneville postulated that patterns observed in plane Couette flow, in particular, derive from a Turing instability, and remarks generally "[p]attern formation is indeed often an obliged stage in the transition to turbulence"[95].

Spatiotemporal patterns in fluid systems could result from Turing or Turing-Hopf instabilities. Barkley[3] proposed a minimal pipe model that reproduces many of the key features of puffs and slugs seen in numerical simulations and in experiments. Barkley's original model consists of two parts, each part addressing one of the two scales. First is a continuous reaction-diffusion model described by two coupled partial differential equations whose dynamics we explore in this paper in hopes of identifying a tell-tale pattern-forming instability. The complement to the continuous system is a discrete model with a chaotic map that is invoked in the excited regime of parameter space to mimic the small-scale chaotic fluctuations seen in experiments and direction numerical simulations (DNS); a later version of the model replaces the discrete chaotic map with a continuous additive

Gaussian noise[96]. Though Barkley's model is successful in predicting the transition to turbulence, it either invokes a discrete chaotic map to produce the requisite chaos[3] or introduces stochasticity to supply small-scale random fluctuations[96]. The success of the model, as well as its relative accessibility, compels further investigation.

In this paper, we show that chaos—including a route to chaos akin to that described in [90]—can be triggered in Barkley's continuous model with the inclusion of a small time delay and/or confining the dynamics to a finite open domain without need to resort to a complementary [chaotic] tent map. Additional new solutions emerge at a Hopf bifurcation to give rise to time-periodic states unseen in Barkley's original model. Further, it is argued that extending the model to two spatial dimensions (with zero flux BC on the other dimension) should lead to stripes and spots, the hallmark Turing patterns seen in $2D$ systems.

5.2.1 Models

Barkley's original continuous pipe model is

$$\begin{aligned} \frac{\partial q}{\partial t} + \overline{U}\frac{\partial q}{\partial z} &= q[u + r - 1 - (r+\delta)(q-1)^2] + \frac{\partial^2 q}{\partial z^2} + \eta q \sigma \\ \frac{\partial u}{\partial t} + \overline{U}\frac{\partial u}{\partial z} &= \epsilon_1(1-u) - \epsilon_2 u q - \frac{\partial u}{\partial z} \end{aligned}$$

where q is turbulence intensity and $u \in [0,1]$ is the centerline velocity along the pipe axis $\hat{z}$ relative to the mean axial speed of the bulk $\overline{U}$. The η term is the adjunct Gaussian white noise introduced in [96] and σ the noise strength. The parameter r is analogous to the Reynolds number seen in the nondimensionalized Navier-Stokes equations.

In this paper, we follow Barkley's lead and transform to the $\overline{U} = 0$ frame that co-moves with the steady bulk flow and replace the additive noise with fast dynamics h so that the

system under study is

$$\begin{aligned}
\frac{\partial q_{MF}}{dt} &= f(q(t), q(t-\tau), u(t), u(t-\tau)) + \frac{\partial q(x,t)}{\partial z^2} \\
\frac{\partial u_{MF}}{dt} &= g(q(t), q(t-\tau), u(t), u(t-\tau)) - \frac{\partial u(x,t)}{\partial z} \\
\frac{\partial h}{\partial t} &= [\text{fast dynamics}]
\end{aligned} \tag{5.1}$$

where

$$\begin{aligned}
f &= f(q(t), q(t-\tau), u(t), u(t-\tau)) \\
&= q[u_\tau + r - 1 - (r+\delta)(q-1)^2] + \epsilon h \\
g &= g(q(t), q(t-\tau), u(t), u(t-\tau)) \\
&= \epsilon_1(1-u) - \epsilon_2 u q_\tau
\end{aligned} \tag{5.2}$$

Here q_{MF} and u_{MF} are regarded as time-averaged mean field variables operating on a slow timescale, h as small-scale deviations from the mean field whose dynamics occur on a faster timescale, and τ is the time delay—which may or may not be set to zero—so that $q_\tau = q(t-\tau)$ and $u_\tau = u(t-\tau)$. Focus is given to the large-scale behavior of q and u; consequently, we will set $h = 0$ and postpone fast timescale dynamics until the Discussion section.

The paper is organized as follows: Numerical procedure; general results, including a discussion of the new periodic and chaotic solutions; a discussion of timescales in relation to percolation dynamics and the possibility of pattern-forming bifurcation in $2D$.

5.2.2 Numerical Procedure

For $z \in (0, N)$, the system under study is

$$\begin{aligned} \frac{dq}{dt} &= f(q(t), q(t-\tau), u(t), u(t-\tau)) + \frac{\partial^2 q(x,t)}{\partial z^2} \\ \frac{du}{dt} &= g(q(t), q(t-\tau), u(t), u(t-\tau)) - \frac{\partial u(x,t)}{\partial z} \\ \frac{\partial h}{\partial t} &= 0 \end{aligned} \tag{5.3}$$

initialized with

$$\left.\begin{aligned} q_o(\phi) &= \phi(\theta) \\ u_o(\psi) &= \psi(\theta) \end{aligned}\right\} \text{ for } \quad \theta \in [-\tau, 0] \tag{5.4}$$

The dynamics are confined to a finite computational domain described by boundary conditions,

$$\left.\begin{aligned} q(0,t) &= q(N,t) = 0 \\ u(0,t) &= u(N,t) + q(N,t) \end{aligned}\right\} \text{ for } t \in [0, T] \tag{5.5}$$

henceforth referred to as the smooth-inlet boundary conditions (SIBC).

Finite-difference method with $N \in (50, 1000)$, where N is the number of spatial grid points in the domain, taken to be the length of the pipe under consideration, with spatial grid size $\Delta z = 0.2$. Time steps of $\Delta t = 0.05$ are default, but larger (e.g., $\Delta t = 0.1$) and smaller (e.g., $\Delta t = 0.025$) time steps were taken, too, as a check of the stability of the code. The linear portion of equations is solved implicitly to ensure numerical stability; the nonlinear portion is solved explicitly with Courant number $C < 1$. To accommodate a nonzero time delay $\tau \neq 0$, the system was solved at $t - \tau$ and the unphysical solutions found for $t < 0$ were discarded.

Stability of code was checked by 1) varying Δt and Δz and observing consistent be-

haviors with no amplification or waves; 2) comparing SIBC in long pipe against periodic boundary conditions (PBC); it is observed that SIBC $\rightarrow$ PBC solutions for long enough domain; and 3) comparing solutions early in the time evolution before boundary is encountered. As $N \rightarrow \infty$, periodic solutions destabilize and asymptotically approach the solutions seen in Barkley's original PDE model.

Smooth-inlet boundary conditions (SIBC) described in Eq. 5.5 were introduced as a proxy for constant mass flux boundary conditions in finite open pipe used in DNS and generated in laboratory settings: all flux leaving the domain, regardless of being in state q or u is matched with an equal flux entering the domain as smooth flow u.

Parameter values $\epsilon_1 = 0.04$, $\epsilon_2 = 0.2$ and $\delta = 0.1$ are the same as those used by Barkley[3] and are fixed throughout. The parameter r is generally unrestricted, but focus is on the region of parameter space $0.7 \leq r \leq 1$.

5.3 Results

The role of disturbances in the inlet of the simulated pipe was the motivation for the particular type of boundary condition used in this study. Smooth inlet boundary conditions (SIBC) were used here because it was felt they were truer to real pipes than periodic boundary conditions. Since intermittency depends on inlet conditions even in very long pipes[10], experimentalists aim for smooth flow in the entrance of the pipe so that the size of any perturbation can be known and controlled[7][88]. Further, real pipes are finite in length; fluid, be it turbulent or laminar, must advect out of the open end of a real pipe eventually. In a sense, the SIBC is a kind of model in and of itself, aiming to reflect pipe flows in real laboratory conditions.

While invoking SIBC, it is observed that solutions depend strongly on the length of the numerical domain N, in addition to the parameters r and τ. As the domain size N impacts the nature of the solutions, it may be treated as an implicit bifurcation parameter (see [97] for a treatment of domain length as an explicit bifurcation parameter). Thus the variable

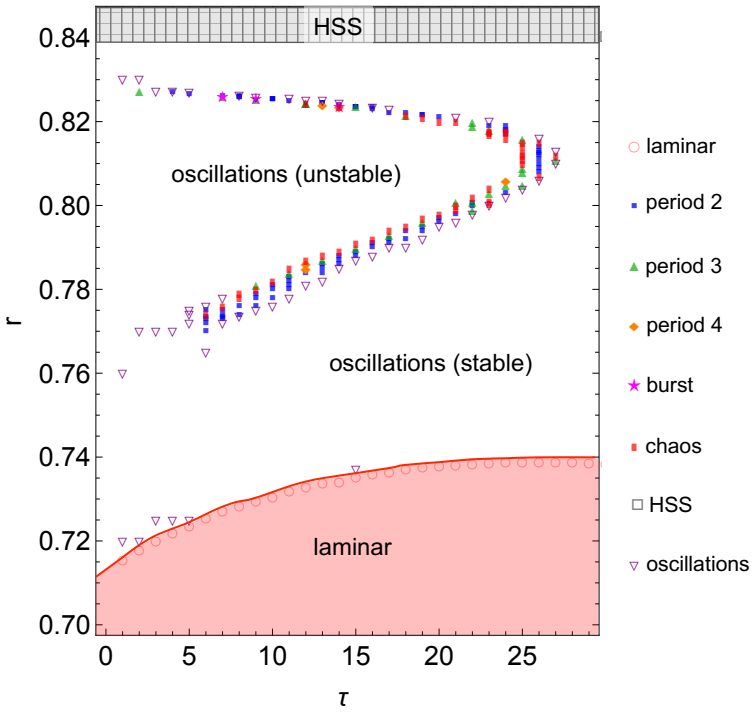

Figure 5.1: Solution space at $N = 140$ as a function of time delay τ and r. In this length of domain a variety of solutions is observed. A Hopf bifurcation first occurs in the undelayed system near $(\tau, r) = (0, 0.71)$; with increasing τ, the Hopf bifurcation occurs at increasing values of r, establishing a curve that defines the critical value τ_c above which periodic solutions are observed. Near $r = 0.839$, independent of τ, a final saddle-node bifurcation takes place whereby periodic solutions are destroyed and a homogeneous steady state (HSS) emerges.

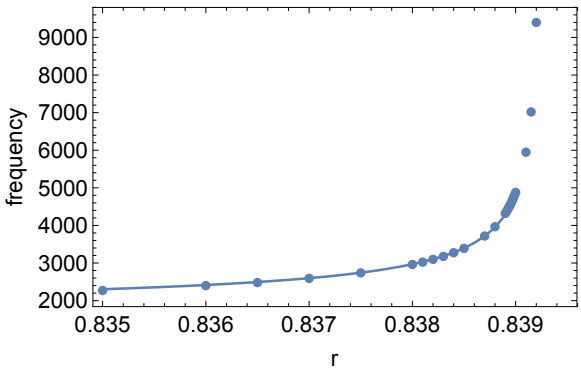

Figure 5.2: Near the saddle-node bifurcation at $r_c \approx 0.839$, the frequencies of oscillation for q increase in accordance with the universal inverse square-root scaling law for saddle-node bifurcations. Shown is the best fit curve frequency $= a + b(r_c - r)^{-0.501}$, where $a = 1520$ and $b = 50.6$. This figure was drawn using data from $N = 500$.

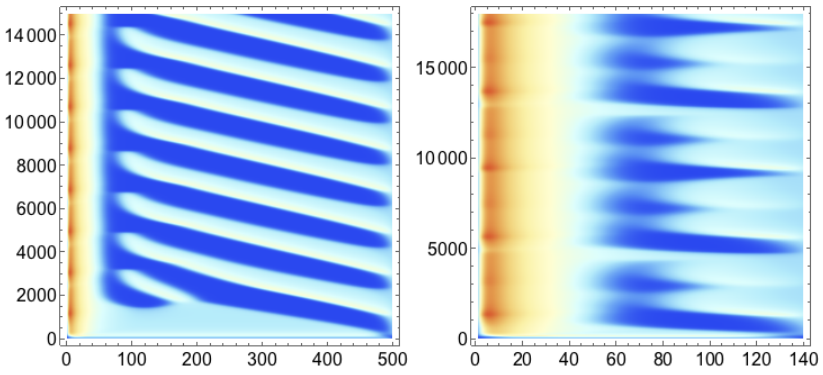

Figure 5.3: Spacetime evolution of $q(z,t)$ in the $\overline{U} = 0$ co-moving frame with the spatial variable z on the horizontal axis and time t on the vertical. The inlet of the pipe ($z \sim 0$) can show relatively large initial turbulent transients. (a) Periodic solutions at $r = 0.8274$, $N = 500$, $\tau = 0$. In a shorter domain, these same parameters see canards (see Fig. 5.8). (b) A chaotic trajectory at $r = 0.79$, $N = 143$, $\tau = 2$.

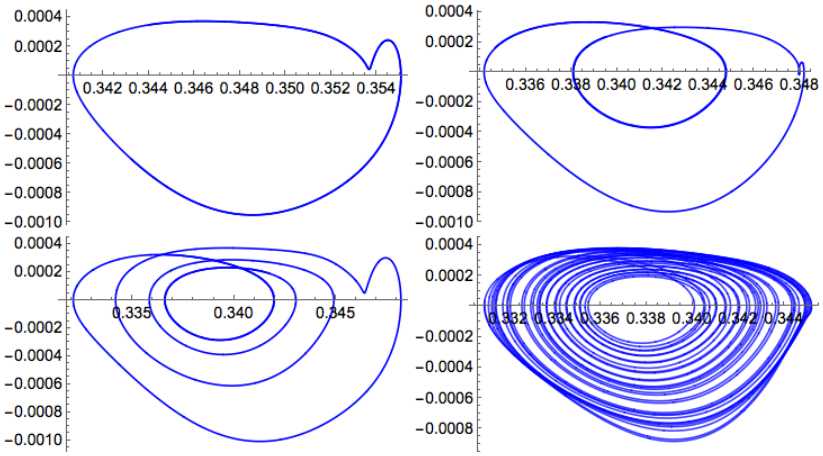

Figure 5.4: Period-doubling route to chaos demonstrated in phase space with u on the horizontal axis and $\dot{u}$ on the vertical. $N = 142$, $\tau = 7$, and (a) $r = 0.780$; (b) $r = 0.787$; (c) $r = 0.789$; and (d) $r = 0.79035$.

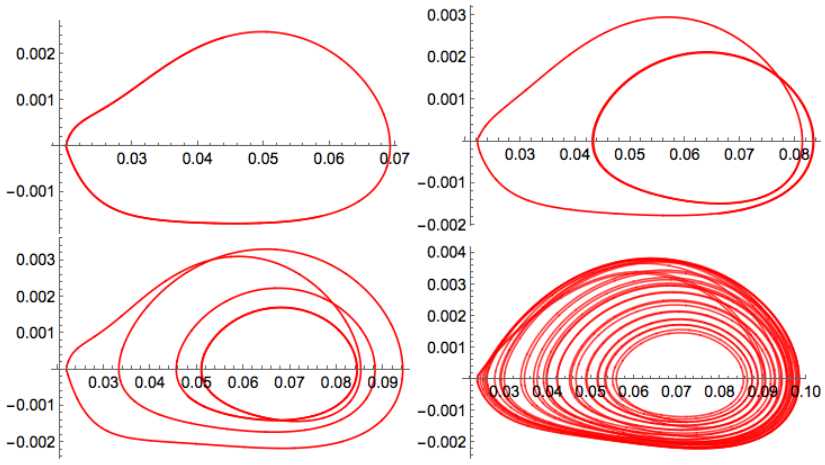

Figure 5.5: Period-doubling route to chaos demonstrated in phase space, with q on the horizontal axis and $\dot{q}$ on the vertical. $N = 142$, $\tau = 7$, and (a) $r = 0.780$; (b) $r = 0.787$; (c) $r = 0.789$; and (d) $r = 0.79035$.

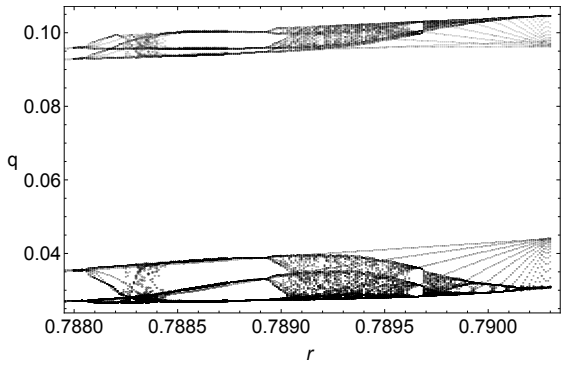

Figure 5.6: Bifurcation diagram for the strongly chaotic region at $N = 140$ and initial conditions are $q(t = 0) = 0.70$.

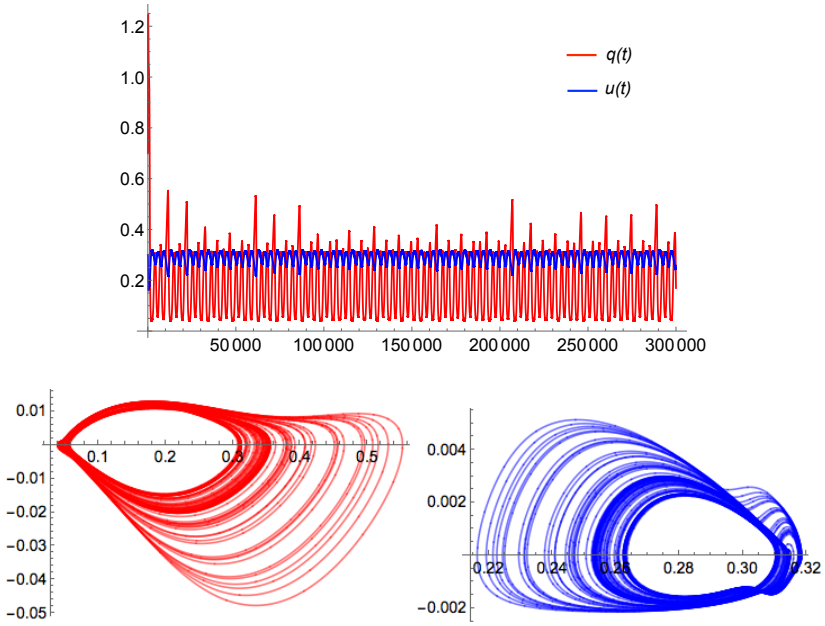

Figure 5.7: TOP: A chaotic time series at $r = 0.8176$ and $\tau = 45$. Bottom: Phase portraits. q (red, bottom left) and u (blue, bottom right).

bifurcation parameters are $r(N)$ and $\tau(N)$. Houghton and Knobloch [98] discussed the role of boundary conditions in the Swift-Hohenberg equation subjected to finite domains: the system admits spatially periodic structures when subject to periodic boundary conditions (PBC), but sees large amplitude filling states when Neumann boundary conditions are imposed. The SIBC used here may be regarded as a hybrid of the two: absorbing for $q(z = N)$, periodic with an additional source for $u(z = 0)$.

With time delay and SIBC incorporated into Barkley's model, chaos is seen in a range of domain lengths at differing values of time delays—or, in the case of $N \approx 150$, at zero time delay—suggesting that the length of the domain plays a larger role in the observed solutions than does time delay. Fig. 5.1 demonstrates the solutions that emerge at one set of parameters. For domains $N \approx 150$, a route to chaos follows a sequence of events remarkably similar to those thought to lead to transient turbulence in pipe[90]: Two coexisting steady states—a trivial "laminar" steady state with $q \to 0, u \to 1$, and a nontrivial excited steady state with $q \neq 0, u \neq 1$—are created at a saddle node bifurcation; the value of r for which this occurs depends on the amount of q introduced into the inlet of the system in analogy

to a minimum perturbation amplitude required to transition from laminar flow[99]. Next, a Hopf bifurcation leads to sustained oscillations between the two coexisting steady states; no further perturbation or triggering beyond the initial condition are required to sustain the oscillations. These periodic solutions are not observed in Barkley's original system. With increasing r and N, the amplitude of the stable limit cycles grows. Eventually, the periodic orbits undergo a period-doubling cascade (Figs. 5.4 and 5.5), followed by the emergence of a chaotic attractor (Fig. 5.6). With increasing r the chaotic structure disappears, and the stable periodic solutions give way to unstable periodic orbits that asymptotically decay to a non-laminar steady state. As r is further increased for $N \sim 140$, chaos re-emerges, this time accompanied by canard explosions ("bursts")—jumps from localized- to globally-turbulent solutions that rapidly, but briefly, fill the whole domain—solutions unseen in the chaotic region at lower r (See Fig. 5.8). Beyond this, large amplitude oscillations are observed until the system undergoes another saddle-node bifurcation at $r \sim 0.839$ for all values of N studied, in agreement with Barkley's observation that the system undergoes a change somewhere between $r = 0.823$ and $r = 0.85$. Here, all periodic states are destroyed and only two homogeneous steady states—the trivial laminar and a large amplitude q steady state—remain. This regime is bistable and is identified with spreading puffs and global turbulence. The destruction of all stable periodic solutions occurs with the onset of the final saddle-node bifurcation. Beyond this point, the amplitude of q drops sharply before increasing again. Just before this final saddle-node bifurcation, the frequencies of the limit cycles approaches a "bottleneck", leading to increasing oscillation frequencies as the saddle-node bifurcation is approached[100]. We observe the universal inverse square root scaling law is obeyed, confirming the saddle-node bifurcation at $r = 0.839$ (Fig. 5.2).

All four behaviors—the two homogeneous steady states (HSS), and decaying and sustained oscillations—may be accompanied by initial transients. Long chaotic transients are most likely to be seen in the region between sustained oscillations and the slug HSS for $r \gtrsim 0.84$. These four behaviors are seen elsewhere, for example, by Vanag and Ep-

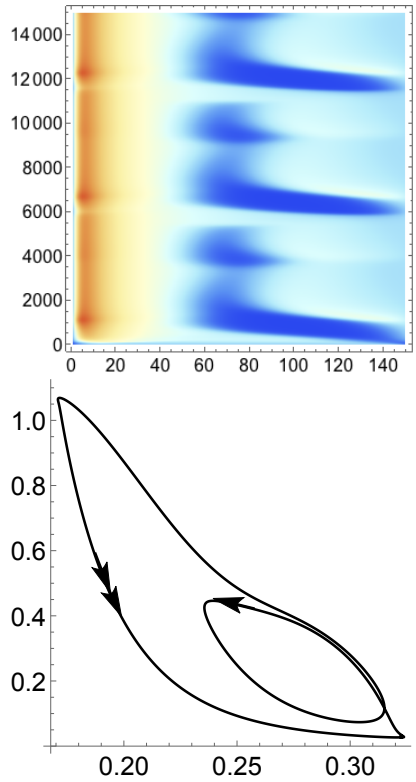

Figure 5.8: Coexistence of small- and large-amplitude solutions at $r = 0.8274$, $N = 150$, $\tau = 0$. Canard behavior is observed when a trajectory, initially following the small-amplitude limit cycle, undergoes a fast excursion to the large-amplitude limit cycle before returning to the original orbit. (a) The spacetime evolution of $q(z,t)$; and the (b) phase space diagrams of $(u, \dot{u})$ (top) and $(q, \dot{q})$ (bottom) during the canard cycle. (c) A canard cycle in (u, q) space demonstrating orbits around the small-amplitude limit cycle with a quick excursion to a large-amplitude relaxation cycle. The small-amplitude limit cycle is destroyed at the saddle-node bifurcation at $r \approx 0.839$.

stein[101]. This isn't too surprising given that Barkley's system, like Vanag and Epstein's, is a modified reaction-diffusion system. Further, as $2D$ reaction-diffusion systems often give rise to striping and other pattern formations, we suspect that Barkley's model can be extended to two spatial dimensions to model transitional stripe-like structures seen in plane Couette and plane Poiseuille flows[102].

5.3.1 Periodic Solutions

With SIBC, the modified Barkley model undergoes a Hopf bifurcation in every finite domain studied. Smaller domains (e.g., $N \sim 140$) see two sets of periodic solutions: a small-

amplitude limit cycle at smaller r that eventually undergoes a period-doubling cascade and chaos, and a larger-amplitude limit cycle at larger r. Large domains (e.g., $N > 300$) see large-amplitude limit cycles very soon after the initial saddle-node bifurcation and only transient chaos. These "pulsating"[103] or "breathing" solutions are seen in domains with and without time delays, including $N = 1000$, the largest domain studied here, and are reminiscent of breathing spots seen in 2D reaction-diffusion systems[104]. As $N \to \infty$, the periodic solutions grow unstable and we recover the asymptotic steady state solutions reported by Barkley[3].

The role of time delays in triggering Hopf bifurcations in $1+$ D-dimensional systems, and Turing-Hopf transitions in $2D$ reaction-diffusion-advection systems, has been studied previously. For example, Sen *et al.*[105] investigated the effect of small time delays in a pigmentation fish model and the CDIMA system, and Zhang and Zang[106] analyzed large delays in the extended Rosenzweig and MacArthur model with zero flux boundary conditions. Both groups observed a critical value of τ for the emergence of sustained Turing patterns. We make similar observations: there is a critical time delay τ_c above which instability sets in and below which the homogeneous steady states remain stable and no oscillations are observed. See Fig. 5.1.

5.3.2 Chaos

For finite domains subjected to SIBC, two sets of time-periodic solutions may be seen: a small-amplitude limit cycle (stable at lower r and N, unstable at larger r and N) and a large-amplitude limit cycle (unstable at small r and N). The former sees long-lived chaos, as well as chaotic transients, while the latter sees only chaotic transients, at least for the values of N and τ investigated in this paper. A period-doubling cascade and chaos is first encountered when a fixed-point solution collides with the small-amplitude periodic orbits, e.g., the onset of chaos near $r \approx 0.7873$, and $\tau = 14$ for $N = 140$ (Fig. 5.7). The crisis destabilizes the small-amplitude orbits and the now-unstable periodic solutions decay

asymptotically towards a non-laminar steady state (however, at other values of N, chaos may still be observed at the same value of τ and r). As r increases further, another round of period-doubling and chaos takes place. Interestingly, this time the chaotic solutions include canards and large-amplitude chaotic bursts—jumps from locally- to globally-turbulent solutions that rapidly, but briefly, fill the whole spatial domain, perhaps analogous to random puff splitting events seen in pipe—solutions unseen in the earlier chaotic region at lower r. Other chaotic trajectories include visits to both coexisting orbits (see Fig. 5.8) and mixed-mode oscillations. Soon after, the small-amplitude limit cycles are destroyed, while the large-amplitude limit cycles stabilize. Consequently, the bifurcation diagram shows an abrupt jump to large-amplitude periodic orbits.

We note that the chaos described here is independent of any *ad hoc* chaotic tent maps; any fast time-scale dynamics $h(t)$ superimposed or added to the system, including small-scale deviations from the mean-field values of q and u, will fluctuate chaotically due to the the chaos of the underlying slow system regardless if the fast dynamics described by $h(t)$ are chaotic or not.

5.4 Discussion

The initial focus of this investigation was to understand the circumstances under which a pattern-forming instability and/or chaos could appear in Barkley's model, including the roles of boundary conditions and time delays known to affect pattern formation in other reaction-diffusion systems.

Pipe flow, like the Barkley model subject to the boundary conditions discussed in this paper, is an open system, and issues related to convective instability must be raised, including the possible presence of noise-sustained structures and concomitant spatiotemporal intermittency. For example, the transition from convective instability to absolute instability with increasing Reynolds number describes a mechanism by which a localized puff can become a spreading slug. As Deissler notes, any open system with nonzero group velocity

will be convectively unstable for some range of parameters[19]. Above the onset of an instability the upstream and downstream front speeds of the localized perturbation will have the same sign as the group velocity and a turbulent patch ("puff") will advect down the pipe, growing in the co-moving frame of reference $\overline{U} = 0$.

Further, the open system can grow convectively chaotic, leading to the spreading of the turbulent structure ("slug"). For example, in the Ginzburg-Landau equation, when the amplitude of a perturbation near the fronts grows sufficiently large ("pops" into the chaotic basin of attraction), the slug will spread randomly in time. As the convectively chaotic fluctuations are effectively random, the information describing spreading slugs must be considered in the aggregate. Barkley *et al.* make an accordant observation of their data that the "bifurcation scenario predicted by the model is only recovered in average quantities."[8] Barkley *et al.* acknowledge that the models—both the original form here as well as the amended form—fail to capture the stochastic fluctuations in the downstream front as well as the spatiotemporal intermittency in the whole of the domain ("intermittent laminar pockets"). Intermittency, too, can be ascribed to noisy fluctuations in convectively unstable systems, as noted by Deissler in an earlier paper[18].

Convectively unstable systems are especially sensitive to noise, and even small fluctuations can trigger large amplitude spatiotemporally-varying structures and pattern formation in the whole domain[19]. Stochasticity—the random small scale variations that fluctuate the puffs, slugs, and their laminar-turbulent fronts—must be inserted into Barkley's model as an additional component operating at a faster timescale than q and u, but it is precisely these faster, smaller amplitude fluctuations that a convectively unstable system is sensitive to. Mullin, citing Waleffe[107], notes in his review that pipe flow becomes more sensitive to background disturbances as Reynolds number increases. Specifically, for a finite perturbation of amplitude ϵ, the minimum amplitude required to trigger turbulence scales with

Reynolds number according to,

$$\epsilon = \mathcal{O}(Re^{\gamma}) \tag{5.6}$$

as $Re \to \infty$ and $\gamma < 0$; that is, turbulence can be triggered with smaller and smaller amplitude disturbances as Reynolds number increases[7].

One approach proposed to describing small scale fluctuations $h(z,t)$ treats a turbulent patch—a puff or slug—as a directed percolation field. Experimental studies of the transition to sustained turbulence in Couette flow and in Waleffe flow was found to be consistent with a directed percolation process[108], and it is speculated that pipe flow, too, would fall into the directed percolation universality class[109]. With the directed percolation rules shown in Fig. 5.9 the resulting mean field equation for the percolating cluster is

$$\frac{\partial q_{MF}}{\partial t} \sim (\lambda(Re) - \gamma)q - (k + \lambda(Re))\, q^2 + D_z \frac{\partial^2 q}{\partial z^2} \tag{5.7}$$

where a generic mean-field expression for q may be written down by balancing diffusion (with streamwise-directed diffusion coefficient D_z) the turbulence coagulation rate k, the reproduction/branching rate λ, and the $q \to u$ turbulent decay rate γ. Small fluctuations about q_{MF} would map to the faster, small-scale dynamics $h(z,t)$ in Eq. 5.1.

The appearance of the diffusion term in the percolation process is notable. (Barkley's original model neglected diffusion, effectively leaving $D_z = 1$, but his amended model incorporates a nonunit diffusion coefficient, e.g. $D_z = 0.13$[8].) In general, the diffusive term inhibits short-wavelength perturbations; however, expanding the system to additional spatial dimensions may introduce pattern-forming instabilities, including diffusion-driven instability (Turing instability). In two dimensions with the bulk of the flow moving in the streamwise direction z and no net flow in the spanwise direction x, the two diffusivities would vary, with the D_z showing a streamwise bias and D_x without, setting up a situation

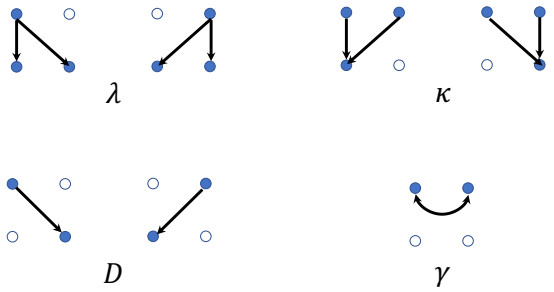

Figure 5.9: Nearest-neighbor reaction-diffusion dynamics from time step t (top row) to $t + dt$ (bottom).

ideal for pattern formation in $2D$.

Diffusion through a percolating cluster, e.g. puff, differs from diffusion in a homogeneous medium. For a fractal cluster or otherwise disordered medium, diffusivity depends on distance from percolation threshold p_c. Above the threshold ($p > p_c$) the cluster is effectively homogeneous and diffusion is regular, i.e. follows Fick's law $\langle R^2(t)\rangle \sim t^{2/d_w}$ with diffusion exponent $d_w = 2$. At criticality ($p = p_c$) however, and the cluster is statistically self-similar at all length scales and the diffusion in anomalous with $d_w > 2$. Below criticality $p < p_c$ the clusters are of finite size on the order of the correlation length $\xi(p)$ so that with $\langle R(t)\rangle^2 \sim \xi^2(p)$ where $\langle R(t)\rangle^2$ is the mean-squared displacement as $t \to \infty$[110].

The percolation process here would be biased in the direction of the applied pressure gradient that is pushing the fluid through the pipe. There are two primary effects of this directional bias. Firstly, the diffusion might show a nonzero drift velocity relative to the bulk velocity $\overline{U}$ [110]. Secondly, the pressure gradient may "trap" turbulent structures q at the boundaries of the cluster. To expand the turbulent cluster, the fluid particle must overcome the energetic barrier associated with the pressure gradient; that is to say, the particle must meet or exceed an energetic threshold in order for the turbulent structure to spread. Thus the spreading of puffs can be connected to Barkley's $u \to q$ transition rate so that $\epsilon_2(r)q_\tau$ must be analogous to a "threshold for excitation" and further connected to Goldenfeld's extremal fluctuations[111]. Since ϵ_2 is a function of r (or, in the directed percolation picture, the branching rate depends on Reynolds number) the fraction of the

pipe filled with turbulence increases with Reynolds number. But percolation isn't the only mechanism by which the turbulent structures can spread; convectively chaotic structures spread randomly, too.

SIBC were used here because it was felt they were truer to real pipes than periodic boundary conditions. Since intermittency depends on inlet conditions even in very long pipes[10], experimentalists aim for smooth flow in the entrance of the pipe so that the size of any perturbation can be known and controlled[7][88]. Further, real pipes are finite in length; fluid, be it turbulent or laminar, must advect out of the open end of a real pipe eventually. In a sense, the SIBC is a kind of model in and of itself, aiming to reflect pipe flows in real laboratory conditions.

While implementing boundary conditions, both smooth inlet boundary conditions (to model finite pipes) and periodic boundary conditions (to model infinite pipe) were applied to see how solutions vary with finite domain size. When lengthening the domain while enforcing SIBC, we recover the solutions seen with periodic boundary conditions (PBC) and those found by Barkley. Consequently, one may view the new solutions—the time-periodic "pulsating" solutions and chaotic solutions, akin to [103]—to be additional sets of solutions seen in the limit of finite domains. That these time-periodic solutions grow unstable only at very large N suggests that SIBC induces a Hopf instability in the system, perhaps one that will interact with a Turing instability to bring about stripes in a two-dimensional extension of the model.

In addition, time-delayed coupling between u and q played less of a role in the set of observed solutions in this $1D$ model than did SIBC. However, the delay may play a bigger role in a two-dimensional extension of the model in accordance with literature on time delay-induced Turing instabilities. One may anticipate that an extension of the model to $2D$ will generate spots and stripes like those seen in plane Couette, and similar to those described by Manneville[95].

5.5 Summary

We were able to find previously-unknown periodic solutions and generate chaos in Barkley's pipe model with two physically-motivated modifications: admitting a time-delayed coupling between q and u, and by introducing SIBC.

CHAPTER 6
CONCLUSION

There remain several avenues of study with which to follow up on the work mentioned in this dissertation. For example, invariant solutions have shown themselves to be relevant to spatiotemporal intermittency at transitional Re, both numerically and experimentally, which suggests that a turbulence model or theory of traveling waves, periodic orbits, and relative periodic orbits could very well describe observations. However, whether that theory is Periodic Orbit Theory (POT) is not yet known; until a sufficiently large catalogue of solutions has been found, POT cannot be rigorously tested. Consequently, it is important to continue the search for invariant solutions until a sufficiently large number have been collected and the predictions of POT can be tested.

In addition to invariant solutions, the search for dynamically-relevant heteroclinic connections between invariant solutions is ongoing. For example, heteroclinic connections between lower-branch and upper-branch pairs of solutions have been computed for some range of Re but their existence is hardly surprising given their proximity in state space and the relatively small number of unstable eigenvectors at relatively low Re; whether these connections are relevant at higher Re or in domains with a greater number of solutions remains unknown. Moreover, heteroclinic connections between unrelated solutions— solutions not emerging from a common bifurcation—have not been found for fluid flows as far as this author is aware.

On the technical side, a machine learning or data-driven algorithm to find invariant solutions could theoretically be implemented, greatly increasing the rate at which invariant solutions is found. Less technically challenging would be the creation of a program that efficiently identifies candidate solutions from recurrence data for the Newton-Krylov algorithm.

Further, the pipe code used in this study could be modified to simulate a pipe with open boundary conditions and to see how disturbances in the inlet of the pipe evolve as a result of convective instability.

Regarding the role of invariant solutions in pattern formation: Can invariant solutions explain puff splitting, puff spreading, and puff-puff interaction? The recent work of Reetz *et al.*[31] suggests a possible course of investigation for pipe: continuation of a traveling wave solution that undergoes a pattern-forming bifurcation leading to a long wavelength modulation of the underlying periodic solution. Recently, I found a solution in a $55R$-long pipe whose unstable eigenvectors appear to possess a strong streamwise streak energy with a long-wavelength modulation. Whether a streamwise long-wavelength modulation explains the puff-laminar "pattern" in pipe may be observed with further continuation of this long-pipe solution into a yet longer pipe.

Among the most pressing question is the reason behind the spatio-temporally intermittency—the puff-laminar-puff-laminar—patterns observed in long pipes with a "preferred" spacing of $20D$ and how invariant solutions can explain this phenomenon. What are the important processes which allow a puff to adopt an equilibrium length but forces a slug to expand aggressively?

Extending Barkley's pipe model to two dimensions is the next step in understanding and testing the model. The model is successful in describing the onset of sustained turbulence in pipe; can it reproduce the observed patterns seen in two-dimensional canonical fluid systems like plane Couette and plane Poiseuille flow? And, importantly, can this model be derived from the Navier-Stokes equations or connected to a related equation?

Finally, one particular question that repeatedly popped up during the research was: Is Re the sole bifurcation parameter for pipe? Numerical continuation of invariant solutions finds that the nature of the solutions and the dynamics depends strongly on the length of the pipe. Perhaps pipe length L is a bifurcation parameter, too?

Appendices

APPENDIX A

LETTERS OF PERMISSION FOR USE OF COPYRIGHTED MATERIAL

CAMBRIDGE UNIVERSITY PRESS LICENSE
TERMS AND CONDITIONS

Oct 07, 2019

This Agreement between Georgia Institute of Technology -- Kimberly Short ("You") and Cambridge University Press ("Cambridge University Press") consists of your license details and the terms and conditions provided by Cambridge University Press and Copyright Clearance Center.

License Number	4683940376441
License date	Oct 07, 2019
Licensed Content Publisher	Cambridge University Press
Licensed Content Publication	The Journal of Fluid Mechanics
Licensed Content Title	Relative periodic orbits form the backbone of turbulent pipe flow
Licensed Content Author	N. B. Budanur, K. Y. Short, M. Farazmand, A. P. Willis, P. Cvitanović
Licensed Content Date	Nov 6, 2017
Licensed Content Volume	833
Licensed Content Issue	undefined
Start page	274
End page	301
Type of Use	Dissertation/Thesis
Requestor type	Author
Portion	Full article
Author of this Cambridge University Press article	Yes
Author / editor of the new work	Yes
Order reference number	na
Territory for reuse	North America Only
Title of your thesis / dissertation	Coherent Structures in Incompressible Fluid Flows
Expected completion date	Oct 2019
Estimated size(pages)	85
Requestor Location	Georgia Institute of Technology 1566 Runnymeade Rd NE ATLANTA, GA 30319 United States Attn: Kimberly Short
Publisher Tax ID	GB823847609
Total	0.00 USD
Terms and Conditions	

TERMS & CONDITIONS

American Physical Society
Reuse and Permissions License

07-Oct-2019

This license agreement between the American Physical Society ("APS") and Kimberly Short ("You") consists of your license details and the terms and conditions provided by the American Physical Society and SciPris.

Licensed Content Information

License Number:	**RNP/19/OCT/019285**
License date:	07-Oct-2019
DOI:	10.1103/PhysRevE.93.022204
Title:	Symmetry reduction in high dimensions, illustrated in a turbulent pipe
Author:	Ashley P. Willis, Kimberly Y. Short, and Predrag Cvitanović
Publication:	Physical Review E
Publisher:	American Physical Society
Cost:	USD $ 0.00

Request Details

Does your reuse require significant modifications: No

Specify intended distribution locations:	United States
Reuse Category:	Reuse in a thesis/dissertation
Requestor Type:	Author of requested content
Items for Reuse:	Whole Article
Format for Reuse:	Electronic

Information about New Publication:

University/Publisher:	Georgia Institute of Technology
Title of dissertation/thesis:	Coherent Structures in Incompressible Fluid Flows
Author(s):	Kimberly Yovel Short
Expected completion date:	Oct. 2019

License Requestor Information

Name:	Kimberly Short
Affiliation:	Individual
Email Id:	kyshort@gatech.edu
Country:	United States

American Physical Society
Reuse and Permissions License

TERMS AND CONDITIONS

The American Physical Society (APS) is pleased to grant the Requestor of this license a non-exclusive, non-transferable permission, limited to Electronic format, provided all criteria outlined below are followed.

1. You must also obtain permission from at least one of the lead authors for each separate work, if you haven't done so already. The author's name and affiliation can be found on the first page of the published Article.

2. For electronic format permissions, Requestor agrees to provide a hyperlink from the reprinted APS material using the source material's DOI on the web page where the work appears. The hyperlink should use the standard DOI resolution URL, http://dx.doi.org/{DOI}. The hyperlink may be embedded in the copyright credit line.

3. For print format permissions, Requestor agrees to print the required copyright credit line on the first page where the material appears: "Reprinted (abstract/excerpt/figure) with permission from [(FULL REFERENCE CITATION) as follows: Author's Names, APS Journal Title, Volume Number, Page Number and Year of Publication.] Copyright (YEAR) by the American Physical Society."

4. Permission granted in this license is for a one-time use and does not include permission for any future editions, updates, databases, formats or other matters. Permission must be sought for any additional use.

5. Use of the material does not and must not imply any endorsement by APS.

6. APS does not imply, purport or intend to grant permission to reuse materials to which it does not hold copyright. It is the requestor's sole responsibility to ensure the licensed material is original to APS and does not contain the copyright of another entity, and that the copyright notice of the figure, photograph, cover or table does not indicate it was reprinted by APS with permission from another source.

7. The permission granted herein is personal to the Requestor for the use specified and is not transferable or assignable without express written permission of APS. This license may not be amended except in writing by APS.

8. You may not alter, edit or modify the material in any manner.

9. You may translate the materials only when translation rights have been granted.

10. APS is not responsible for any errors or omissions due to translation.

11. You may not use the material for promotional, sales, advertising or marketing purposes.

12. The foregoing license shall not take effect unless and until APS or its agent, Aptara, receives payment in full in accordance with Aptara Billing and Payment Terms and Conditions, which are incorporated herein by reference.

13. Should the terms of this license be violated at any time, APS or Aptara may revoke the license with no refund to you and seek relief to the fullest extent of the laws of the USA. Official written notice will be made using the contact information provided with the permission request. Failure to receive such notice will not nullify revocation of the permission.

14. APS reserves all rights not specifically granted herein.

15. This document, including the Aptara Billing and Payment Terms and Conditions, shall be the entire agreement between the parties relating to the subject matter hereof.

American Physical Society
Reuse and Permissions License

07-Oct-2019

This license agreement between the American Physical Society ("APS") and Kimberly Short ("You") consists of your license details and the terms and conditions provided by the American Physical Society and SciPris.

Licensed Content Information

License Number:	**RNP/19/OCT/019286**
License date:	07-Oct-2019
DOI:	10.1103/PhysRevE.100.023116
Title:	Periodic solutions and chaos in the Barkley pipe model on a finite domain
Author:	K. Y. Short
Publication:	Physical Review E
Publisher:	American Physical Society
Cost:	USD $ 0.00

Request Details

Does your reuse require significant modifications: No

Specify intended distribution locations:	United States
Reuse Category:	Reuse in a thesis/dissertation
Requestor Type:	Author of requested content
Items for Reuse:	Whole Article
Format for Reuse:	Electronic

Information about New Publication:

University/Publisher:	Georgia Institute of Technology
Title of dissertation/thesis:	Coherent Structures in Incompressible Fluid Flows
Author(s):	Kimberly Yovel Short
Expected completion date:	Oct. 2019

License Requestor Information

Name:	Kimberly Short
Affiliation:	Individual
Email Id:	kyshort@gatech.edu
Country:	United States

American Physical Society
Reuse and Permissions License

TERMS AND CONDITIONS

The American Physical Society (APS) is pleased to grant the Requestor of this license a non-exclusive, non-transferable permission, limited to Electronic format, provided all criteria outlined below are followed.

1. You must also obtain permission from at least one of the lead authors for each separate work, if you haven't done so already. The author's name and affiliation can be found on the first page of the published Article.

2. For electronic format permissions, Requestor agrees to provide a hyperlink from the reprinted APS material using the source material's DOI on the web page where the work appears. The hyperlink should use the standard DOI resolution URL, http://dx.doi.org/{DOI}. The hyperlink may be embedded in the copyright credit line.

3. For print format permissions, Requestor agrees to print the required copyright credit line on the first page where the material appears: "Reprinted (abstract/excerpt/figure) with permission from [(FULL REFERENCE CITATION) as follows: Author's Names, APS Journal Title, Volume Number, Page Number and Year of Publication.] Copyright (YEAR) by the American Physical Society."

4. Permission granted in this license is for a one-time use and does not include permission for any future editions, updates, databases, formats or other matters. Permission must be sought for any additional use.

5. Use of the material does not and must not imply any endorsement by APS.

6. APS does not imply, purport or intend to grant permission to reuse materials to which it does not hold copyright. It is the requestor's sole responsibility to ensure the licensed material is original to APS and does not contain the copyright of another entity, and that the copyright notice of the figure, photograph, cover or table does not indicate it was reprinted by APS with permission from another source.

7. The permission granted herein is personal to the Requestor for the use specified and is not transferable or assignable without express written permission of APS. This license may not be amended except in writing by APS.

8. You may not alter, edit or modify the material in any manner.

9. You may translate the materials only when translation rights have been granted.

10. APS is not responsible for any errors or omissions due to translation.

11. You may not use the material for promotional, sales, advertising or marketing purposes.

12. The foregoing license shall not take effect unless and until APS or its agent, Aptara, receives payment in full in accordance with Aptara Billing and Payment Terms and Conditions, which are incorporated herein by reference.

13. Should the terms of this license be violated at any time, APS or Aptara may revoke the license with no refund to you and seek relief to the fullest extent of the laws of the USA. Official written notice will be made using the contact information provided with the permission request. Failure to receive such notice will not nullify revocation of the permission.

14. APS reserves all rights not specifically granted herein.

15. This document, including the Aptara Billing and Payment Terms and Conditions, shall be the entire agreement between the parties relating to the subject matter hereof.

APPENDIX B

MULTI-POINT SHOOTING

We used a multi-point shooting method in order to find some of the (relative) periodic orbits reported in § 4.5 (marked with subscript 'M' in Table 4.1). For simplicity, we explain the concept for periodic orbits. The approach is essentially the same for relative periodic orbits, once the drifts in the continuous symmetry group directions are accounted for.

Consider a state x_0 on a periodic orbit with period T, i.e.,

$$x_0 = f^T(x_0)\,.$$

The periodic orbits are found by searching for the period $T > 0$ and the state x_0 as the zeros of the nonlinear system of equations $x_0 - f^T(x_0) = 0$. We determine these zeros from a starting guess by Newton–GMRES–hook iterations [72].

By the semi-group property of the flow map f^t, we have $x_0 = f^T(x_0) = f^{t_2}(f^{t_1}(x_0))\,,$ for any $t_1, t_2 > 0$ such that $t_1 + t_2 = T$. Denoting the time-t_1 image of x_0 by $x_1 = f^{t_1}(x_0)$, the period closes in two steps

$$x_1 = f^{t_1}(x_0)\,, \qquad x_0 = f^{t_2}(a_1)\,.$$

The periodic orbit is then found through *two-point shooting* by searching for states x_0 and x_1 as well as the times t_1 and t_2 that satisfy

$$x_1 - f^{t_1}(x_0) = 0\,, \qquad x_0 - f^{t_2}(a_1) = 0\,.$$

The motivation for using the multi-point shooting is two-fold:

1. Let x_0 be a point on a periodic orbit with period T. In theory, we have $f^T(x_0) - x_0 =$

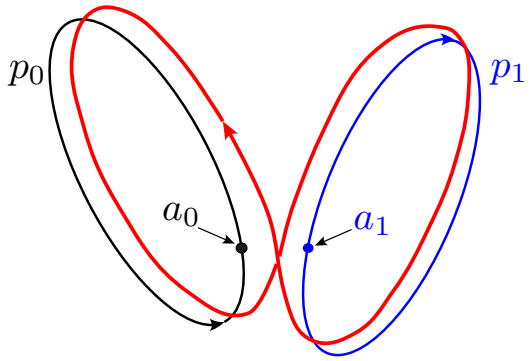

Figure B.1: An illustration of the multi-point shooting method. A long periodic orbit (red) is obtained from shorter periodic orbits p_0 (black) and p_1 (blue) with periods T_0 and T_1, respectively. Multi-point shooting attempts to find the shortest orbit that shadows both p_0 and p_1, with period T that is approximately the sum of the periods of the shorter orbits, $T \simeq T_0 + T_1$.

0. In practice, x_0 is never known exactly and only a numerical approximation of it is available. If the periodic orbit is highly unstable, the initial discrepancy grows over time to such extent that the state $f^T(x_0)$ might land far away from x_0. By partitioning the orbit into shorter segments, the error growth is kept under control.

2. Multi-point shooting offers a systematic way to create long orbits by "glueing" the already known shorter orbits[66]. Let p_0 and p_1 denote two short periodic orbits with periods T_0 and T_1, respectively (see figure B.1). The initial guesses for x_0 and x_1 are chosen to belong to the shorter orbits, i.e., $x_0 \in p_0$ and $x_1 \in p_1$. The initial guesses for the flight times t_1 and t_2 are chosen to coincide with the period of the short orbits, i.e., $t_1 = T_0$ and $t_2 = T_1$. If the Newton–GMRES–hook steps converge, the resulting orbit shadows the short periodic orbits and has a period $T \simeq T_0 + T_1$.

REFERENCES

[1] N. B. Budanur, D. Borrero-Echeverry, and P. Cvitanović, "Periodic orbit analysis of a system with continuous symmetry-a tutorial," *Chaos: An Interdisciplinary Journal of Nonlinear Science*, vol. 25, no. 7, p. 073 112, 2015.

[2] B. Suri, J. Tithof, R. O. Grigoriev, and M. F. Schatz, "Forecasting fluid flows using the geometry of turbulence," *Physical review letters*, vol. 118, no. 11, p. 114 501, 2017.

[3] D. Barkley, "Simplifying the complexity of pipe flow," *Physical Review E*, vol. 84, no. 1, p. 016 309, 2011.

[4] L. S. Tuckerman, T. Kreilos, H. Schrobsdorff, T. M. Schneider, and J. F. Gibson, "Turbulent-laminar patterns in plane poiseuille flow," *Physics of Fluids*, vol. 26, no. 11, p. 114 103, 2014.

[5] F. Mellibovsky and A. Meseguer, "A mechanism for streamwise localisation of nonlinear waves in shear flows," *Journal of Fluid Mechanics*, vol. 779, 2015.

[6] C. Foias, O. Manley, R. Rosa, and R. Temam, *Navier-Stokes equations and turbulence*. Cambridge University Press, 2001, vol. 83.

[7] T. Mullin, "Experimental studies of transition to turbulence in a pipe," *Annual Review of Fluid Mechanics*, vol. 43, pp. 1–24, 2011.

[8] D. Barkley, B. Song, V. Mukund, G. Lemoult, M. Avila, and B. Hof, "The rise of fully turbulent flow," *Nature*, vol. 526, no. 7574, p. 550, 2015.

[9] Y. Cencel and J. Cimbala, "Fluid mechanics–fundamentals and applications," 2006.

[10] V. Mukund and B. Hof, "The critical point of the transition to turbulence in pipe flow," *Journal of Fluid Mechanics*, vol. 839, pp. 76–94, 2018.

[11] J. Barnett, D. R. Gurevich, and R. O. Grigoriev, "Streamwise localization of traveling wave solutions in channel flow," *Physical Review E*, vol. 95, no. 3, p. 033 124, 2017.

[12] E Weinan and J.-G. Liu, "Finite difference methods for 3d viscous incompressible flows in the vorticity–vector potential formulation on nonstaggered grids," *Journal of Computational Physics*, vol. 138, no. 1, pp. 57–82, 1997.

[13] P Cvitanovic, R Artuso, R Mainieri, G Tanner, and G Vattay, "Chaos: classical and quantum, chaosbook. org," *Niels Bohr Institute, Copenhagen, Denmark*, 2016.

[14] M. Beck and C. E. Wayne, "Using global invariant manifolds to understand metastability in the burgers equation with small viscosity," *SIAM Journal on Applied Dynamical Systems*, vol. 8, no. 3, pp. 1043–1065, 2009.

[15] J. Bec and K. Khanin, "Burgers turbulence," *Physics Reports*, vol. 447, no. 1-2, pp. 1–66, 2007.

[16] M. Cross and H. Greenside, *Pattern formation and dynamics in nonequilibrium systems*. Cambridge University Press, 2009.

[17] A Meseguer and L. N. Trefethen, "Linearized pipe flow to reynolds number 10^7," *Journal of Computational Physics*, vol. 186, no. 1, pp. 178–197, 2003.

[18] R. J. Deissler, "Turbulent bursts, spots and slugs in a generalized ginzburg-landau equation," *Physics letters A*, vol. 120, no. 7, pp. 334–340, 1987.

[19] ——, "External noise and the origin and dynamics of structure in convectively unstable systems," *Journal of statistical physics*, vol. 54, no. 5-6, pp. 1459–1488, 1989.

[20] S. A. Orszag, "Accurate solution of the orr–sommerfeld stability equation," *Journal of Fluid Mechanics*, vol. 50, no. 4, pp. 689–703, 1971.

[21] M. Chantry, A. P. Willis, and R. R. Kerswell, "Genesis of streamwise-localized solutions from globally periodic traveling waves in pipe flow," *Physical review letters*, vol. 112, no. 16, p. 164 501, 2014.

[22] S. Zammert and B. Eckhardt, "Streamwise and doubly-localised periodic orbits in plane poiseuille flow," *Journal of Fluid Mechanics*, vol. 761, pp. 348–359, 2014.

[23] H. Faisst and B. Eckhardt, "Transition from the couette-taylor system to the plane couette system," *Physical Review E*, vol. 61, no. 6, p. 7227, 2000.

[24] M. Kramár, R. Levanger, J. Tithof, B. Suri, M. Xu, M. Paul, M. F. Schatz, and K. Mischaikow, "Analysis of kolmogorov flow and rayleigh–bénard convection using persistent homology," *Physica D: Nonlinear Phenomena*, vol. 334, pp. 82–98, 2016.

[25] B. Suri, J. Tithof, R. Mitchell Jr, R. O. Grigoriev, and M. F. Schatz, "Velocity profile in a two-layer kolmogorov-like flow," *Physics of Fluids*, vol. 26, no. 5, p. 053 601, 2014.

[26] D. Coles, "Transition in circular couette flow," *Journal of Fluid Mechanics*, vol. 21, no. 3, pp. 385–425, 1965.

[27] A. Prigent, "La spirale turbulente," PhD thesis, Université Paris Sud-Paris XI, 2001.

[28] D. Barkley and L. S. Tuckerman, "Computational study of turbulent laminar patterns in couette flow," *Physical review letters*, vol. 94, no. 1, p. 014 502, 2005.

[29] D. Samanta, A. De Lozar, and B. Hof, "Experimental investigation of laminar turbulent intermittency in pipe flow," *Journal of Fluid Mechanics*, vol. 681, pp. 193–204, 2011.

[30] E Knobloch, "Spatially localized structures in dissipative systems: open problems," *Nonlinearity*, vol. 21, no. 4, T45, 2008.

[31] F. Reetz, T. Kreilos, and T. M. Schneider, "Exact invariant solution reveals the origin of self-organized oblique turbulent-laminar stripes," *Nature communications*, vol. 10, no. 1, p. 2277, 2019.

[32] P. Gaspard, "Encyclopedia of nonlinear science, alwyn scott, editor,(routledge, new york, 2005) pp. 264-266.,"

[33] D. Bullara and Y. De Decker, "Pigment cell movement is not required for generation of turing patterns in zebrafish skin," *Nature communications*, vol. 6, p. 6971, 2015.

[34] H. Shoji, K. Yamada, D. Ueyama, and T. Ohta, "Turing patterns in three dimensions," *Physical Review E*, vol. 75, no. 4, p. 046 212, 2007.

[35] A. Prigent, G. Grégoire, H. Chaté, O. Dauchot, and W. van Saarloos, "Large-scale finite-wavelength modulation within turbulent shear flows," *Physical review letters*, vol. 89, no. 1, p. 014 501, 2002.

[36] A. P. Willis, K. Y. Short, and P. Cvitanović, "Symmetry reduction in high dimensions, illustrated in a turbulent pipe," *Physical Review E*, vol. 93, no. 2, p. 022 204, 2016.

[37] N. B. Budanur, K. Y. Short, M. Farazmand, A. P. Willis, and P. Cvitanović, "Relative periodic orbits form the backbone of turbulent pipe flow," *J. Fluid Mech.*, vol. 833, pp. 274–301, 2017.

[38] K. Short, "Periodic solutions and chaos in the barkley pipe model on a finite domain," *Physical Review E*, vol. 100, no. 2, p. 023 116, 2019.

[39] A. P. Willis, "The openpipeflow navier–stokes solver," *SoftwareX*, vol. 6, pp. 124–127, 2017.

[40] B. Hof, C. W. H. van Doorne, J. Westerweel, F. T. M. Nieuwstadt, H. Faisst, B. Eckhardt, H. Wedin, R. R. Kerswell, and F. Waleffe, "Experimental observation of nonlinear traveling waves in turbulent pipe flow," *Science*, vol. 305, pp. 1594–1598, 2004.

[41] D. J. C. Dennis and F. M. Sogaro, "Distinct organizational states of fully developed turbulent pipe flow," *Phys. Rev. Lett.*, vol. 113, p. 234 501, 2014.

[42] R. R. Kerswell and O. Tutty, "Recurrence of travelling waves in transitional pipe flow," *J. Fluid Mech.*, vol. 584, pp. 69–102, 2007.

[43] A. de Lozar, F. Mellibovsky, M. Avila, and B. Hof, "Edge state in pipe flow experiments," *Phys. Rev. Lett.*, vol. 108, p. 214 502, 2012.

[44] Y. Duguet, A. P. Willis, and R. R. Kerswell, "Transition in pipe flow: the saddle structure on the boundary of turbulence," *J. Fluid Mech.*, vol. 613, pp. 255–274, 2008.

[45] M. Avila, F. Mellibovsky, N. Roland, and B. Hof, "Streamwise-localized solutions at the onset of turbulence in pipe flow," *Phys. Rev. Lett.*, vol. 110, p. 224 502, 2013.

[46] M. Chantry, A. P. Willis, and R. R. Kerswell, "Genesis of streamwise-localized solutions from globally periodic traveling waves in pipe flow," *Phys. Rev. Lett.*, vol. 112, p. 164 501, 2014.

[47] J. F. Gibson, J. Halcrow, and P. Cvitanović, "Visualizing the geometry of state space in plane Couette flow," *J. Fluid Mech.*, vol. 611, pp. 107–130, 2008.

[48] E. Hopf, "A mathematical example displaying features of turbulence," *Commun. Pure Appl. Math.*, vol. 1, pp. 303–322, 1948.

[49] N. B. Budanur, P. Cvitanović, R. L. Davidchack, and E. Siminos, "Reduction of the SO(2) symmetry for spatially extended dynamical systems," *Phys. Rev. Lett.*, vol. 114, p. 084 102, 2015, 1405.1096.

[50] E. Cartan, *La méthode du repère mobile, la théorie des groupes continus, et les espaces généralisés*, ser. Exposés de Géométrie. Paris: Hermann, 1935, vol. 5.

[51] C. W. Rowley and J. E. Marsden, "Reconstruction equations and the Karhunen-Loéve expansion for systems with symmetry," *Physica D*, vol. 142, pp. 1–19, 2000.

[52] A. P. Willis, P. Cvitanović, and M. Avila, "Revealing the state space of turbulent pipe flow by symmetry reduction," *J. Fluid Mech.*, vol. 721, pp. 514–540, 2013.

[53] P. Frederickson, J. L. Kaplan, E. D. Yorke, and J. A. Yorke, "The Liapunov dimension of strange attractors," *J. Diff. Eqn.*, vol. 49, pp. 185–207, 1983.

[54] J. Jiménez and P. Moin, "The minimal flow unit in near-wall turbulence," *J. Fluid Mech.*, vol. 225, pp. 213–240, 1991.

[55] J. M. Hamilton, J. Kim, and F. Waleffe, "Regeneration mechanisms of near-wall turbulence structures," *J. Fluid Mech.*, vol. 287, pp. 317–348, 1995.

[56] G. Hagen, "Ueber die bewegung des wassers in engen cylindrischen röhren," *Annalen der Physik*, vol. 122, no. 3, pp. 423–442, 1839.

[57] J. L. Poiseuille, *Recherches expérimentales sur le mouvement des liquides dans les tubes de très-petits diamètres*. Imprimerie Royale, 1844.

[58] M. Avila, A. P. Willis, and B. Hof, "On the transient nature of localized pipe flow turbulence," *Journal of Fluid Mechanics*, vol. 646, pp. 127–136, 2010.

[59] B. Hof, J. Westerweel, T. M. Schneider, and B. Eckhardt, "Finite lifetime of turbulence in shear flows," *Nature*, vol. 443, no. 7107, p. 59, 2006.

[60] K. Avila, D. Moxey, A. de Lozar, M. Avila, D. Barkley, and B. Hof, "The onset of turbulence in pipe flow," *Science*, vol. 333, no. 6039, pp. 192–196, 2011.

[61] H. Faisst and B. Eckhardt, "Traveling waves in pipe flow," *Physical Review Letters*, vol. 91, no. 22, p. 224 502, 2003.

[62] H. Wedin and R. R. Kerswell, "Exact coherent structures in pipe flow: travelling wave solutions," *Journal of Fluid Mechanics*, vol. 508, pp. 333–371, 2004.

[63] C. C. Pringle and R. R. Kerswell, "Asymmetric, helical, and mirror-symmetric traveling waves in pipe flow," *Physical review letters*, vol. 99, no. 7, p. 074 502, 2007.

[64] J. F. Gibson, "Channelflow: a spectral navier–stokes simulator in c++," *New Hampshire*, 2012.

[65] F. Mellibovsky and B. Eckhardt, "From travelling waves to mild chaos: a supercritical bifurcation cascade in pipe flow," *Journal of fluid mechanics*, vol. 709, pp. 149–190, 2012.

[66] D. Auerbach, P. Cvitanović, J.-P. Eckmann, G. Gunaratne, and I. Procaccia, "Exploring chaotic motion through periodic orbits," *Physical Review Letters*, vol. 58, no. 23, p. 2387, 1987.

[67] N. B. Budanur and B. Hof, "Heteroclinic path to spatially localized chaos in pipe flow," *Journal of Fluid Mechanics*, vol. 827, 2017.

[68] P. Cvitanovic, R. Artuso, R. Mainieri, G. Tanner, and G. Vattay, "Chaos: classical and quantum,"

[69] T. Kreilos, S. Zammert, and B. Eckhardt, "Comoving frames and symmetry-related motions in parallel shear flows," *Journal of Fluid Mechanics*, vol. 751, pp. 685–697, 2014.

[70] C. W. Rowley, I. G. Kevrekidis, J. E. Marsden, and K. Lust, "Reduction and reconstruction for self-similar dynamical systems," *Nonlinearity*, vol. 16, no. 4, p. 1257, 2003.

[71] P. Cvitanović, D. Borrero-Echeverry, K. M. Carroll, B. Robbins, and E. Siminos, "Cartography of high-dimensional flows: a visual guide to sections and slices," *Chaos: An Interdisciplinary Journal of Nonlinear Science*, vol. 22, no. 4, p. 047 506, 2012.

[72] D. Viswanath, "Recurrent motions within plane couette turbulence," *Journal of Fluid Mechanics*, vol. 580, pp. 339–358, 2007.

[73] G. J. Chandler and R. R. Kerswell, "Invariant recurrent solutions embedded in a turbulent two-dimensional kolmogorov flow," *Journal of Fluid Mechanics*, vol. 722, pp. 554–595, 2013.

[74] C. C. Pringle, Y. Duguet, and R. R. Kerswell, "Highly symmetric travelling waves in pipe flow," *Philosophical Transactions of the Royal Society A: Mathematical, Physical and Engineering Sciences*, vol. 367, no. 1888, pp. 457–472, 2008.

[75] K. Short and A. P. Willis, "Bifurcation structure of relative periodic orbits in pipe flow. in preparation.," 2016.

[76] P. Cvitanović, G. H. Gunaratne, and I. Procaccia, "Topological and metric properties of hénon-type strange attractors," *Physical Review A*, vol. 38, no. 3, p. 1503, 1988.

[77] A. de Carvalho and T. Hall, "How to prune a horseshoe," *Nonlinearity*, vol. 15, no. 3, R19, 2002.

[78] M. Benedicks and L. Carleson, "The dynamics of the hénon map," *Annals of Mathematics*, vol. 133, no. 1, pp. 73–169, 1991.

[79] J. Halcrow, J. F. Gibson, P. Cvitanović, and D. Viswanath, "Heteroclinic connections in plane couette flow," *Journal of Fluid Mechanics*, vol. 621, pp. 365–376, 2009.

[80] G. Mathew, I. Mezić, S. Grivopoulos, U. Vaidya, and L. Petzold, "Optimal control of mixing in stokes fluid flows," *Journal of Fluid Mechanics*, vol. 580, pp. 261–281, 2007.

[81] Z. Lin, J.-L. Thiffeault, and C. R. Doering, "Optimal stirring strategies for passive scalar mixing," *Journal of Fluid Mechanics*, vol. 675, pp. 465–476, 2011.

[82] M. Farazmand, "An adjoint-based approach for finding invariant solutions of navier–stokes equations," *Journal of Fluid Mechanics*, vol. 795, pp. 278–312, 2016.

[83] P Cvitanovic, "Life in extreme dimensions," *Chaos: Classical and Quantum (ed. P. Cvitanovic, R. Artuso, R. Mainieri, G. Tanner & G. Vattay). Niels Bohr Institute*, 2017.

[84] P. Lax, *Functional analysis*, ser. Pure and applied mathematics. Wiley, 2002, ISBN: 9780471556046.

[85] G. Berkooz, P. Holmes, and J. L. Lumley, "The proper orthogonal decomposition in the analysis of turbulent flows," *Annual review of fluid mechanics*, vol. 25, no. 1, pp. 539–575, 1993.

[86] N. B. Budanur and P. Cvitanović, "Unstable manifolds of relative periodic orbits in the symmetry-reduced state space of the kuramoto–sivashinsky system," *Journal of Statistical Physics*, vol. 167, no. 3-4, pp. 636–655, 2017.

[87] N. B. Budanur, "Exact coherent structures in spatiotemporal chaos: from qualitative description to quantitative predictions," PhD thesis, Georgia Institute of Technology, 2015.

[88] B. Hof, A. de Lozar, D. J. Kuik, and J. Westerweel, "Repeller or attractor? selecting the dynamical model for the onset of turbulence in pipe flow," *Physical review letters*, vol. 101, no. 21, p. 214 501, 2008.

[89] B. Eckhardt, "Turbulence transition in shear flows: chaos in high-dimensional spaces," *Procedia IUTAM*, vol. 5, pp. 165–168, 2012.

[90] T. Kreilos, "Turbulence transition in shear flows and dynamical systems theory," Philipps-Universität Marburg, Tech. Rep., 2014.

[91] Y.-C. Lai and T. Tél, *Transient chaos: complex dynamics on finite time scales*. Springer Science & Business Media, 2011, vol. 173.

[92] H. Faisst and B. Eckhardt, "Sensitive dependence on initial conditions in transition to turbulence in pipe flow," *Journal of Fluid Mechanics*, vol. 504, pp. 343–352, 2004.

[93] V. A. Romanov, "Stability of plane-parallel couette flow," *Functional analysis and its applications*, vol. 7, no. 2, pp. 137–146, 1973.

[94] S. Grossmann, "The onset of shear flow turbulence," *Reviews of modern physics*, vol. 72, no. 2, p. 603, 2000.

[95] P. Manneville, "Turbulent patterns in wall-bounded flows: a turing instability?" *EPL (Europhysics Letters)*, vol. 98, no. 6, p. 64 001, 2012.

[96] D. Barkley, "Modeling the transition to turbulence in shear flows," in *Journal of Physics: Conference Series*, IOP Publishing, vol. 318, 2011, p. 032 001.

[97] V. Klika and E. A. Gaffney, "History dependence and the continuum approximation breakdown: the impact of domain growth on turing?s instability," *Proceedings of the Royal Society A: Mathematical, Physical and Engineering Sciences*, vol. 473, no. 2199, p. 20 160 744, 2017.

[98] S. Houghton and E Knobloch, "Homoclinic snaking in bounded domains," *Physical Review E*, vol. 80, no. 2, p. 026 210, 2009.

[99] B Hof, A Juel, and T Mullin, "Scaling of the turbulence transition threshold in a pipe," *Physical review letters*, vol. 91, no. 24, p. 244 502, 2003.

[100] S. H. Strogatz, *Nonlinear dynamics and chaos: with applications to physics, biology, chemistry, and engineering*. CRC Press, 2018.

[101] V. K. Vanag and I. R. Epstein, "Out-of-phase oscillatory turing patterns in a bistable reaction-diffusion system," *Physical Review E*, vol. 71, no. 6, p. 066 212, 2005.

[102] Y. Duguet, P. Schlatter, and D. S. Henningson, "Formation of turbulent patterns near the onset of transition in plane couette flow," *Journal of Fluid Mechanics*, vol. 650, pp. 119–129, 2010.

[103] N. Nikitin and V. Pimanov, "Numerical study of localized turbulent structures in a pipe," *Fluid Dynamics*, vol. 50, no. 5, pp. 655–664, 2015.

[104] V. K. Vanag and I. R. Epstein, "Localized patterns in reaction-diffusion systems," *Chaos: An Interdisciplinary Journal of Nonlinear Science*, vol. 17, no. 3, p. 037 110, 2007.

[105] S. Sen, P. Ghosh, S. S. Riaz, and D. S. Ray, "Time-delay-induced instabilities in reaction-diffusion systems," *Physical Review E*, vol. 80, no. 4, p. 046 212, 2009.

[106] T. Zhang and H. Zang, "Delay-induced turing instability in reaction-diffusion equations," *Physical Review E*, vol. 90, no. 5, p. 052 908, 2014.

[107] F. Waleffe, "On a self-sustaining process in shear flows," *Physics of Fluids*, vol. 9, no. 4, pp. 883–900, 1997.

[108] M. Chantry, L. S. Tuckerman, and D. Barkley, "Universal continuous transition to turbulence in a planar shear flow," *Journal of Fluid Mechanics*, vol. 824, 2017.

[109] G. Lemoult, L. Shi, K. Avila, S. V. Jalikop, M. Avila, and B. Hof, "Directed percolation phase transition to sustained turbulence in couette flow," *Nature Physics*, vol. 12, no. 3, p. 254, 2016.

[110] S. Havlin and D. Ben-Avraham, "Diffusion in disordered media," *Advances in Physics*, vol. 36, no. 6, pp. 695–798, 1987.

[111] N. Goldenfeld, N. Guttenberg, and G. Gioia, "Extreme fluctuations and the finite lifetime of the turbulent state," *Physical Review E*, vol. 81, no. 3, p. 035 304, 2010.

VITA

KYS grew up in rural Oklahoma, the daughter of a truck driver. She started university way too young (age 15), intending to study physics but got distracted and built theatre sets instead. She picked up some French along the way; did the singer-songwriter play-guitar-in-coffee-shops-for-tips-and-veggie-sandwiches thing for a while; was a disk jockey at a couple radio stations in New Mexico; wrote radio and billboard copy for an ad agency in Texas; very nearly went to law school in Arizona; and was gainfully employed as an accountant in offices where people actually wear suits and pantyhose and high heels.

It took a while, but she eventually got that PhD in physics.

She wishes she could have received a nonzero amount of encouragement, support, or mentorship from her advisor(s) during her PhD. It would have made all the difference.